Ultracold Fermi Gases in a Bichromatic Optical Superlattice

by

Chingyun Cheng

Department of Physics
Duke University

Date: _____

Approved:

_____
John E. Thomas, Supervisor

_____
Steffen A. Bass, Chair

_____
Calvin R. Howell

_____
Glenn S. Edwards

_____
Jian-Guo Liu

Dissertation submitted in partial fulfillment of the requirements for the degree of
Doctor of Philosophy in the Department of Physics
in the Graduate School of Duke University
2016

Abstract

Ultracold Fermi Gases in a Bichromatic Optical Superlattice

by

Chingyun Cheng

Department of Physics
Duke University

Date: _____

Approved:

_____
John E. Thomas, Supervisor

_____
Steffen A. Bass, Chair

_____
Calvin R. Howell

_____
Glenn S. Edwards

_____
Jian-Guo Liu

An abstract of a dissertation submitted in partial fulfillment of the requirements for the degree of Doctor of Philosophy in the Department of Physics in the Graduate School of Duke University
2016

Abstract

I describe the theory and construction of a new bichromatic optical superlattice to study the pairing and thermodynamics of mixtures of spin $\frac{1}{2}$-up and spin $\frac{1}{2}$-down atoms in periodic double well potentials. Our bichromatic lattice contains $\lambda_1 = 1064$ nm and $\lambda_2 = 532$ nm standing wave lattices. With tunable depth and relative phase between the two lattices, periodic double well potentials of arbitrary local symmetry can be constructed.

I present the first systematic experimental study of a two-component ultracold ^{6}Li atomic Fermi gas in a single color 1064 nm lattice, which is continuously tuned from 2D to quasi-2D. A system is 2D if it is free to move in two dimensions while tightly confined in the third direction, such that only the ground state is occupied. Conversely, it is quasi-2D if higher states in the tightly confined direction are also occupied. I describe both radio frequency spectra and radial cloud profiles measured under identical conditions for each regime. Our results confirm predictions that the mean-field theory is not valid throughout the 2D to quasi-2D dimensional crossover. We also clarify that there is no transition between 2D and quasi-2D systems.

I also present the first study of pairing in a periodic double well potential. A Green's function method is developed to compute the pairing energies in the lattice. Although further understanding of the results are needed, I provide some preliminary rf spectra measurements supporting the theoretical approach and implying the existence of two types of pairing.

Contents

List of Figures

Acknowledgements

I am truly grateful for my advisor Dr. John Thomas. John is one of the most encouraging, inspiring physicist that I know and love. We started the lattice business together because he can tell that I have a real passion for it. We've come a long way and now he does not hate Hubbard model anymore! I hope this is a good change for him.

I want to thank my colleagues, especially our postdoc Ilya and junior student Kan for working closely with me. We suffered, argued, and shared lots of joyful moments. I will certainly miss the discussions and coffee breaks I had with Ilya. I will also remember those late night working in the lab with Kan while both of us were starving. Also huge thanks to Kan's wife for not divorcing him! I sincerely wish Kan the best in the future.

A lot has happened during the past few years of my life, and I am blessed to have the support and love from my dear family and friends.

1

Introduction

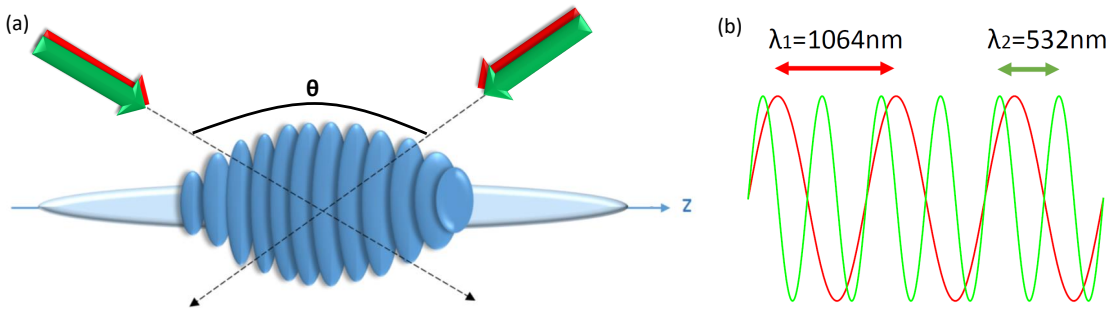

FIGURE 1.1: Bichromatic superlattice constructed by two color co-propagating beams of $\lambda_1 = 1064$ nm and $\lambda_2 = 532$ nm. (a) Two beams co-propagate and intersect at $\theta = 91^\circ$ and form a bichromatic lattice. The lattice is superposed on a CO_2 laser dipole trap along its axial direction z. (b) Illustration of tunable relative phase between the two color beams.

My dissertation presents the theory and construction of a new bichromatic optical lattice to study the pairing and thermodynamics of strongly interacting ultracold Fermi gases in periodic double well potentials. A bichromatic superlattice is constructed by co-propagating two color beams of $\lambda_1 = 1064$ nm and $\lambda_2 = 532$ nm, intersecting at $\theta = 91^\circ$ and superposed along the axial direction of a CO_2 laser dipole trap, as shown in Fig. 1.1. We load atoms into this composite trap to gen-

erate an ensemble of bilayer clouds. By changing the relative intensity and phase between the two color lattices, we construct periodic double well potentials of flexible local symmetry, as illustrated in Fig. 1.2. Such a composite trap system enables the study of dimensional crossover, control of dispersion and extended fermionic pairing.

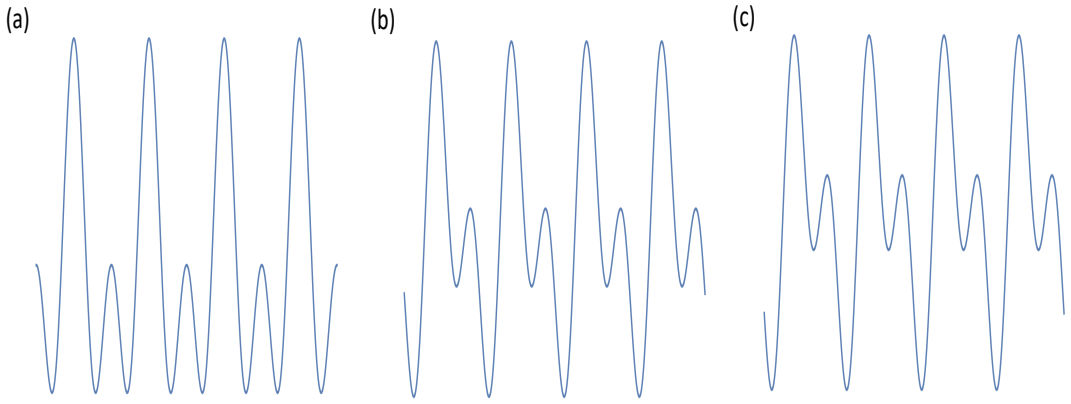

FIGURE 1.2: An illustration of modifying the double well geometry by changing the relative phase ϕ between the two color lattices. Plotted for $V(x) = -V_1 \cos^2(kx) + V_2 \cos^2(2kx + \phi)$ with $V_1 = V_2 = 1$ and relative phase (a) $\phi = 0$, (b) $\phi = 3\pi/16$, and (c) $\phi = \pi/4$. As a result, the tunneling and pairing are expected to be altered significantly.

I first study the 2D to quasi-2D crossover using just a single color infrared optical lattice, for testing the validity of the 2D Bardeen-Cooper-Schrieffer (BCS) mean field theory. A system is 2D if it is free to move in two dimensions x and y , while tightly confined in the third direction z. Assuming a harmonic confinement, a gas is 2D if only the z harmonic oscillator ground state, whose energy is $\frac{1}{2}h\nu_z$, is occupied. Conversely, the system is quasi-2D if higher states in the tightly confined direction are also occupied.

Recent experiments have made a number of intriguing and somewhat puzzling observations regarding the applicability of mean field theory to describe 2D many-body systems. An undamped, monopole breathing mode is found to oscillate at

twice the trap frequency for a broad range of temperatures and couplings across the 2D crossover [1]. This apparent scale-invariant behavior, in a theory with an explicit scale of pairing energy E_b, is very surprising [2], but emerges naturally from zero temperature mean field theory. Radio frequency spectra obtained in the 2D regime [3, 4], reveal that the absorption threshold is close to E_b, a 2D-BCS mean field prediction [5] that one would not have expected to be quantitatively valid in 2D. Although one might expect similar 2D-behavior for a quasi-2D gas, the measured spectra are in strong disagreement with BCS mean field theory [6], as are the measured thermodynamic properties [7, 8, 9, 10, 11, 12], which require a beyond mean field treatment. This raises an important open question: Can mean field theory describe the thermodynamics of a 2D gas when the spectrum is correctly predicted? We present in this thesis work the first systematic experimental study.

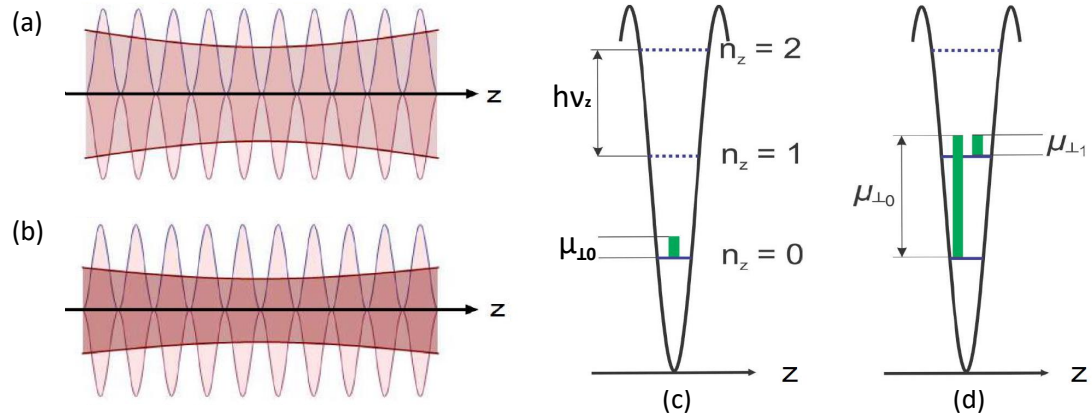

FIGURE 1.3: Defining dimensionality of the gas. A deep optical lattice is generated along the z-direction by interfering two $\lambda = 1064$ nm beams. (a) represents a weaker radial confinement from the CO_2 laser trap, thus a lower Fermi energy, than in (b). Part (c) and (d) illustrate the radial chemical potential $\mu_\perp$ of each axial state. When the chemical potential is small compared to $h\nu_z$, the gas is 2D, as in (a) and (c). The gas is quasi-2D when Fermi energy is comparable to $h\nu_z$, as in (b) and (d), where higher axial states are occupied.

For our system of gas loaded in a one dimensional standing wave lattice, when the radial Fermi energy E_F is small compared to $h\nu_z$, the energy difference between

two states in the tight confinement direction, the gas is 2D as shown in Fig. 1.3(a) and (c). In contrast the gas is quasi-2D when E_F and $h\nu_z$ are comparable such that higher axial states are occupied, as shown in Fig. 1.3(b) and (d). The dimensionality of the gas within each single layer is tuned from 2D to quasi-2D by continuously increasing the transverse Fermi energy, by increasing the radial confinement of the CO_2 laser potential.

The measurements employ two primary techniques. Radio-frequency (rf) spectroscopy is used to measure the pair-binding energy and phase contrast imaging is used for extracting the cloud radii, to study the thermodynamics. I present both rf spectra and radial cloud profile measurements taken under identical conditions for each regime, to test the validity of the 2D BCS mean-field theory systematically for the first time. For the quasi-2D gas, we find that the spectra disagree with 2D-BCS theory. For the 2D gas, we find that the spectra can be fit by 2D-BCS mean field theory, consistent with previous work[3, 13]. In contrast to the spectra, we find that the radii for 2D clouds are much smaller than those predicted by 2D-BCS mean field theory, which yields ideal gas density profiles[14]. Our results show that there is no transition between 2D and quasi-2D systems and that beyond mean field descriptions are required in both regimes.

Next I use rf spectroscopy to study extended fermionic pairing interactions in periodic double well potentials as shown in Fig. 1.4, where an ensemble of bilayer Fermi gases are formed. The shape of each double well is changed by varying the depth and relative phase between the two color lattices, as illustrated in Fig. 1.1(b) and Fig. 1.2. The change in double well local symmetry modifies the interlayer coupling and tunneling, which one would expect to alter the binding of extended pairs significantly. We develop a Green's function approach for computing the extended pair energies in a double well bilayer gas, and present the first preliminary results for the rf spectra. We find reasonable agreement between the theory and measurement,

indicating that two types of dimer pairing is possible.

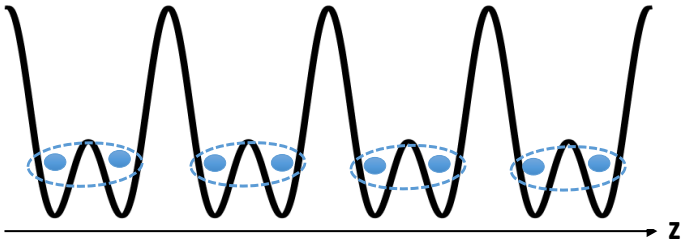

FIGURE 1.4: Illustration of the extended pairing in a double well bilayer gas.

One can control the dispersion of strongly correlated superfluids in the bichromatic lattice. By choosing certain depth and relative phase, a Dirac point is generated between the second and third bands, and the gas can be made linearly dispersive [15]. Our future goal is to use the CO_2 laser trap to tune the Fermi energy to the band crossing region of the one dimensional Dirac point, creating an analog of a trapped, relativistic Fermi gas.

1.1 Fermi gas with tunable interactions: Feshbach resonance

We trap and cool a dilute gas of fermionic ^{6}Li atoms to quantum degeneracy, where the interparticle spacing is small compared to the de Broglie wavelength $\lambda_{dB} = h/(\sqrt{2\pi m k_B T})$. In this regime, the wavepackets of adjacent particles starts to overlap such that a classical description is no longer valid. The gas now has to be described by a many-body wavefunction governed by Fermi statistics, which requires the wavefunction to be antisymmetrized under exchange of particles. In the dilute limit $nr_0^3 << 1$ where r_0 is the range of the interatomic potential, the average interparticle spacing is much greater than the range of the interatomic potential. The interaction between particles can be taken as short range. In this limit, three-body collisions are rare and only two-body s-wave scattering is considered to be dominant.

From a heuristic standpoint, consider a collision in which two atoms have a rela-

tive linear momentum p. The maximum relative orbital angular momentum that is relevant to the scattering process is approximately given by $L \simeq r_0 p \simeq r_0 h/\lambda_{dB} << 1$. Since the angular momentum is quantized $L = l\hbar$, and $L << 1$ only $l = 0$, i.e. s-wave scattering, is allowed. One can model the short range interaction as a pseudopotential [16]

$$V(\mathbf{r})\Psi(\mathbf{r}) = \frac{4\pi\hbar^2 a}{m}\delta(\mathbf{r})\frac{\partial}{\partial r}\left[r\Psi(\mathbf{r})\right], \tag{1.1}$$

where $\mathbf{r} = \mathbf{r_1} - \mathbf{r_2}$ specifies the relative position of the two atoms and a is the scattering length. In our system, the scattering strength can be tuned from zero to very strongly attractive $a < 0$ or repulsive $a > 0$ where $a \gg \lambda_{dB}$ is strongly interacting, using an external bias magnetic field near a collisional Feshbach resonance.

Since the Pauli exclusion principle prevents identical fermions interacting with each other via s-wave scattering, in order for interaction to exist, we use a two-component Fermi gas with atoms in the lowest two hyperfine states $|1\rangle$ and $|2\rangle$ of ^{6}Li. All alkali atoms have only one valence electron ($s = 1/2$). Therefore, states $|1\rangle$ and $|2\rangle$ interact via either spin singlet molecular potential or spin triplet molecular potential for s-wave scattering. For a spin singlet state whose spin wavefunction is antisymmetric, to antisymmetrize the overall wavefunction, the spatial wavefunction is symmetric. The symmetric spatial wavefunction of the spin-singlet state reduces the repulsive interaction between the nuclei, resulting in a deeper molecular potential than the triplet.

In Fig. 1.5, atomic potentials for both singlet and triplet states are shown near a Feshbach resonance. Bound molecular states exist in the deep singlet potential, also referred to as the energetically closed channel. The two atom state in the shallow triplet potential, called the open channel, has energy higher than the energy of the singlet bound state. An external magnetic field is applied to Zeeman shift the energy level of the triplet state towards that of the singlet bound state.

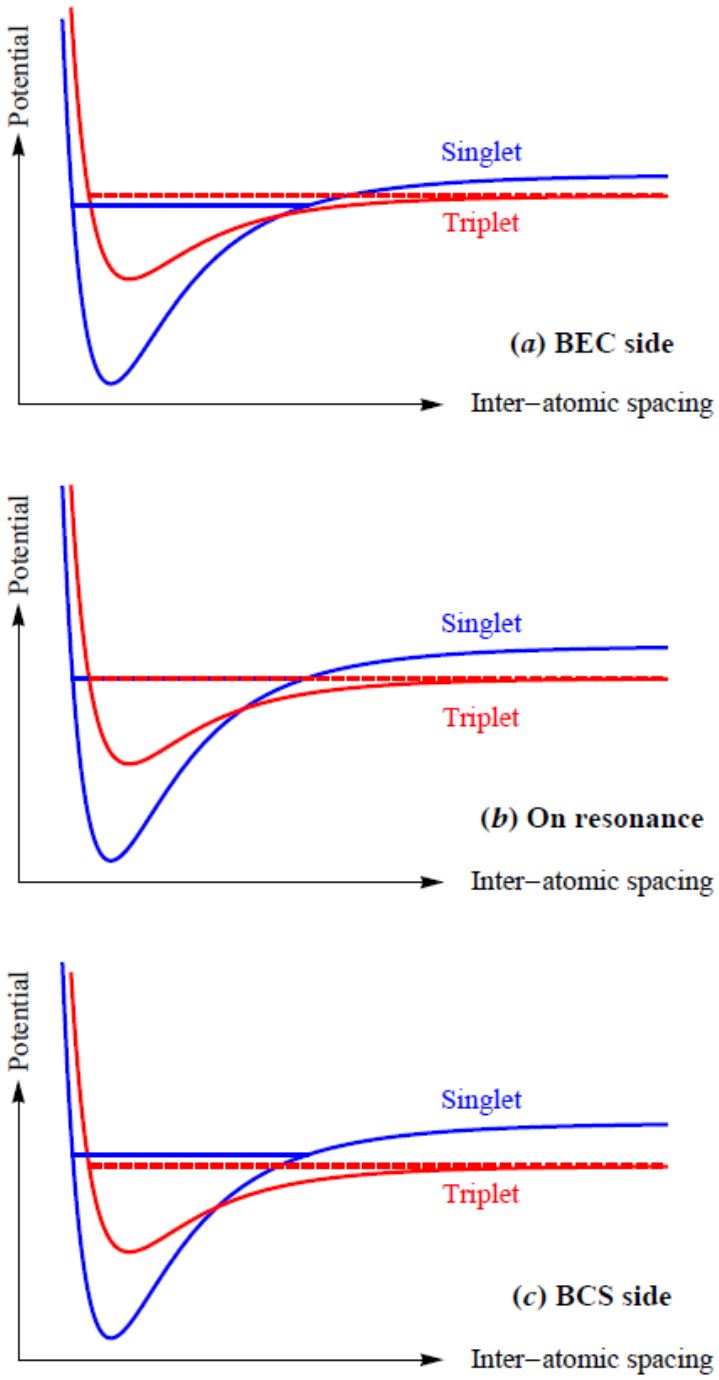

FIGURE 1.5: Relative positions of atomic potential for the highest lying singlet bound molecular vibrational state (solid horizontal blue line) and triplet two atom states(red dashed line) around a Feshbach resonance. The triplet state can be tuned by a magnetic field. (a) $B < B_0$ corresponds to the BEC side of Feshbach resonance where molecular dimers are stable; (b) $B = B_0$ corresponds to resonance; (c) $B > B_0$ corresponds to BCS side, where molecular dimers are not stable, and decay into the triplet continuum.

When the open and closed channel are tuned to be degenerate at $B = B_0$, as shown in Fig. 1.5(b), the hyperfine coupling between the two channels give rise to a Feshbach resonance, where the scattering length diverges and leads to strong interactions. When the magnetic field is at $B < B_0$, the energy of the triplet two atom state lies above the singlet bound state, as shown in Fig. 1.5(a). The scattering length is positive and interactions are repulsive. The triplet two atoms form stable bosonic dimers due to three-body recombination and form a molecular BEC at low temperatures. This regime is called the BEC side of the resonance. Conversely, when the magnetic field is tuned to $B > B_0$ as shown in Fig. 1.5(c), the scattering length is negative and the interactions are attractive. The singlet molecular state is unstable and decays into the triplet continuum due to the hyperfine coupling. In a many-body system above B_0 two atom states form Cooper pairs due to the weak attractive interaction in the presence of other fermions, and form a Fermi superfluid at low temperatures. This corresponds to the right side of the resonance in Fig. 1.6, or the BCS side of the resonance.

The Feshbach resonance is parametrized as a function of the magnetic field B as [17],

$$a_s(B) = a_b \left(1 + \frac{\Delta}{B - B_0}\right)(1 + \alpha(B - B_0)), \tag{1.2}$$

where the background scattering length $a_b = -1450\ a_0$, a_0 is the Bohr radius. The resonance occurs at $B_0 = 832.2$ G [18, 19] and has a width of $\Delta = 300$ G, and $\alpha = 0.0004\ \mathrm{G}^{-1}$ is the first-order correction. This is sometimes referred to as the broad Feshbach resonance[1]. The broad Feshbach resonance provides a controllable way to explore the strongly interacting nature of the system. Figure 1.6 illustrates the ^{6}Li $|1\rangle$-$|2\rangle$ s-wave scattering length around the broad Feshbach resonance.

[1] There is a narrow Feshbach resonance located at 543 G with width less than 1 G.

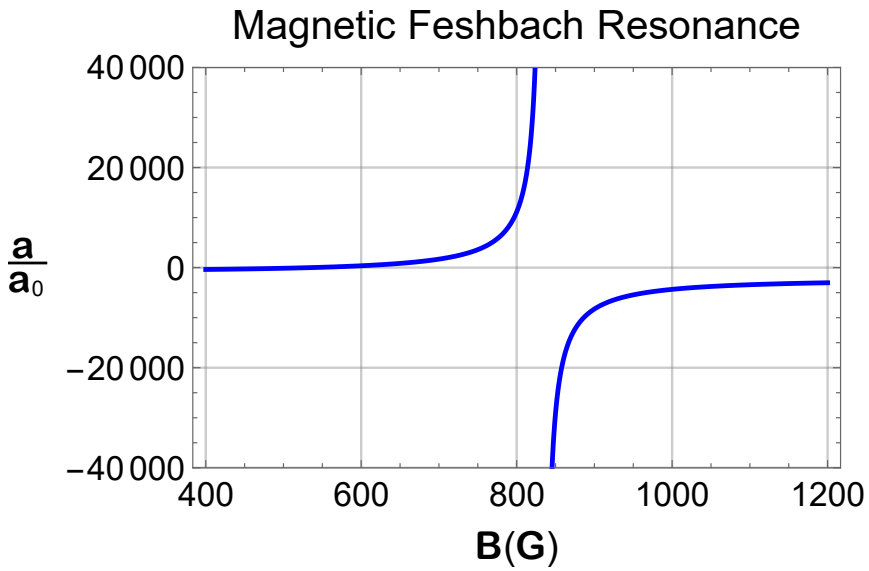

FIGURE 1.6: S-wave scattering length in units of Bohr radius versus magnetic field for ^{6}Li $|1\rangle$-$|2\rangle$ scattering channels around broad Feshbach resonance at $B_0 = 832.2$ G. $B < B_0$ is the BEC side, and $B > B_0$ is the BCS side.

1.2 Validity of 2D BCS Mean-Field Theory

A quantum system is 2D if the chemical potential and the thermal energy are smaller than the energy difference between two consecutive states in the strongly confined direction. For a deep one dimensional optical lattice in the z-direction, the energy difference $h\nu_z$ can be obtained using a harmonic approximation, as shown in Fig. 1.3, where $\omega_z = 2\pi\nu_z$ is the harmonic oscillator frequency. Under this condition, the motion of particles is restricted to the quantum mechanical ground state with a length scale $l_0 = \sqrt{\frac{\hbar}{mw_z}}$, where m is the mass of the atom. This new length scale l_0, which does not exist for a 3D gas, now emerges and is competing with another length scale, the three-dimensional s-wave scattering length a.

In 2D systems the dimer binding energy E_b sets the natural length scale for two-body scattering interactions [20], but a many-body treatment is required when the Fermi energy E_F is large compared to E_b, since the interatomic spacing is then smaller than the size of the dimer [5]. 2D-BCS mean field theory (MFT) [5] provides

an elegant treatment of this problem, but MFT is expected to fail in 2D systems, as noted by Randeria and Taylor [21] and shown in many recent predictions [22, 23, 24, 25, 26, 27, 28]. For quasi-2D systems, the effect of the third dimension on the equation of state and pairing energies is not yet understood [29, 30].

Prior to this thesis work there has been no experimental study of the thermodynamic properties in the 2D regime. I present in Ch 4 the first systematic experimental study of a two-component ultracold ^{6}Li atomic Fermi gas in a single color 1064 nm lattice, continuously tuned from 2D to quasi-2D. Both the rf spectra and cloud radii are measured under the same condition, to demonstrate the effect of the third dimension systematically for the first time.

1.3 Pairing in a Bilayer Fermi Gas

In addition to two-dimensional systems with single layers, bilayer or multilayer systems attracted enormous attention in condensed matter physics. Extra degrees of freedom coming from coupling between layers, i.e. the long-range Coulomb interaction, are expected to lead to intriguing physics such as an interlayer exciton condensation in bilayer semiconductors [31, 32, 33, 34, 35], fractional quantum Hall effect in bilayer quantum well structures [36, 37, 38, 39, 40, 41], and zero-field magnetic phases found in bilayer graphene [42, 43, 44].

In ultracold atoms, an analogous multilayer geometry can be created by confining atoms with a deep bichromatic optical lattice in one direction. Since the long-range Coulomb interaction is absent in neutral atoms, layers separated by distances larger than the range of the collision potential are simply decoupled without interlayer tunneling. With our bichromatic superlattice setup, we are able to construct an ensemble of bilayer Fermi gases. As shown in Fig. 1.3, by controlling the relative phase and amplitude of the two color lattices, tunneling within each bilayer can be tuned, and we are able to study the confinement-induced pairing of these "exciton-

like" molecules which span over adjacent layers, as illustrated in Fig 1.4.

1.4 Dissertation organization

I describe in Ch 2 the optical lattice theory for a bichromatic lattice. Experimental methods including lattice alignment and loading, lattice depth and relative phase calibration, band population measurement, and modulation induced interband transition are described in Ch 3. I address in Ch 4 how the dimensionality of the gas is tuned smoothly from 2D to quasi-2D. Then I discuss the details of using radio-frequency spectroscopy as a measure of the pair binding energy. I present the measured rf spectra and the cloud radii for both regimes. In chapter Ch 5, I describe a Green's function scheme for calculating the pair energies in an bichromatic lattice. I present preliminary rf spectra measurements for the double well superlattice, which supports the existence of two types of dimer pairing, suggesting that two types of superfluid pairing is possible.

2

Bichromatic Lattice Theory

Ultracold quantum gases are versatile and robust systems for probing fundamental condensed-matter physics problems [45, 46, 47, 48, 49, 50, 51, 52], realizing quantum computing[53] and understanding atomic and molecular physics [54]. The readers are encouraged to refer to the review papers by Bloch et al [55, 56]. Storing fermions in an optical lattice allows one to realize the Fermi Hubbard model with tunable interactions with no impurities, which serves as a paradigm for strongly correlated systems in condensed matter physics. The control and tunability of the interactions in ultracold gases provides an ideal approach for studying basic problems in many-body physics, which has not been accessible in condensed matter or nuclear physics.

A laser beam provides an oscillating electric field, which induces an oscillating dipole moment in the atom, and interacts with this dipole moment to create a trapping potential. The laser light is usually detuned far from the atomic resonance frequency, in order to suppress spontaneous emission from resonant excitations to avoid heating. An optical lattice is a spatially periodic potential formed by simply overlapping two counter-propagating laser beams. The interference between the two laser beams of wavelength λ forms an optical standing wave with period $\lambda/2$. In

general one can interfere more beams in more directions to form a 1D, 2D or 3D periodic potentials, as shown in Fig 2.1.

The 1D lattice is effectively an array of 2D disk-like trapping potentials. Two orthogonal optical standing waves create an array of 1D tubes, while three orthogonal optical standing waves correspond to a 3D simple cubic crystal. The advantage of using optical fields to generate periodic trapping potentials is that one has complete control over geometry and depth of the potential, even in the time domain, allowing the study of dynamics such as relaxation after a sudden quench, or transport properties, or creation of artificial gauge fields, etc.

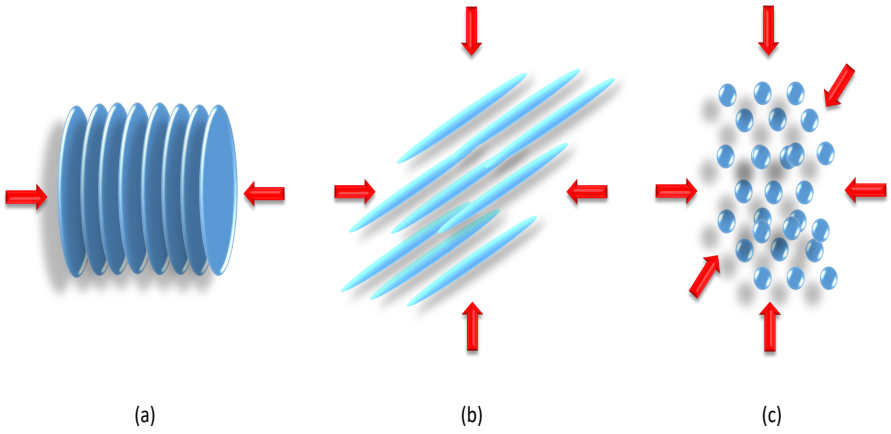

FIGURE 2.1: (a)A 1D optical lattice formed by a retro reflected beams. (b)A 2D optical lattice which tightly confines the atomic motion in two directions. (c)A 3D optical lattice formed by three orthogonal standing wave lattice beams.

Our bichromatic lattice is formed by intersecting two co-propagating beams, with wavelengths $\lambda_1 = 1064$ nm and $\lambda_2 = 532$ nm, at an intersecting $\theta = 91^\circ$ angle, as shown in Fig 2.2(a) and (b). With tunable relative phase between two lattices, periodic double wells of various symmetries are formed. As shown in Fig 2.2(c), one can have a symmetric double well, a slightly tilted double well, and a very asymmetric geometry by choosing the phase. Changing the geometry significantly alters the tunneling between the two adjacent wells. Thus, we expect the two particle pairing

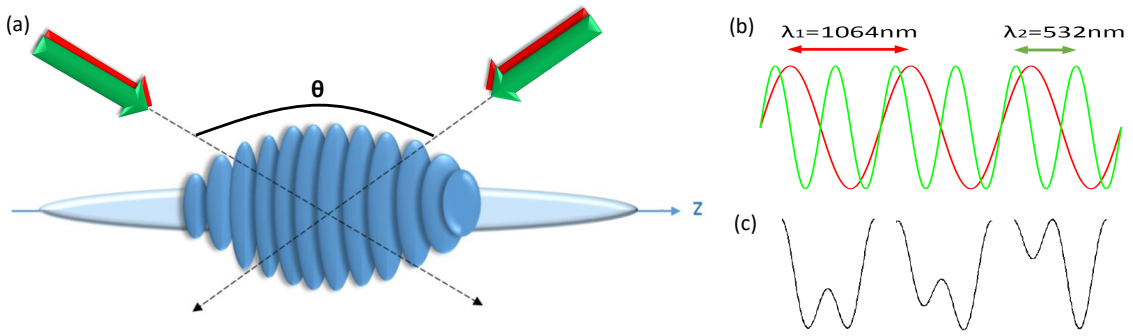

FIGURE 2.2: Bichromatic lattice with tunable relative phase constructed by intersecting two color co-propagating beams. (a) and (b) Two color co-propagating beams of $\lambda_1 = 1064$ nm and $\lambda_2 = 532$ nm, intersecting at $\theta = 91^0$, and superposed on CO_2 laser dipole trap along its axial direction z. (c) Double well of various symmetry are generated by tuning relative phase between two lattices.

is modified. In Ch 5 we describe a Green's function approach to study two particle pairing in a bichromatic lattice in detail. The eigen solutions of the single particle Schrödinger equation are needed to construct the Green's function. In this chapter, we present details of how one calculates the eigenfunctions and eigen-energies for a bichromatic superlattice.

2.1 Optical Dipole Traps

When a neutral atom is in a static electric field, the energy level of the atom shifts because of interaction between the induced dipole moment of the atom and the external field, known as the Stark effect. Similar interactions arise when an optical field is present, where the oscillating electric field generates an induced dipole moment $\mathbf{d} = \alpha\mathbf{E}$, where α is the polarizability of the atom. Interaction between the induced dipole moment and the optical field, known as AC Stark effect, generates a potential for the atoms,

$$V = -\frac{1}{2}\overline{\mathbf{d}\cdot\mathbf{E}}\,. \tag{2.1}$$

The polarizability of the atoms in the ground state is given by

$$\alpha = \frac{1}{\hbar} \sum_e \mu_{eg}^2 \left[\frac{1}{\omega_{eg} - \omega} + \frac{1}{\omega_{eg} + \omega} \right] , \tag{2.2}$$

where μ_{eg} is the electric dipole moment transition matrix element between ground state $|g\rangle$ and excited state $|e\rangle$, and w_{eg} is the associated transition frequency. We can see from eq. 2.2 that the laser frequency should be red detuned for an attractive potential, since then $\omega_{eg} - \omega > 0$ and $\alpha > 0$. For blue detuning, one obtains a repulsive potential, where $\alpha < 0$.

The simplest way to trap atoms is with a focused red-detuned laser beam. For a Gaussian beam which has $1/e$ field radius of w_0, the optical dipole trap has the following form :

$$V(r, z) = -\frac{V_0}{1 + (z/z_R)^2} \, e^{-\frac{2r^2}{w_0^2}}, \tag{2.3}$$

where $z_R = \pi w_0^2/\lambda$ is the Rayleigh length. The trap depth in MKS units is $V_0 = \frac{\alpha I}{2\epsilon_0 c}$, where ϵ_0 is the permittivity of free space and c is the speed of light, and I is the peak laser intensity. In most experiments, the atoms are cooled so that they stay at the bottom of the trap. Then the Gaussian shaped optical potential can be approximated as harmonic in all three directions.

2.2 Bichromatic Lattice Band Theory

Periodic potentials for atoms can be created by interfering two counter-propagating laser beams with the same linear polarization and wavelength to produce a standing wave along the beam propagation direction as described above. The envelope along the beam propagation direction falls off with distance. As can be seen in eq. 2.3, the intensity varies as $1/(1 + (z/z_R)^2)$, with $z_R = \pi w_0^2/\lambda$ being the Rayleigh length, and w_0 being the beam waist ($1/e$ field radius). However, for typical atomic cloud

extensions and beam waists used for optical lattices, this spatial dependence can be neglected. Ignoring the Gaussian envelope along the beam propagation direction and the radial direction, the resulting one dimensional bichromatic optical potential along z can be written as

$$V(z) = V_1 \cos^2(kz) + V_2 \cos^2\left(2kz + \frac{\phi}{2}\right), \tag{2.4}$$

with a depth of $V_1 \equiv -s_1 E_R < 0$ for the red-detuned 1064 nm lattice and $V_2 \equiv s_2 E_R > 0$ for the blue-detuned 532 nm lattice. We define s_1 and s_2, the lattice depth in units of the lattice recoil energy E_R to be positive. By definition the recoil energy is

$$E_R = \frac{\hbar^2 k^2}{2m}, \tag{2.5}$$

where k is the wave vector. Since our lattice is constructed by intersecting two beams at $\theta = 91^\circ$ instead of retro reflection, thus k has to be replaced by k', which is the projected component along the direction of interference, i.e.

$$k' = k \sin\left(\frac{\theta}{2}\right). \tag{2.6}$$

The effective wavelength λ' is

$$\lambda' = \frac{\lambda}{\sin\left(\frac{\theta}{2}\right)}. \tag{2.7}$$

The effective lattice spacing $d = \frac{\lambda'}{2}$ is

$$d = \frac{\lambda'}{2} = \frac{\lambda}{2\sin\left(\frac{\theta}{2}\right)}. \tag{2.8}$$

In solid state physics, the common model used to describe the eigenstates of electrons moving in the periodic potential created by the ions of a metal or crystal

is based on the Bloch theorem [57, 58]. The same formalism can be applied to ultracold atoms in an optical lattice potential, which has translational symmetry $V(z) = V(z + d)$, where d is the lattice spacing.

Before we solve the Schrödinger equation of atoms inside a lattice, it is worth mentioning that we employ the box normalization to get a complete set of orthonormal functions. For a free particle of momentum p inside a box of length L, the wavefunction can be expressed as

$$\Psi(x) = Ae^{i\,p\,x}. \tag{2.9}$$

Box normalization requires

$$\int_{x_0}^{x_0+L} dx' |\Psi(x')|^2 = 1, \tag{2.10}$$

which determines the coefficient $A = \sqrt{\frac{1}{L}}$. For a periodic boundary condition $\Psi(x) = \Psi(x + L)$, one obtains $q = 2\pi m/L$, $-\infty \leqslant m \leqslant \infty$ and $m \in integers$. The states are orthonormal shown as

$$\int_{x_0}^{x_0+L} dx \Psi_p^*(x)\Psi_{p'}(x) = \frac{1}{L}\int_{x_0}^{x_0+L} dx e^{i(p'-p)x} = \delta_{pp'} \tag{2.11}$$

The Schrödinger equation that describes a single particle moving in a 1D periodic lattice potential of size $L = Nd$ is

$$\left[\frac{P^2}{2m} + V(z)\right]\psi = E\psi. \tag{2.12}$$

We can write the single particle wavefunction as a sum over its Fourier components

$$\psi = \sum_p C_p e^{ipz}. \tag{2.13}$$

Since the lattice potential is periodic, it can be written

$$\begin{aligned} V(z) &= \sum_G V_G\, e^{iGz}, \\ G &= n\, G_0,\ n = 0, \pm 1, \pm 2 \ldots\ , \end{aligned} \tag{2.14}$$

where $G_0 = \frac{2\pi}{d}$ is the reciprocal lattice vector and $G\, d = 2n\pi$. Rewriting eq. 2.12 and using eq. 2.13 and eq. 2.14,

$$\sum_p e^{ipz} \left(\frac{\hbar^2 p^2}{2m} - E \right) C_p + \sum_G \sum_{p'} C_{p'} V_G e^{i(p'+G)z} = 0. \tag{2.15}$$

Let $p' + G = p$ in the second term, thus $p' = p - G$. Then

$$\sum_p e^{ipz} \left[\left(\frac{\hbar^2 p^2}{2m} - E \right) C_p + \sum_G C_{p-G} V_G \right] = 0. \tag{2.16}$$

Shifting $p \to p + G_1$ the above expression can be written as

$$\left(\frac{\hbar^2 (p + G_1)^2}{2m} - E^\alpha(p) \right) C^\alpha_{p+G_1} + \sum_G C^\alpha_{p+G_1-G} V_G = 0, \tag{2.17}$$

where α, the band index, denotes the α-th eigenstate $|\alpha, p\rangle \equiv \sum_G C^\alpha_{p-G} |p - G\rangle$ with the corresponding eigenenergy E^α.

It is natural to work in dimensionless units by normalizing to a convenient momentum $k = \frac{\pi}{d}$ and energy scales, the recoil energy $E_R = \hbar^2 k^2 / 2m$. Rewriting eq. 2.17,

$$\left[\left((\widetilde{p} + \widetilde{G_1})^2 - \widetilde{E^\alpha}(\widetilde{p}) \right) C^\alpha_{p+G_1} + \sum_G C^\alpha_{p+G_1-G} \widetilde{V_G} \right] = 0, \tag{2.18}$$

with $\widetilde{p} = p/k$, $\widetilde{E^\alpha} = E^\alpha / E_R$ and $\widetilde{V_G} = V_G / E_R$. The above equation tells us $C^\alpha_{p+G_1}$ couples only to $C^\alpha_{p+G_1-G}$. Therefore the eigenfunction, or Bloch state for a single

particle of selected $p = q$ in a lattice of size $L = Nd$, can be expressed in position representation as

$$\psi_q^\alpha(z) = \sum_G C_{q+G}^\alpha \frac{e^{i(q+G)z}}{\sqrt{Nd}}, \tag{2.19}$$

where N is the total number of lattice sites. Here q is the so called quasi-momentum or lattice momentum.

From the above general expression for the Bloch states, since $G\,d = 2n\pi$, where n is an integer,

$$\psi_q^\alpha(z + d) = e^{iqd}\psi_q^\alpha(z). \tag{2.20}$$

The Bloch state at $z + d$ is the same as Bloch state at z with a phase shift of e^{iqd}. This is often expressed as $\psi_q^\alpha(z) = e^{ik\cdot z}u_q(z)$, where $u_q(z + d) = u_q(z)$ is periodic. The eigenstates are superposition of plane waves whose amplitudes are modulated with the same periodicity as the lattice potential.

By shifting q to $q + G_1$ in eq. 2.19, and noting that the summation is over all reciprocal lattice vectors G_1, the sum remains the same, so that

$$\psi_{q+G_1}^\alpha(z) = \psi_q^\alpha(z). \tag{2.21}$$

Here the Bloch state is periodic in quasi-momentum q with a periodicity of G_0, the reciprocal lattice vector. Inserting $\Psi_{q+G}(z)$ in the Schrödinger equation eq. 2.12, we have

$$E(q + G) = E(q). \tag{2.22}$$

The eigenenergy is also periodic in quasi-momentum q, and repeats after $q + G_0$. Notice that the symmetry in quasi-momentum space allows one to restrict q inside the first Brillouin zone, i.e. $\frac{-G_0}{2} = -\frac{\pi}{d} < q < \frac{G_0}{2} = \frac{\pi}{d}$, to avoid redundancy when specifying all Bloch states. Which leads to $q = \frac{2\pi m}{Nd}$ with $\frac{-N}{2} < m < \frac{N}{2} - 1$, where N is an even integer.

Note that Bloch states are orthonormal as shown in the following. Define the integral $I^{\alpha,\alpha'}_{q,q'}$ over the lattice of length Nd as

$$\begin{aligned} I^{\alpha,\alpha'}_{q,q'} &\equiv \int_0^{Nd} dx \Psi^{\alpha'*}_{q'}(x)\Psi^{\alpha}_{q}(x) \\ &= \delta_{\alpha'\alpha}\sum_{n=0}^{N-1}\int_{nd}^{nd+d} dx\, \Psi^{\alpha}_{q}(x)\Psi^{\alpha}_{q'}(x) \\ &= \delta_{\alpha'\alpha}\sum_{n=0}^{N-1}\int_{0}^{d} dx'\, \Psi^{\alpha}_{q}(x'+nd)\Psi^{\alpha}_{q'}(x'+nd) \\ &= \delta_{\alpha'\alpha}\sum_{n=0}^{N-1} e^{i(q-q')nd}\sum_{G,G'} C^{\alpha}_{G}(q)C^{\alpha}_{G'}{}^{*}(q')\int_0^d dx'\,\frac{e^{i(q-q'+G-G')x'}}{Nd}, \end{aligned} \tag{2.23}$$

where $\delta_{\alpha,\alpha'}$ comes in naturally by assuming these states are non-degenerate, i.e. $E^{\alpha} \neq E^{\alpha'}$. After a change of variable, notice that the sum over n forms a geometric series. Recall $q = \frac{2\pi m}{Nd}, m \in integer$, the geometric sum reduces to a Kronecker delta $\delta_{q'q}$ as

$$\sum_{n=0}^{N-1} e^{ind(q-q')} = \frac{1-e^{iNd(q-q')}}{1-e^{id(q-q')}} = N\delta_{qq'}. \tag{2.24}$$

Eq. 2.23 is then

$$I^{\alpha,\alpha'}_{q,q'} = \delta_{\alpha'\alpha}\delta_{qq'}\sum_{G,G'} C^{\alpha}_{G}(q)C^{\alpha}_{G'}{}^{*}(q')\int_0^d \frac{dx'}{d}\, e^{i(G-G')x'}. \tag{2.25}$$

Since $(G-G')d = 2\pi(n-n')$, then the integral $\int_0^d \frac{dx'}{d}\, e^{i(G-G')x'} = \delta_{G,G'}$.

$$I^{\alpha,\alpha'}_{q,q'} \equiv \int_0^{Nd} dx \Psi^{\alpha'*}_{q'}(x)\Psi^{\alpha}_{q}(x) = \delta_{\alpha'\alpha}\delta_{qq'}\sum_{G}|C^{\alpha}_{G}(q)|^2, \tag{2.26}$$

where $\sum_G |C^{\alpha}_{G}(q)|^2 = 1$ for normalized states.

We can rewrite the one dimensional bichromatic lattice potential given in eq. 2.4.

Ignoring the constant offset $\frac{V_1+V_2}{2}$ and substituting $2k = G_0$.[1]

$$V(z) = \frac{V_1}{4}\left(e^{iG_0 z} + e^{-iG_0 z}\right) + \frac{V_2}{4}\left(e^{i(2G_0 z+\phi)} + e^{-i(2G_0 z+\phi)}\right). \tag{2.27}$$

Using the form of eq. 2.14, $V_G = \sum_G V_G e^{iG\cdot z}$, we have

$$V_G = \frac{V_1}{4}\delta_{G,G_0} + \frac{V_1}{4}\delta_{G,-G_0} + \frac{V_2 e^{i\phi}}{4}\delta_{G,2G_0} + \frac{V_2 e^{-i\phi}}{4}\delta_{G,-2G_0}. \tag{2.28}$$

The fundamental lattice potential part, i.e. $\cos^2(kz)$, allows only coupling between $|q\rangle$ and $|q \pm G_0\rangle$, whereas the secondary lattice potential, i.e. $\cos^2(2kz + \frac{\phi}{2})$, allows coupling only between $|q\rangle$ and $|q \pm 2G_0\rangle$.

We can rewrite eq. 2.18 using eq. 2.28 to obtain the dimensionless matrix

$$\begin{aligned} &H[M, G_1, G_2, \tilde{q}, s_1, s_2, \phi] \\ &= (\tilde{q} + 2(G_1 - 1 - M))^2 \delta_{G_1,G_2} + \frac{-s_1}{4}\delta_{G_1+1,G_2} + \frac{-s_1}{4}\delta_{G_1-1,G_2} \\ &\quad + \frac{s_2}{4}e^{-i\phi}\delta_{G_1+2,G_2} + \frac{s_2}{4}e^{i\phi}\delta_{G_1-2,G_2}, \end{aligned} \tag{2.29}$$

where $G_1, G_2 \in integers$ and $1 \leqslant G_1, G_2 \leqslant 2M+1$ for a $(2M+1)$ band model. Recall that $V_1 = -s_1 E_R$ and $V_2 = s_2 E_R$ with s_1 and s_2 being normalized lattice depth.

For a 5 band model with higher bands truncated, the matrix equation with $M = 2$ is

$$\begin{bmatrix} (\tilde{q}-4)^2 & \frac{-s_1}{4} & \frac{s_2}{4}e^{-i\phi} & 0 & 0 \\ \frac{-s_1}{4} & (\tilde{q}-2)^2 & \frac{-s_1}{4} & \frac{s_2}{4}e^{-i\phi} & 0 \\ \frac{s_2}{4}e^{i\phi} & \frac{-s_1}{4} & \tilde{q}^2 & \frac{-s_1}{4} & \frac{s_2}{4}e^{-i\phi} \\ 0 & \frac{s_2}{4}e^{i\phi} & \frac{-s_1}{4} & (\tilde{q}+2)^2 & \frac{-s_1}{4} \\ 0 & 0 & \frac{s_2}{4}e^{i\phi} & \frac{-s_1}{4} & (\tilde{q}+4)^2 \end{bmatrix} \begin{bmatrix} C^\alpha_{\tilde{q}-4} \\ C^\alpha_{\tilde{q}-2} \\ C^\alpha_{\tilde{q}} \\ C^\alpha_{\tilde{q}+2} \\ C^\alpha_{\tilde{q}+4} \end{bmatrix} = \widetilde{E^\alpha} \begin{bmatrix} C^\alpha_{\tilde{q}-4} \\ C^\alpha_{\tilde{q}-2} \\ C^\alpha_{\tilde{q}} \\ C^\alpha_{\tilde{q}+2} \\ C^\alpha_{\tilde{q}+4} \end{bmatrix} \tag{2.30}$$

We first show in Fig 2.3 the energy versus quasi-momentum q for a 5-band calculation in the first Brillouin zone for a single lattice, i.e. $s_2 = 0$, with increasing

[1] Since $d = \frac{\lambda'}{2}$, $G_0 = \frac{2\pi}{d} = \frac{\pi}{\lambda} = 2k'$, here $k' = k\sin\left(\frac{\theta}{2}\right)$. For consistent notation, we write effect wave vector as k instead of k' in the text.

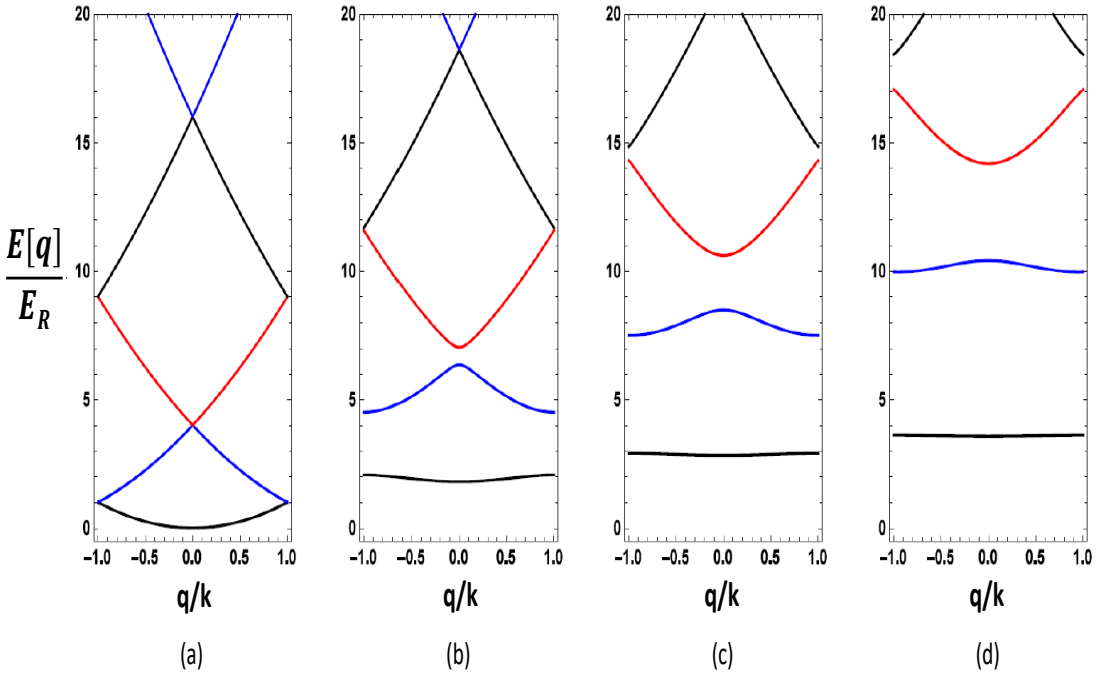

FIGURE 2.3: The band structure of a single color lattice of (a) $s_1 = 0$, (b) $s_1 = 5$, (c) $s_1 = 10$, and (d) $s_1 = 15$ respectively calculated using a 5-band model.

lattice depth from $s_1 = 0$ to 15. Each energy band is labeled with a different color. For $s_1 = 0$ the energy momentum dispersion is quadratic, as for a free particle. With increasing the lattice depth, the bands flatten out and open up energy gaps between the bands.

We compare the lattice potential and the band structure of the fundamental lattice of $s_1 = 10$ to that of the bichromatic lattices of $s_1 = 10$, $s_2 = 20$, $\phi = 0$, $2\pi/35$, or π in Fig 2.4(a) through (d). As can be seen from the figure below, one creates a periodic symmetric double well superlattice by choosing the relative phase $\phi = 0$. Notice that the lowest two energy bands are brought close to degeneracy. A tiny phase deviation from zero, for example $\phi = 2\pi/35$, almost does not change either the lattice potential geometry or the band structure.

To get a physical insight, we solve the Schrödinger equation for a single site of the

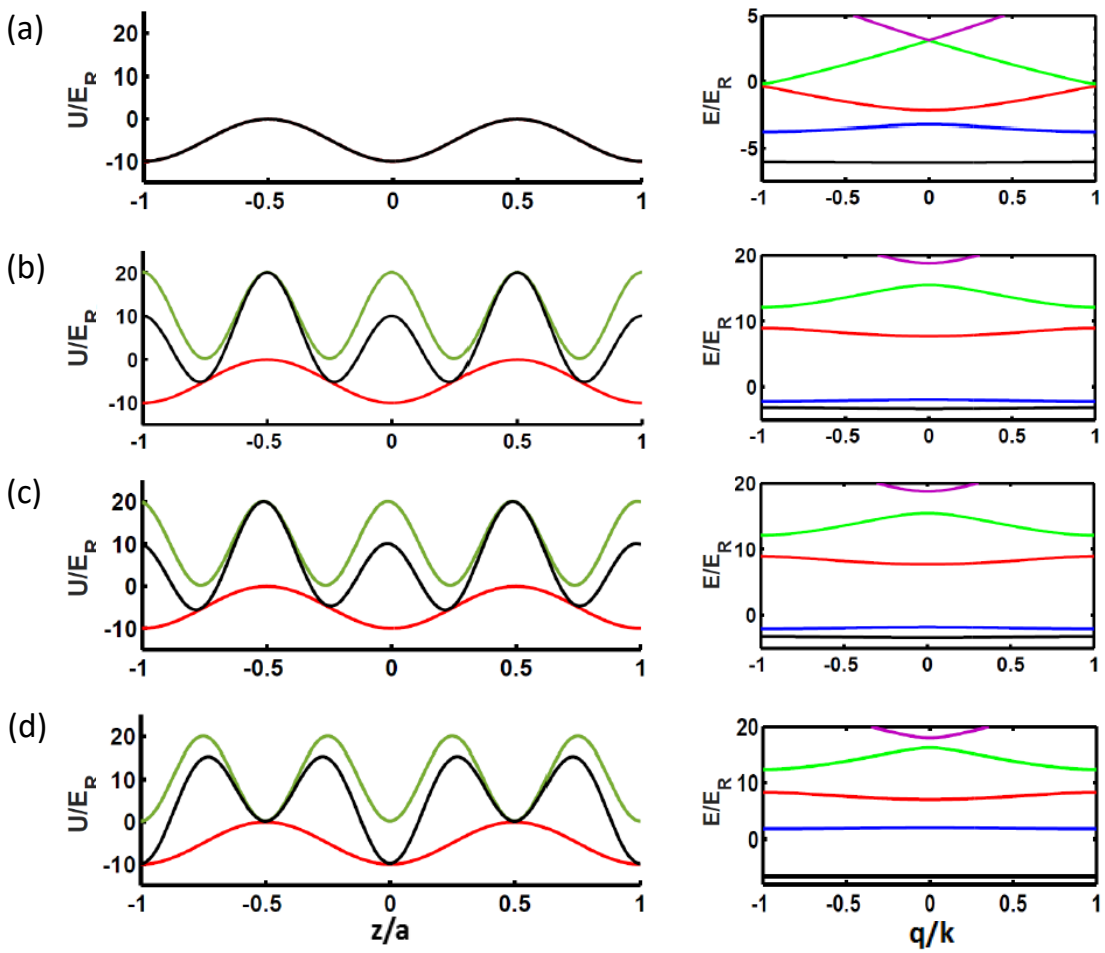

FIGURE 2.4: Comparison of lattice potential (left) and band structure (right) between (a) the fundamental lattice of $s_1 = 10$ and (b) the bichromatic lattice of $s_1 = 10, s_2 = 20$, $\phi = 0$, (c) $\phi = 2\pi/35$, or (d) $\phi = \pi$. The left column shows lattice potential in units of E_R of the $\lambda_1 = 1064$ nm lattice, as described in eq. 2.5 and eq. 2.6. Where $\lambda_1 = 1064$ nm lattice is labeled red, $\lambda_2 = 532$ nm lattice is labeled green, and the overall lattice is labeled black. The right column shows the band structure, where all bands are labeled with different colors. Notice for (b) $\phi = 0$ and (c) $\phi = 2\pi/35$, the lowest two bands are almost degenerate.

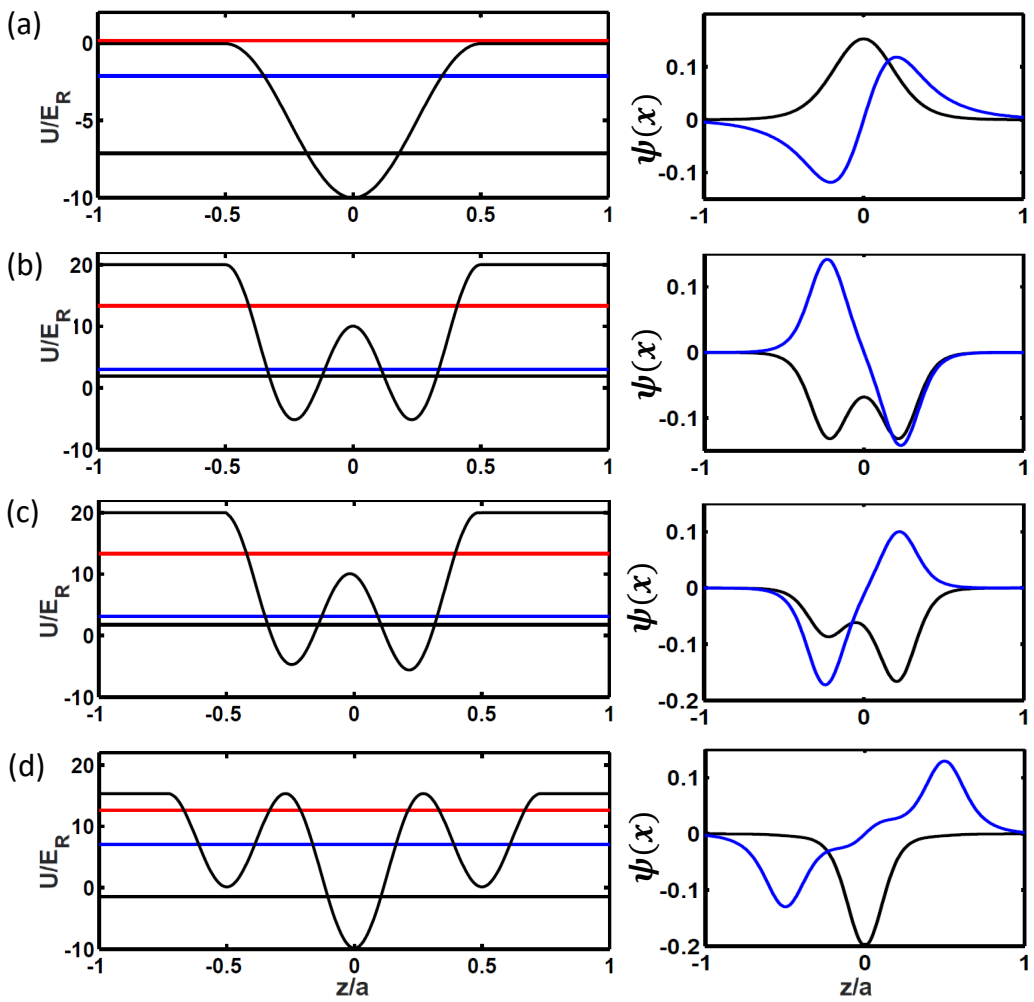

FIGURE 2.5: Eigensolutions to the Schrödinger equation for a single lattice site of (a) the fundamental lattice of $s_1 = 10$ and (b) the bichromatic lattice of $s_1 = 10, s_2 = 20$, $\phi = 0$, (c) $\phi = 2\pi/35$, or (d) $\phi = \pi$. In the left column the horizontal lines labeled on the single site lattice potential (black curve), are the lowest three eigenenergies in units of E_R. The eigenfunctions of the ground state and the first excited state, labeled black and blue, are plotted in the right column.

superlattice, rather than treating it as a lattice with periodic boundary conditions. Using the same parameters as in Fig 2.4, results for the lowest three eigenenergies and two eigenfunctions corresponding to the lowest two energies are shown in Fig 2.5. Once again, we see the lowest two energy bands became degenerate when a symmetric double is formed for relative phase $\phi = 0$. Comparing right column of Fig 2.5(a) and (b), one finds the double well structure changes the ground state wavefunction

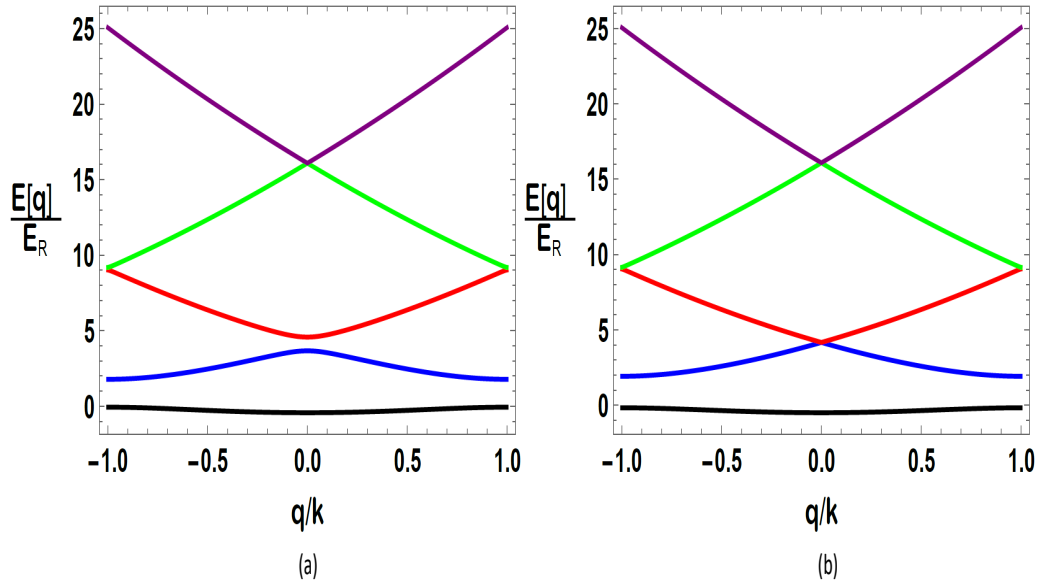

FIGURE 2.6: Generating a Dirac point in a bichromatic lattice. Band structure of bichromatic lattice of $s_1 = 4$, $s_2 = 1$, (a) $\phi = 0$, and (b) $\phi = \pi$. For $\phi = \pi$, a Dirac point occurs between the 2nd and 3rd band at the Brillouin zone center where the two bands cross and the dispersion is linear.

significantly. With an almost non-existing phase shift of $\phi = 2\pi/35$, one can barely tell any change in the lattice potential and the eigenenergies. However, the symmetry of the ground state wavefunction is notably modified when comparing Fig 2.5(b) and (c). For $\phi = \pi$, the ground state degeneracy is lifted, and the wavefunction resembles that of a fundamental lattice.

We show in Fig 2.6 (a) and (b) that by properly choosing $s_1 = 4$, $s_2 = 1$ and $\phi = \pi$, a Dirac point occurs between the second and third band at the Brillouin zone center. The energy versus quasi-momentum dependence is linear, which mimics that of a relativistic particle. A more detailed discussion is presented in Sec 6.2.1.

2.3 Quasi-momentum Distributions

Experimentally we control the chemical potential to control the band population. In order to determine the chemical potential of the system with atoms loaded into

the lattice, it is important to measure the quasi-momentum distribution of the gas by doing a band map. Band mapping is accomplished by ramping down the lattice potential gradually on a timescale that is fast compared to the tunneling timescale in the lowest band of the lattice, but adiabatic with respect to interband transitions [59, 60]. By doing so, the Bloch waves are adiabatically transferred into plane waves and the initial quasi-momentum distribution becomes the final momentum distribution, which we measure with a time-of-flight absorption image.

To measure quasi-momentum distributions of atoms, most groups turn off all traps and allow the atoms to expand freely for a time-of-flight before imaging the density distribution. During the expansion, there should be no interactions between the atoms in order to preserve their initial momentum. In our lab, we do not have the capability to turn off the magnetic trap completely in a short time, and also ^{6}Li atoms are much lighter than, for example ^{40}K. They tend to quickly fly outside the accessible image region and can no longer be captured by the camera. Inspired by Jochim's work [7], and to accommodate what we have, we developed a new method to measure the quasi-momentum distribution inside a harmonic trap. The harmonic trap in which we conduct a band map is composed of the magnetic field curvature and an adjustable power CO_2 laser axial confinement. The advantages of band mapping in a CO_2 laser harmonic trap include the enhancement of signal to noise ratio due to the radial confinement, and the flexible choice of band mapping time with the help of the CO_2 laser trap axial confinement. By letting the cloud expand in the harmonic trap for one quarter period, $t = T/4$, the spatial density distribution reveals the momentum distribution at time zero, regardless of its initial position distribution. With this technique, one can measure the population in all Bloch bands, which show up in the higher Brillouin zones in the band map picture.

A simple physical picture is the following: The equation of motion of a classical

particle moving in a harmonic trap is

$$x(t) = x_0 \cos \omega t + \frac{p_0}{mw} \sin \omega t, \tag{2.31}$$

with x_0 the initial position, p_0 the initial momentum and ω the trap frequency. After one quarter period $t = \frac{T}{4}$, $\omega T/4 = \pi/2$,

$$x\left(t = \frac{T}{4}\right) = \frac{p_0}{m\omega}. \tag{2.32}$$

The position at $\frac{T}{4}$ is the initial momentum, independent of x_0.

From a quantum mechanical point of view, one can describe the momentum distribution measurement generally using the Wigner function formalism. The Wigner function $W(x, p, t)$ represents the phase space density distribution at time t, and is defined as

$$W(x, p, t) \equiv \sum_{\Psi} P_{\Psi} \int_{-\infty}^{\infty} d\epsilon \, \frac{e^{i\epsilon p/\hbar}}{2\pi\hbar} \Psi^* \left(x + \frac{\epsilon}{2}, t\right) \Psi \left(x - \frac{\epsilon}{2}, t\right). \tag{2.33}$$

Here Ψ is the wavefunction and x and p are position and momentum. For an ensemble, the Wigner function is summed over all possible states $\Psi(x, t)$ with probability P_{Ψ}.

Integrating $W(x, p, t)$ over p or x one obtains the position or the momentum distribution,

$$\begin{aligned} W_x(x, t) &\equiv \int_{-\infty}^{\infty} dp \, W(x, p, t) = \sum_{\Psi} P_{\Psi} |\Psi(x, t)|^2, \\ W_p(p, t) &\equiv \int_{-\infty}^{\infty} dx \, W(x, p, t) = \sum_{\Psi} P_{\Psi} |\Psi(p, t)|^2. \end{aligned} \tag{2.34}$$

From the time-dependent Schrödinger equation

$$i\hbar \frac{\partial \Psi}{\partial t} = -\frac{\hbar^2}{2m} \frac{\partial^2 \Psi}{\partial x^2} + V(x) \Psi, \tag{2.35}$$

and eq. 2.33, one easily obtains the general equation of motion of the Wigner function for any external potential $V(x)$.

$$\frac{\partial W(x,p,t)}{\partial t} + \frac{p}{m}\frac{\partial W(x,p,t)}{\partial x} - \frac{\partial V(x)}{\partial x}\frac{\partial W(x,p,t)}{\partial p}$$
$$= \sum_{s=1}^{\infty} \left(\frac{\hbar}{2}\right)^{2s} \frac{1}{(2s+1)!}\frac{\partial^{2s+1}V(x)}{\partial x^{2s+1}}\frac{\partial^{2s+1}W(x,p,t)}{\partial p^{2s+1}}. \tag{2.36}$$

For any linear potential $V(x) = Fx$, or quadratic potential $V(x) = kx^2$, the right hand side of eq. 2.36 vanishes.

Let's look closely at the case where $V(x) = \frac{1}{2}m\omega_0^2 x^2$, since in our experiment, the atomic gas is released into a harmonic potential coming from the CO_2 laser dipole trap and the magnetic bowl. Assuming $W(x,p,t) = W(f(x,p,t), g(x,p,t))$, we require

$$\frac{\partial W}{\partial f}\left[\frac{\partial f}{\partial t} + \frac{p}{m}\frac{\partial f}{\partial x} - m\omega_0^2 x\frac{\partial f}{\partial p}\right] = 0,$$
$$\frac{\partial W}{\partial g}\left[\frac{\partial g}{\partial t} + \frac{p}{m}\frac{\partial g}{\partial x} - m\omega_0^2 x\frac{\partial g}{\partial p}\right] = 0. \tag{2.37}$$

The solutions of the above coupled differential equations are

$$f(x,p,t) = x\cos(\omega_0 t) - \frac{p}{m\omega_0}\sin(\omega_0 t),$$
$$g(x,p,t) = m\omega_0 x\sin(\omega_0 t) + p\cos(\omega_0 t). \tag{2.38}$$

Notice at zero time $f(x,p,t=0) = x_0$ and $g(x,p,t=0) = p_0$, f and p reduces to position and momentum at zero time. For small $w_0 t$, $f = x_0 - \frac{p_0}{m}t$, and $g = p_0 + m\omega_0^2 x_0 t$. Thus, the Wigner function at time t is related to its value at $t = 0$, where $W^{(0)}[x,p] \equiv W(x,p,t=0)$ via the following expression,

$$W(x,p,t) = W^{(0)}\left[x\cos(w_0 t) - \frac{p}{m\omega_0}\sin(\omega_0 t),\ m\omega_0 x\sin(\omega_0 t) + p\cos(\omega_0 t)\right]. \tag{2.39}$$

For an evolution times of 1/4 the trap period [61], where $\omega_0 t = \frac{\pi}{2}$

$$W\left(x, p, \frac{T}{4}\right) = W^{(0)}\left[-\frac{p}{mw_0},\ mw_0 x\right] . \tag{2.40}$$

Integrating over p,

$$W_x\left(x, \frac{T}{4}\right) = mw_0 W_p^{(0)}\left[mw_0 x\right]. \tag{2.41}$$

We see that the normalized position distribution at $T/4$ is equal to the normalized momentum distribution at $t = 0$ with $p = mw_0 x$.

By adiabatically lowering the optical lattice, we convert the quasi-momentum into momentum. Releasing the cloud into the harmonic trap for $T/4$ before taking an absorption image, we obtain the band map of the non-interacting gas. The number of particles in each band and quasi-momentum can thus be measured. Details of band map experiments are presented in Sec 3.7.

One can numerically simulate the momentum or quasi-momentum distribution for a Bloch state $\Psi_q^\alpha(x)$. The corresponding Wigner function for a Bloch state following the definition in eq. 2.33 is

$$\begin{aligned} W(x,p) &= \sum_{G,G'} C_{G'}^{\alpha\,*} C_G^\alpha \frac{e^{i(G-G')x}}{Nd} \frac{1}{2\pi} \int_{-\frac{Nd}{2}}^{\frac{Nd}{2}} d\epsilon\, e^{i\epsilon(p-q-\frac{G+G'}{2})} \\ &= \sum_{G,G'} C_{G'}^{\alpha\,*} C_G^\alpha \frac{e^{i(G-G')x}}{Nd} \frac{1}{2\pi} \frac{\sin\left[\frac{Nd}{2}(p-q-\frac{G+G'}{2})\right]}{\frac{Nd}{2}(p-q-\frac{G+G'}{2})} . \end{aligned} \tag{2.42}$$

The momentum distribution for the Bloch state is then

$$\begin{aligned} W_q^\alpha(p) &= \int_{-\frac{Nd}{2}}^{\frac{Nd}{2}} dx\, W(x,p) \\ &= \sum_{G,G'} C_{G'}^{\alpha\,*} C_G^\alpha\, I_{G,G'}\, \frac{1}{2\pi} \frac{\sin\left[\frac{Nd}{2}(p-q-\frac{G+G'}{2})\right]}{\frac{Nd}{2}(p-q-\frac{G+G'}{2})} . \end{aligned} \tag{2.43}$$

The integral

$$I_{G,G'} \equiv \int_{-\frac{Nd}{2}}^{\frac{Nd}{2}} dx\, e^{i(G-G')x} = \frac{e^{i(G-G')\frac{Nd}{2}} - e^{-i(G-G')\frac{Nd}{2}}}{2i(G-G')\frac{Nd}{2}} Nd = Nd\,\delta_{G,G'}\ , \qquad (2.44)$$

since $(G-G')\frac{Nd}{2} = \frac{2\pi}{d}(n-n')\frac{Nd}{2} = (n-n')N\pi$, $N \in\ even$[2] and $n, n' \in$ integers. Eq. 2.43 becomes

$$\begin{aligned} W_q^\alpha(p) &= \sum_G\ |C_G^\alpha(q)|^2\ \frac{Nd}{2\pi} \frac{\sin\left(\frac{Nd}{2}(p-q-G)\right)}{\frac{Nd}{2}(p-q-G)} \\ &= \sum_G\ |C_G^\alpha(q)|^2\ \delta(p-q-G), \end{aligned} \qquad (2.45)$$

where the $\delta(p-q-G)$ comes from the limit $Nd \to \infty$.

To calculate the momentum distribution, we need to determine the chemical potential, including the Bloch states and the transverse harmonic states in the radial direction. For transverse harmonic confinement with harmonic frequency $\omega_\perp$, the transverse density of states is $\mathcal{D}(\epsilon_\perp) = \frac{\epsilon_\perp}{(\hbar w_\perp)^2}$. For each Ψ_q^α state with energy E_q^α, the allowed radial energies for a given global chemical potential μ are limited by $0 \leqslant \epsilon_\perp \leqslant \mu - E^\alpha(q)$. Summing over all α, q states, the total number of states equals to the total number of atoms of one spin state $N_\uparrow$,

$$\begin{aligned} N_\uparrow &= \sum_{\alpha,q} \int_0^\mu d\epsilon_\perp \mathcal{D}(\epsilon_\perp)\, \Theta\left[\mu - E^\alpha(q) - \epsilon_\perp\right] \\ &= \sum_{\alpha,q} \frac{\left[\mu - E^\alpha(q)\right]^2}{2\left(\hbar w_\perp\right)^2} \Theta\left[\mu - E^\alpha(q)\right]. \end{aligned} \qquad (2.46)$$

The probability of being in Bloch state Ψ_q^α given the global chemical potential μ is then

$$P_\alpha^\mu(q) = \frac{\left[\mu - E^\alpha(q)\right]^2}{NE_F^2} \Theta\left[\mu - E^\alpha(q)\right] \Theta[1 - (q/k)^2], \qquad (2.47)$$

[2] Recall that quasi-momentum is restricted within the 1st Brillouin zone, i.e. $\frac{-G_0}{2} < q = 2\pi m/Nd < \frac{G_0}{2}$. Therefore $\frac{-N}{2} < m < \frac{N}{2} - 1$ with N being even numbers.

with N being the number of lattice sites and $E_F = \hbar\omega_\perp\sqrt{\frac{2N_\uparrow}{N}}$ being the local radial Fermi energy at each lattice site. Notice that $\frac{N_\uparrow}{N}$ is the number of spin up state per site, and the theta function restricts the range of q to be within the fist Brillouin zone.

With a little algebra, one can rewrite the above equation in dimensionless form, where all energies are expressed in units of E_R and quasi-momentum q is in units of the wave vector k, i.e., $\mu = \widetilde{\mu}\, E_R$, $E_F = \widetilde{E_F}\, E_R$, $E^\alpha(q) = \widetilde{E}^\alpha(\widetilde{q})\, E_R$.

$$1 = \frac{1}{\widetilde{E_F}^2}\sum_\alpha \frac{1}{N}\sum_{n=-N/2}^{N/2}\left[\widetilde{\mu} - \widetilde{E}^\alpha\left(\frac{2n}{N}\right)\right]^2 \Theta\left[\widetilde{\mu} - \widetilde{E}^\alpha\left(\frac{2n}{N}\right)\right] \tag{2.48}$$

Given a global chemical potential $\tilde{\mu}$, one can use the above equation to solve for the radial Fermi energy $\widetilde{E_F}$ or vice versa. The probability distribution in normalized units is then

$$P_\alpha^\mu(\widetilde{q}) \;\; = \frac{\left[\widetilde{\mu} - \widetilde{E}^\alpha(\widetilde{q})\right]^2}{\widetilde{E_F}^2}\Theta\left[\widetilde{\mu} - \widetilde{E}^\alpha(\widetilde{q})\right]\Theta\left[1 - \widetilde{q}^2\right], \tag{2.49}$$

where $\int_0^1 d\widetilde{q} P_\alpha^\mu(\widetilde{q}) = 1$.

With eq. 2.49 one can plot the probability distribution within the first Brillouin zone for each band, as shown in Fig 2.7. The band probability distributions are calculated for a lattice depth of $s_1 = 20$, number of lattice sites $N = 500$, chemical potential of $\mu = 3\, E_R$, $10\, E_R$, and $15\, E_R$ respectively. The radial Fermi energy is calculated to be $8.83\, E_R$, $17.74\, E_R$, $25.38\, E_R$ based on the given parameters and the normalization condition. The probability of occupying higher bands is enhanced by increasing the chemical potential.

Using the probability distribution function in eq. 2.49, one can obtain the normalized average momentum distribution by summing over the Wigner function $W_q^\alpha(p)$

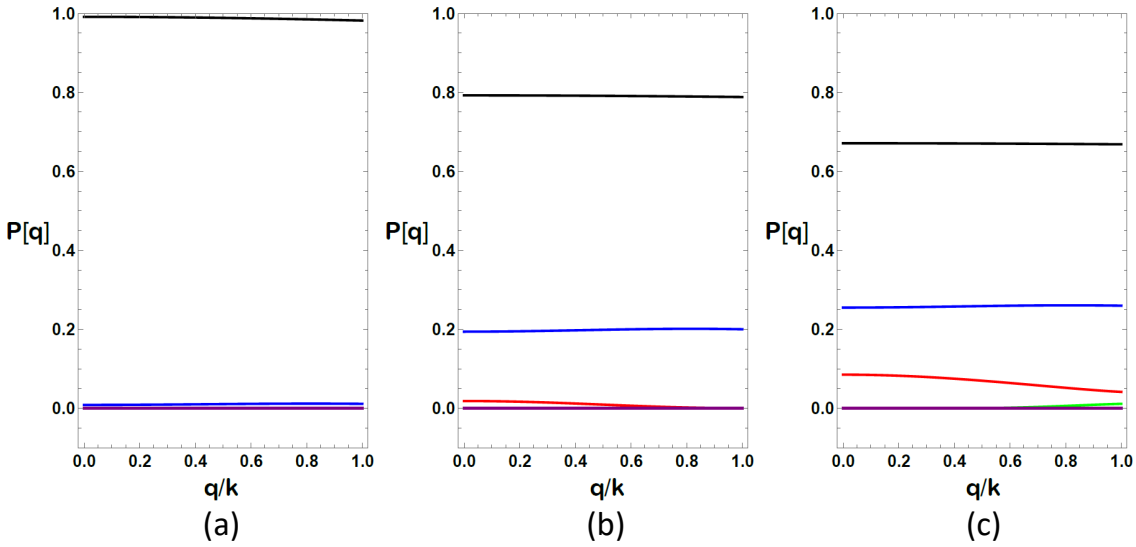

FIGURE 2.7: The band probability distribution within the first Brillouin zone calculated for a lattice depth of $s_1 = 20$, number of lattice sites $N = 500$, chemical potential of $\mu = 3E_R$, $10E_R$, and $15E_R$ respectively. Various colors refers to different bands: Black is the first band, blue is the second, red is the third, green is the fourth, purple is the fifth.

for each Bloch state Ψ_q^α, i.e. $\widetilde{W}(p) = \sum_{\alpha,q} P_\alpha^\mu(q) W_q^\alpha(p)$. In normalized units,

$$\widetilde{W}(\widetilde{p}) \quad = \tfrac{1}{2} \sum_\alpha \sum_G \; |C_G^\alpha(\widetilde{q})|^2 P_\alpha^\mu(\widetilde{q})\, \delta(\widetilde{p} - \widetilde{q} - \widetilde{G}) \tag{2.50}$$

Notice the factor $\frac{1}{2}$ comes from the symmetric normalization $\int_{-\infty}^{\infty} \widetilde{W}(\widetilde{p})\, d\widetilde{p} = 1$. With this expression, we can plot the momentum or the quasi-momentum distribution. The momentum distribution, labeled as blue in Fig 2.8, corresponds to abruptly turning off of the lattice, thus the coefficients C_G^α in eq. 2.49 are evaluated for the given lattice depth.

The quasi-momentum distribution, labeled as red in Fig 2.8, corresponds to adiabatic lowering of the lattice to a shallow depth before releasing the cloud, where the coefficients C_G^α are evaluated at $s_1 = 0.01$. The energy momentum dispersion for a zero lattice depth is quadratic, the same as for free particles. Therefore the

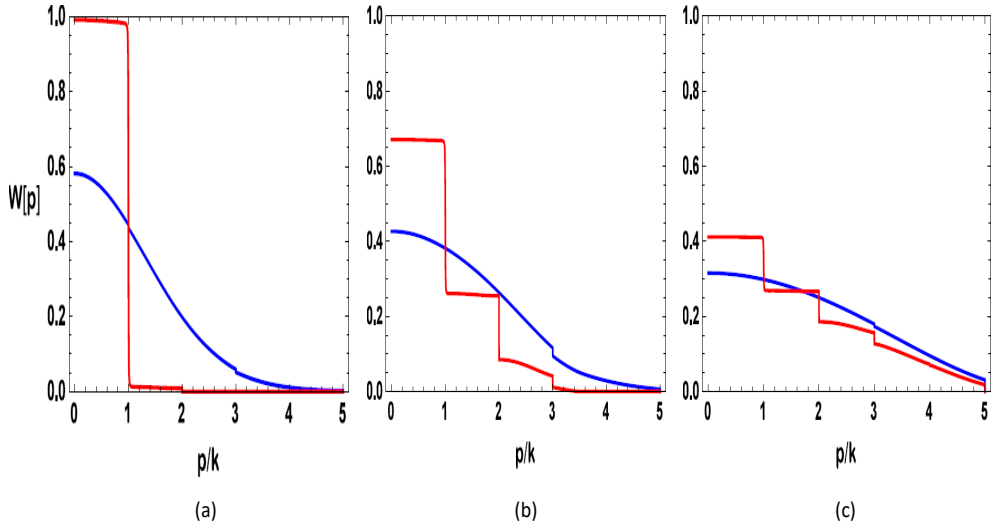

FIGURE 2.8: The normalized momentum and quasi-momentum distributions of atoms inside a lattice. The momentum distribution (blue, corresponding to abrupt turn off of the lattice) and the quasi-momentum distribution (red, corresponding to adiabatic lowering of the lattice) in normalized units calculated for a lattice depth of $s_1 = 20$, number of lattice sites $N = 500$, chemical potential of (a)$\mu = 3E_R$, (b)$15E_R$, and (c)$35E_R$ respectively.

coefficients C_G^α are

$$\begin{aligned} C^1_{G_1} &= \delta_{G_1,0} \ ; \\ C^2_{G_1}(q_1) &= \delta_{G_1,-G_0}\Theta[q_1] + \delta_{G_1,G_0}\Theta[-q_1] \ ; \\ C^3_{G_1}(q_1) &= \delta_{G_1,G_0}\Theta[q_1] + \delta_{G_1,-G_0}\Theta[-q_1] \ ; \end{aligned} \tag{2.51}$$

similarly for all the higher bands $\alpha = 4, 5.....$ Therefore, the normalized momentum distribution, which determines the band map, is

$$\begin{aligned} \widetilde{W}(\widetilde{p}) = \frac{1}{2}(P^\mu_0(\widetilde{p}) + \Theta[\widetilde{p}+\widetilde{G_0}]P^\mu_2(\widetilde{p}+\widetilde{G_0}) + \Theta[-\widetilde{p}+\widetilde{G_0}]P^\mu_2(\widetilde{p}-\widetilde{G_0}) \\ +\Theta[\widetilde{p}-\widetilde{G_0}]P^\mu_3(\widetilde{p}-\widetilde{G_0}) + \Theta[-\widetilde{p}-\widetilde{G_0}]P^\mu_3(\widetilde{p}+\widetilde{G_0}) + ...). \end{aligned} \tag{2.52}$$

One can see that the theta functions map out the probability distributions of each band in the regions $\widetilde{p} \pm n\widetilde{G_0}$.

The distributions shown in Fig 2.8 are calculated for a lattice depth of $s_1 = 20$, number of lattice sites $N = 500$, and chemical potential of $\mu = 3E_R$, $15E_R$, and $35E_R$ respectively. The corresponding radial Fermi energies are calculated to be $8.83E_R$, $25.38E_R$, $63.57E_R$ based on the given parameters for the normalization condition. The shoulders of red plateaus show up at multiples of p/k, which corresponds to various Brillouin zone boundaries. Once again, we see the effect of occupying higher bands due to the increase of the chemical potential. The quasi-momentum distribution looks more and more like a Gaussian shaped momentum distribution as one keeps raising the chemical potential to fill up more bands.

Details of the band map experiments for the infrared lattice, the green lattice and the bichromatic lattice are reported in Sec 3.7.

2.4 Lattice Modulation

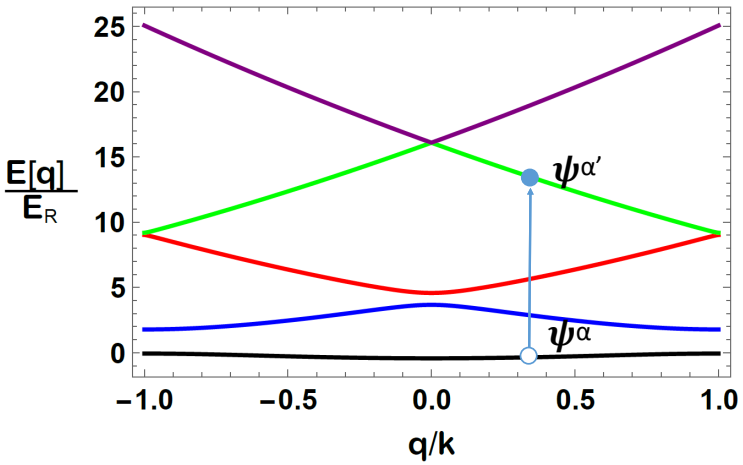

FIGURE 2.9: The interband transition between states Ψ^{α} and $\Psi^{\alpha'}$ induced by lattice depth sinusoidal modulation preserves quasi-momentum.

In this section we study inducing transitions between different bands by periodically modulating the lattice depth. Due to the translational symmetry of the lattice potential, only transitions between different energy bands that conserves quasi-

momentum are allowed, as illustrated in Fig 2.9. We will give a detailed derivation below. Thus one can treat such modulation process as a transition for a two-level system.

We can incorporate the modulation by adding a time-dependent oscillating perturbation to the lattice potential,

$$H = \frac{p^2}{2m} + V(x)(1 + \epsilon\cos(\omega t)) \tag{2.53}$$

where $H_0 = \frac{p^2}{2m} + V(x)$ is the unperturbed Hamiltonian and $H' = \epsilon V(x)\cos(\omega t)$ is the perturbation, with ϵ being small.

We can define an effective Rabi frequency Ω as

$$\Omega = \Omega^{\alpha'\alpha}(q) = \frac{1}{\hbar}\,\epsilon\, T^{\alpha'\alpha}_{q'=q}, \tag{2.54}$$

for a transition between E^{α}_q and $E^{\alpha'}_q$ at quasi-momentum q. The transition matrix element $T^{\alpha'\alpha}_{q'=q}$ will be defined below in eq. 2.58. The time-dependent transition probability can be expressed as

$$P^{\alpha,\alpha'}(\epsilon,\omega,\tau,q) = \frac{\Omega^2}{\Omega'^2}\sin^2\left(\frac{\Omega'\tau}{2}\right). \tag{2.55}$$

Here $\Omega' = \sqrt{\Omega^2 + \Delta^2}$, the detuning is $\Delta = \Delta^{\alpha'\alpha}(q) \equiv \omega - \frac{E^{\alpha'}(q) - E^{\alpha}(q)}{\hbar}$, where ω is the frequency of the modulation of amplitude ϵ and duration τ.

The Bloch states Ψ^{α}_q of band index α and quasi-momentum q are the eigenstate of H_0,

$$\Psi^{\alpha}_q(x) = \frac{1}{\sqrt{Nd}}\sum_G C^{\alpha}_{q+G}\; e^{i(q+G)x}, \tag{2.56}$$

$$H_0\Psi^{\alpha}_q(x) = E^n_q\Psi^{\alpha}_q(x). \tag{2.57}$$

We define the transition matrix element $T^{\alpha'\alpha}_{q'q}$

$$\begin{aligned} T^{\alpha'\alpha}_{q'q} &= \int_0^{Nd} dx \Psi^{*\alpha'}_{q'}(x) V(x) \Psi^{\alpha}_{q}(x) \\ &= \sum_{n=0}^{N-1} \int_{nd}^{d+nd} dx \Psi^{*\alpha'}_{q'}(x) V(x) \Psi^{\alpha}_{q}(x). \end{aligned} \tag{2.58}$$

Using the same trick of changing variables $x' \equiv x - nd$ as in eq. 2.20, the above equation becomes

$$T^{\alpha'\alpha}_{q'q} = \sum_{n=0}^{N-1} \int_0^d dx' \, \Psi^{*\alpha'}_{q'}(x'+nd) \; V(x'+nd) \; \Psi^{\alpha}_{q}(x'+nd).$$

Since the lattice potential is periodic, i.e. $V(x'+nd) = V(x')$, and the Bloch states obey $\Psi^{\alpha}_{q}(x'+nd) = e^{iqnd} \, \Psi^{\alpha}_{q}(x')$,

$$T^{\alpha'\alpha}_{q'q} = \sum_{n=0}^{N-1} e^{ind(q-q')} \int_0^d dx' \Psi^{*\alpha'}_{q'}(x') \; V(x') \; \Psi^{\alpha}_{q}(x').$$

Using the same trick as in eq. 2.21, the geometric series summed over n reduces to a Kronecker delta $\delta_{q'q}$, then

$$T^{\alpha'\alpha}_{q'q} = \delta_{qq'} \sum_{G'G} C^{*\alpha}_{q+G'} \; C^{\alpha}_{q+G} \int_0^d \frac{1}{d} dx' e^{i(G-G')x'} V(x'). \tag{2.59}$$

For $V(x) = V_1 \cos^2(2kx)$, by ignoring the constant offset of $V_1/2$, one can write $V(x) = \frac{V_1}{4}(e^{iG_0x} + e^{-iG_0x})$ where $G_0 = 2k$,

$$\int_0^d \frac{1}{d} dx' e^{i(G-G' \pm G_0)x'} = \delta_{G',G\pm G_0}. \tag{2.60}$$

Dividing by E_R yields the dimensionless transition matrix elements, $T = \widetilde{T} E_R$,

$$\widetilde{T}^{\alpha'\alpha}_{q'q} = \delta_{qq'} \widetilde{V} \sum_{G=G_{min}}^{G_{max}-G_0} \left(C^{*\alpha}_{q+G} \; C^{\alpha}_{q+G+G_0} + C^{*\alpha}_{q+G+G_0} \; C^{\alpha}_{q+G} \right), \tag{2.61}$$

where $\widetilde{V} = V_1/(4E_R) = -s_1/4$ and $\Psi_q^\alpha(x) = \sum_G C_{q+G}^\alpha e^{i(q+G)x}$ is the Bloch solution for the un-perturbed Hamiltonian in eq. 2.57. Note that the sum is truncated at $G_{max} - G_0$. For a $2M + 1$ band model, the range of G is $G \in [-MG_0, -(M-1)G_0, ..., -G_0, 0, G_0, ..., MG_0]$ where $G_{min} = -MG_0$ and $G_{max} = MG_0$. In order not to exceed the matrix dimension when summing over G with the extra G_0 shift due to the coupling potential $V(x)$, the upper limit of the summation is modified accordingly to $G_{max} - G_0$. For a 5-band model, $G_{min} = -2G_0$ and $G_{max} = 2G_0$. The sum then runs from $-2G_0 \leqslant G \leqslant G_0$. The $\delta_{q,q'}$ indicate that sinusoidally modulating of the lattice depth allows transitions only between states having the same quasi-momentum, as shown in Fig 2.9.

Consider modulating only the green lattice, for atoms loaded into the bichromatic lattice, i.e.,

$$H_0 = \frac{p^2}{2m} + V_1 \cos^2 kx + V_2 \cos^2\left(2kx + \frac{\phi}{2}\right) \tag{2.62}$$

$$H' = \epsilon V_2 \cos^2\left(2kx + \frac{\phi}{2}\right)\cos(\omega t). \tag{2.63}$$

Analogous to the previous case, we ignore the offset and write $V(x) = \frac{V_2}{4}(e^{i2G_0x+i\phi} + e^{-i2G_0x-i\phi})$ when computing the dimensionless transition matrix element. Then,

$$\widetilde{T}_{q'q}^{\alpha'\alpha} = \delta_{qq'}\widetilde{V}\sum_{G_{min}}^{G_{max}-2G_0}\left(C^{*\alpha}_{q+G}\, C^{\alpha}_{q+G+2G_0}e^{-i\phi} + C^{*\alpha}_{q+G+2G_0}\, C^{\alpha}_{q+G}e^{i\phi}\right). \tag{2.64}$$

Here $\widetilde{V} = V_2/4E_R$ and $\Psi_q^\alpha(x) = \sum_G C_{q+G}^\alpha e^{i(q+G)x}$ is the eigenvector of eq. 2.62. In order not to exceed the matrix dimension when summing over G with the extra $2G_0$ shift due to the coupling potential $V(x)$, the upper limit of the summation is modified accordingly to $G_{max} - 2G_0$.

We show in Fig 2.10 the transition matrix element squared for transitions from the ground band to all higher bands, when modulating a single color lattice. Apart

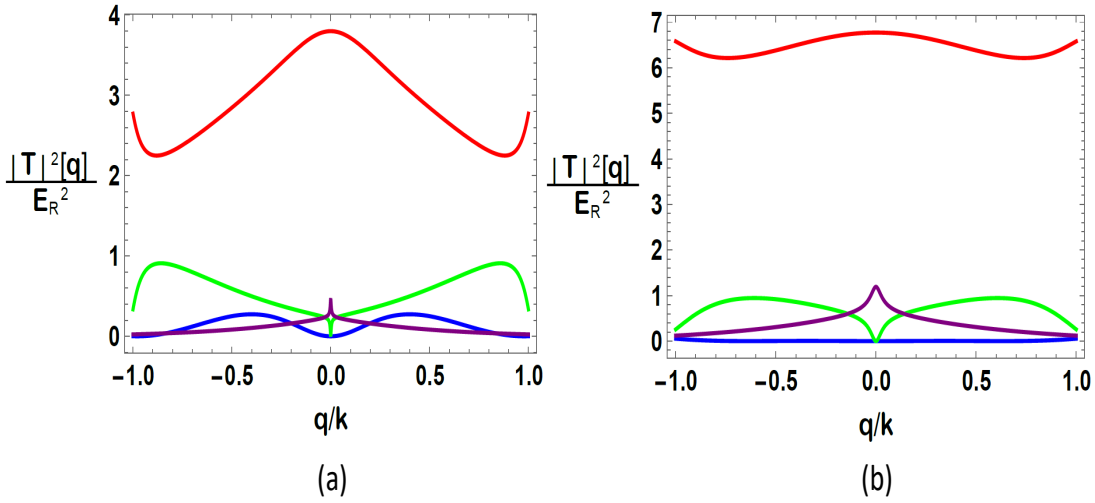

FIGURE 2.10: Interband transition matrix element squared for modulating a single color lattice of (a) $s_1 = 10$ and (b) $s_1 = 20$. Colors denote transition between different bands. Blue: 1→2, Red: 1→3, Green: 1→4, Purple: 1→5.

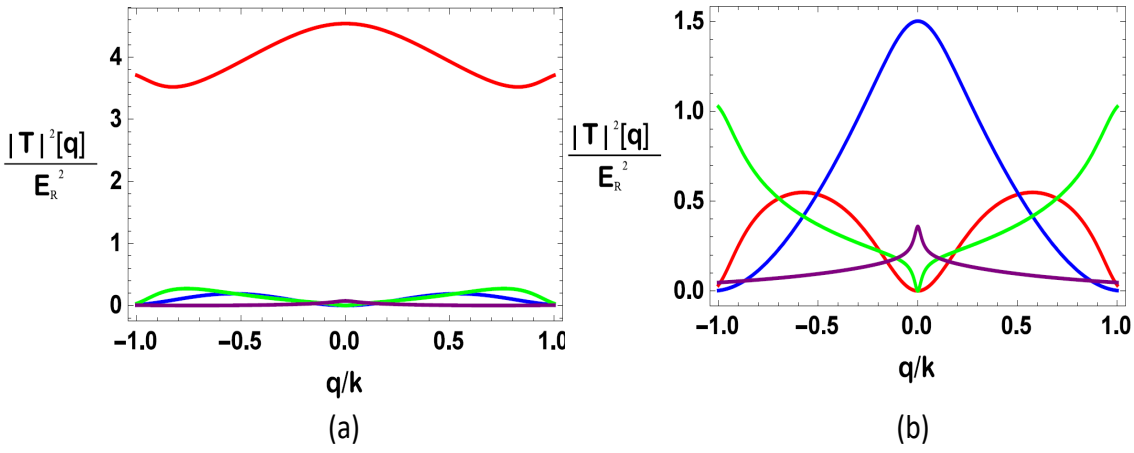

FIGURE 2.11: Interband transition matrix element squared for modulating the fundamental(s_1) component of a bichromatic lattice of $s_1 = 8$, $s_2 = 8$, (a) $\phi = \pi$ and (b) $\phi = 0$. Colors denote transition between different bands. Blue: 1→2, Red: 1→3, Green: 1→4 Purple: 1→5

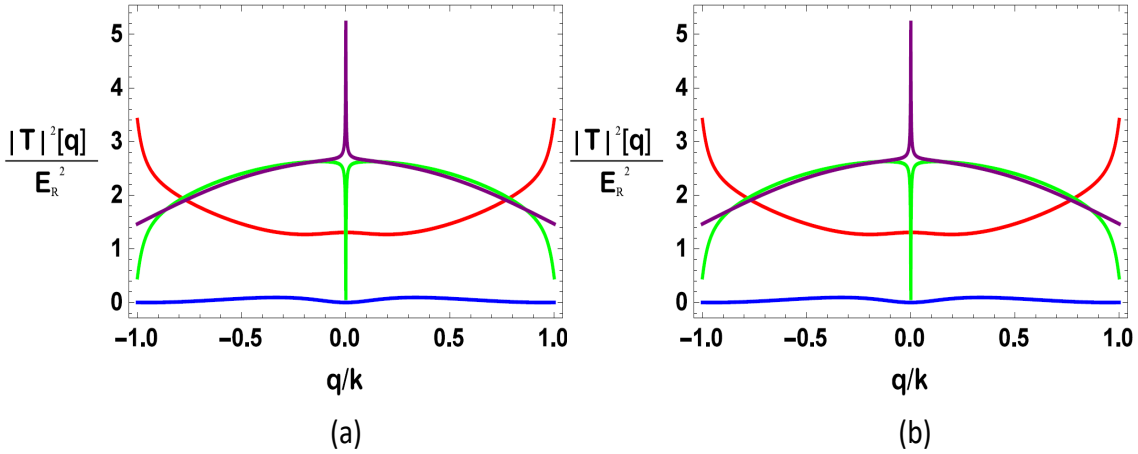

FIGURE 2.12: Interband transition matrix element squared for modulating the secondary(s_2) component of a bichromatic lattice of $s_1 = 8$, $s_2 = 8$, (a) $\phi = \pi$ and (b) $\phi = 0$. Colors denote transition between different bands. Blue: 1→2, Red: 1→3, Green: 1→4 Purple: 1→5

from noticing the quasi-momentum dependence, also note that both Fig 2.10(a) and Fig 2.10(b) show enhanced $1 \rightarrow 3$ transitions compared to all other transitions.

Fig 2.11 shows the interband transition element squared between the ground band and all higher bands when modulating the fundamental(s_1) component of a bichromatic lattice of $s_1 = 8$, $s_2 = 8$, for relative phase of $\phi = 0$ and π. When $\phi = 0$, which corresponds to a periodic double well lattice, transitions for $1 \rightarrow 2$ and $1 \rightarrow 4$ are greatly enhanced. Fig 2.12 shows the result when modulating the secondary(s_2) component of a bichromatic lattice of $s_1 = 8$, $s_2 = 8$, for relative phase of $\phi = 0$ and π. The results for the two phases are identical. Comparing Fig 2.11 to Fig 2.12, one finds enhancement in particular for $1 \rightarrow 4$ or $1 \rightarrow 5$ transitions by modulating the secondary lattice.

The lattice modulation modifies the band occupation probability. We simulate a band map after lattice modulation by including the parametric transition probability $P^{\alpha',\alpha}(\epsilon, \omega, \tau, \tilde{q})$, in the momentum distribution $\widetilde{W}(\tilde{p})$ in eq. 2.49. For a selected ω to

induce transitions from state α to α', the momentum distribution of state α' is

$$\widetilde{W}^{\alpha'}(\widetilde{p}) = \sum_G |C_G^{\alpha'}(\widetilde{p}-\widetilde{G})|^2 P^{\alpha',\alpha}(\epsilon,\omega,\tau,\widetilde{p}-\widetilde{G}) \\ \frac{\left[\widetilde{\mu}-\widetilde{E}^{\alpha}\left(\widetilde{p}-\widetilde{G}\right)\right]^2}{\widetilde{E_F}^2}\Theta\left[\widetilde{\mu}-\widetilde{E}^{\alpha}(\widetilde{p}-\widetilde{G})\right]\Theta\left[1-(\widetilde{p}-\widetilde{G})^2\right] \tag{2.65}$$

The remaining momentum distribution in state α is

$$\widetilde{W}^{\alpha}(\widetilde{p}) = \sum_G |C_G^{\alpha}(\widetilde{p}-\widetilde{G})|^2 \left[1-P^{\alpha',\alpha}(\epsilon,\omega,\tau,\widetilde{p}-\widetilde{G})\right] \\ \frac{\left[\widetilde{\mu}-\widetilde{E}^{\alpha}\left(\widetilde{p}-\widetilde{G}\right)\right]^2}{\widetilde{E_F}^2}\Theta\left[\widetilde{\mu}-\widetilde{E}^{\alpha}(\widetilde{p}-\widetilde{G})\right]\Theta\left[1-(\widetilde{p}-\widetilde{G})^2\right] \tag{2.66}$$

Summing over the momentum distributions of all bands, one obtains

$$\widetilde{W}(\widetilde{p}) = \widetilde{W}^{\alpha'}(\widetilde{p}) + \widetilde{W}^{\alpha}(\widetilde{p}) + \sum_{\beta\neq\alpha,\alpha'} \widetilde{W}^{\beta}(\widetilde{p})\,. \tag{2.67}$$

We show in Fig 2.13 the simulated band map for modulating the one color lattice of $s_1 = 8$ with modulation amplitude $\epsilon = 13\%$ and $\tau = 1.3$ ms at 110 kHz for a chemical potential of $\mu = 3\,E_R$. For this chemical potential, only the ground band is initially filled before the modulation. The modulation frequency corresponds to a $1 \rightarrow 3$ transition at normalized quasi-momentum $\tilde{q} = 0.6$. Details of lattice modulation experiments are presented in Sec 3.8.

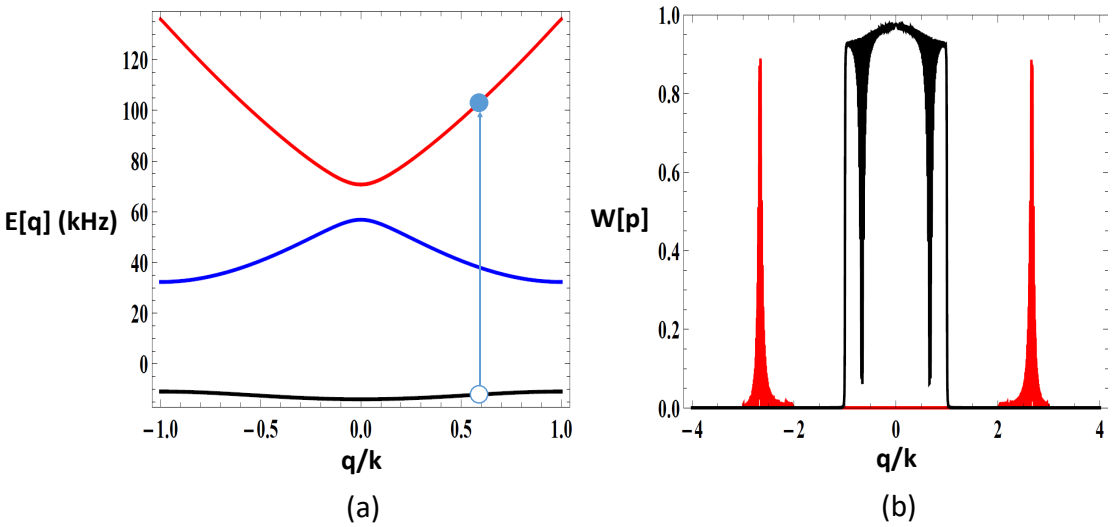

FIGURE 2.13: Band map simulation after lattice modulation of a lattice depth of $8E_R$ with a 13% modulation amplitude for 1.3 ms at 110 kHz. (a) Band structure of a $8E_R$ lattice in units of kHz. The driving frequency 110 kHz corresponds to a $1 \rightarrow 3$ transition at $\tilde{q} = 0.6$. (b) The simulated band map result using eq. 2.54, showing depletion of the initial population in the ground band (black) and transfer to the second excited band (red).

3

Experimental Methods

In this chapter, I begin with the basic experimental methods for generating a degenerate Fermi gas sample in Sec 3.1. The new bichromatic optical lattice with tunable relative phase and repulsive end caps is presented in Sec 3.2 and 3.3. The lattice alignment procedure and the lattice loading procedure are presented in Sec 3.4 and 3.5. The lattice calibration using Kapitza-Dirac scattering is presented in Sec 3.6. The band mapping method for the bichromatic lattice is presented in Sec 3.7. Lastly I describe the trap frequency measurements, employing parametric resonance in Sec 3.8.

3.1 Standard Cooling and Trapping

In brief, the atom sample preparation involves an atomic source and techniques of cooling and trapping. The solid ^{6}Li is stored in an oven with a long hollow wick, which directs an atomic beam towards the main vacuum chamber. The oven is heated up to about 400°C to vaporize the solid, generating a hot gas traveling along the nozzle, through a Zeeman slower, which decelerates the atoms from about $1\,km/s$ to $30\,m/s$, slow enough to be trapped in a magneto-optical-trap (MOT). The MOT

is composed of a pair of anti-Helmholtz coils and three orthogonal retroreflected laser beams, which are red-detuned with respect to D2 line of ^{6}Li, and is located at the center of the chamber. The atoms enter the MOT region and are cooled to the Doppler limit of 140 μK. The repump beams, close to resonance with the D2 line, are turned off so atoms are pumped into the $^2S_{1/2}$ $F = 1/2$ ground states. All MOT beams and the quadrupole fields are turned off at the end, and approximately two million atoms are loaded into a far off-resonance CO_2 laser dipole trap (FORT), which is superposed on top of the MOT.

Then we turn on the bias magnetic field produced by a pair of high field magnets to roughly 8 G to split the degenerate ^{6}Li hyperfine states. We apply an rf pulse corresponding to the energy difference between the lowest two states $|1\rangle$ and $|2\rangle$ to produce a population balanced two state mixture. The bias magnetic field is then increased to 834 G near a $|1\rangle$-$|2\rangle$ Feshbach resonance, where the enhanced collision rate causes atoms that gain energy during the collision to escape the trap more efficiently, while leaving lower energy atoms trapped. We refer to this stage as free evaporation. At the end of this stage, we are left with 450 thousand atoms per spin state at 50 μK.

The atoms are further cooled down after evaporation by lowering the FORT, which we refer to as forced evaporative cooling. At the end of forced evaporative cooling, the atomic sample reaches the temperature of about 10 to 100 nK. For more details about general degenerate atom sample preparation, please refer to previous theses by our group [62]. After evaporative cooling, the gas is ready to load into the bichromatic optical lattice. The procedure is presented in Sec 3.4.

3.2 Bichromatic Lattice Setup

The bichromatic lattice system shown in Fig 3.1 and Fig. 3.2 is comprised of two optical lattices, a fundamental lattice of $\lambda_1 = 1064$ nm and a secondary lattice of

$\lambda_2 = 532$ nm. The 1064 nm infrared beam is generated from a IPG 30W fiber laser (model: YLR-30-1064-LP-SF) and has a linewidth smaller than 100 kHz. We take 5W out of this beam to send into a frequency doubling cavity (Toptica SHG pro) with a light convertion efficiency of about 40% to generate a 2W 532 nm beam at exactly double the frequency of the pump beam. Each of the beams passes through a similar set of optics, as shown in Fig 3.1. The beams first go through a pair of phase-locked high power AOMs made of TeO_2. We send about 3W of each beam in to the AOMs, which have 80% efficiency or higher for the first order diffracted beam. The phase-locked module modulates the 1064 nm beam at 80 MHz and the 532 nm beam at 160 MHz, which preserves the two-to-one ratio of their frequencies. Then each beam goes through a spatial filtering setup to clean up the profile before coupling into a high power polarization maintaining optical fiber (Oz optics). For 1 W output of the fiber, the coupling efficiency is around 60%.

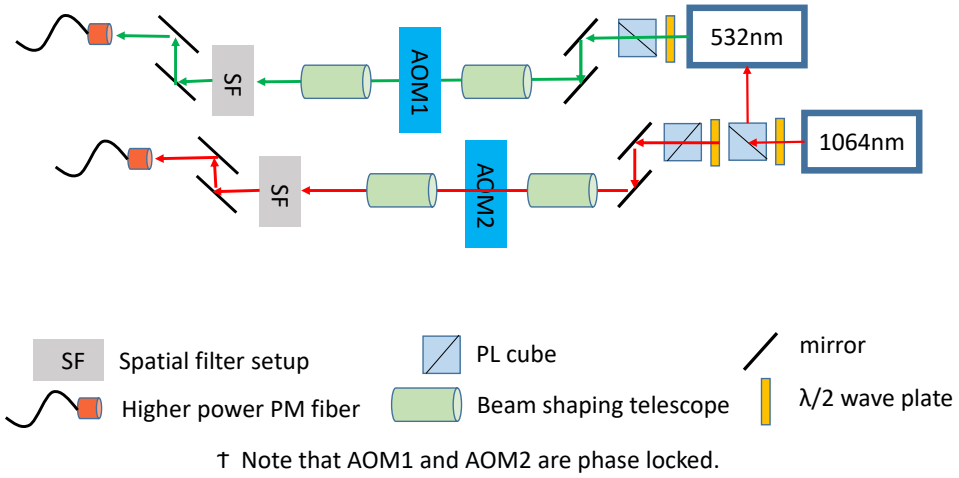

FIGURE 3.1: Setup for generating bichromatic lattice beams. The 532 nm beam is generated by pumping a frequency doubling cavity with a 1064 nm beam. The beam goes through a phase-locked AOM, some shaping optics, and spatial filtering setup before coupling into a polarization maintaining optical fiber.

The lattice setup is shown in Fig 3.2. The outputs of the two fibers are each

mounted on an ultrastable mirror mount. The two beams go through individual sets of mirrors and focusing lenses, and then are combined on a common dichroic beam splitter before going through the vacuum chamber. Note that the two beams are both vertically polarized, i.e., pointing into the paper in Fig 3.2, to achieve maximum interference intensity, since the lattices are constructed by intersecting two beams at a $\theta = 91^\circ$ angle as shown in Fig 2.2. All optics are located on top of a 3-axis translational stage. A window with antireflection coating is inserted after the output of each fiber to pick off a small portion of the beam, which is then focused on to a photodiode for control and stabilizing the lattice beam intensity using a servo. The individual sets of mirrors allows us to easily align the two beams. The individual focusing lenses are adjusted such that the two beams roughly focus in the same plane, with the measured $1/e$ field radius at the focus being $110\,\mu$m for 1064 nm beam, and $90\,\mu$m for 532 nm beam. The Rayleigh lengths for the beams are roughly 3 cm and 4 cm respectively.

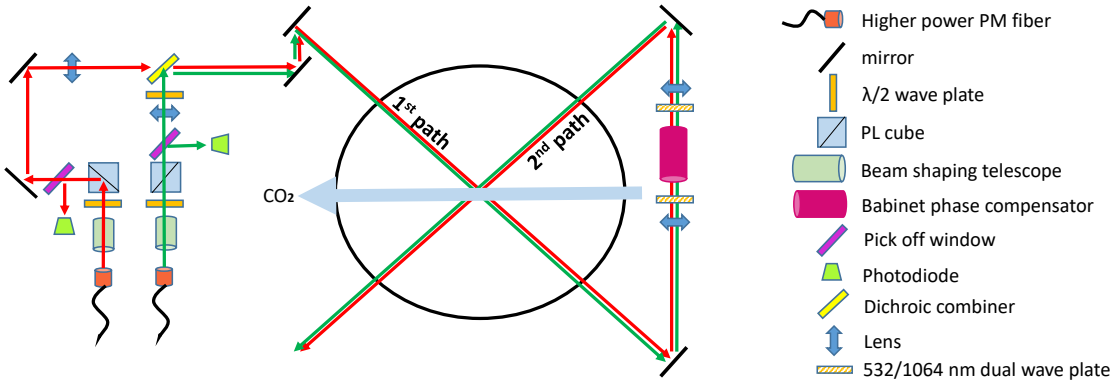

FIGURE 3.2: Bichromatic lattice setup. The $\lambda_1 = 1064$ nm and $\lambda_2 = 532$ nm beams are combined on a dichroic beam splitter before co-propagating through the chamber. A Babinet compensator is inserted in the second path to adjust the relative phase between the two color lattices.

The two beams co-propagate after the combining dichroic beam splitter, and go

through the atomic cloud twice. The beams enter the chamber the first time and focus near the atom cloud. We refer to this as the first path. After passing through the chamber, they are collimated with a common lens and go through a Babinet phase compensator before passing through a common focusing lens. The beams enter the chamber again, which we refer to as the second path, and focus around the atoms. The interference between the two paths creates a standing wave pattern along the CO_2 laser beam. The lattice beam size measurements around the focal point of the first and second path are shown in Fig 3.3.

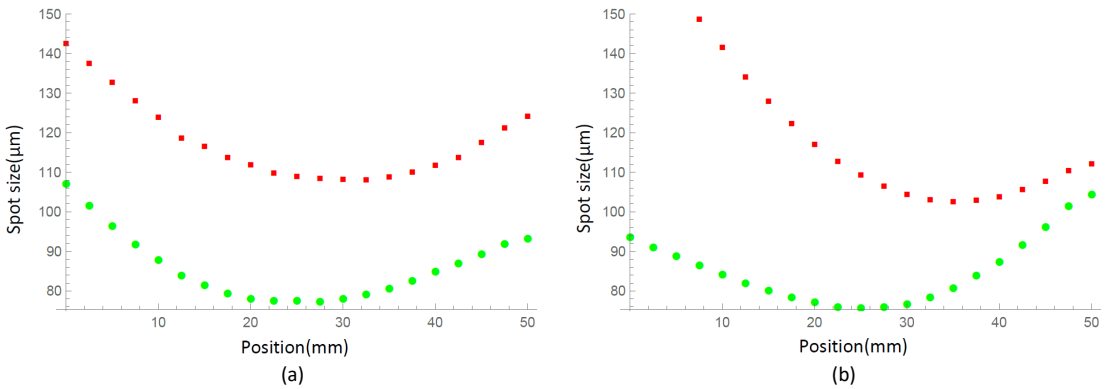

FIGURE 3.3: Lattice beam size measurements near the focal plane of (a) the first path, and (b) the second path. The $\lambda_1 = 1064$ nm beam is labeled red, and the $\lambda_2 = 532$ nm beam is labeled green. The two beams roughly focus at the same place, and each has a size of roughly 100 μm.

By construction, the relative phase between the intensity patterns of the two color beams is locked due to traveling through the same optical path, although the combined lattice may drift slowly in space. With the Babinet phase compensator, one can change the relative phase of the intensity patterns, which results in double well potentials with tunable symmetry. In order to maximize the difference in phase retardation using the Babinet compensator, we align the 1064 nm and the 532 nm beam polarization each to the fast and slow axis of the birefringent crystal quartz. Note that the 532/1064 nm dual-wavelength waveplate is made of two quartz waveplates combined with their optical axes orthogonal to one another. The dual-

wavelength waveplates placed before and after the Babinet compensator in Fig 3.2 rotate the polarization of the 532 nm beam by $\lambda/2$ while producing a retardation of λ for the 1064 nm light, which has no effect.

3.3 End Caps

As mentioned earlier, our composite trap is formed by a bichromatic lattice superposed on a CO_2 laser trap. We increase the chemical potential by increasing the radial confinement of the CO_2 laser trap. As described in Sec 2.3, the probability of occupying higher bands is enhanced by increasing the chemical potential. Since atoms in higher bands have larger tunneling rate, they will tunnel out of the region where the maximum lattice depth is located, therefore causing a non-uniform lattice population. We employ end caps constructed by two repulsive $\lambda = 532$ nm sheets, which are focused on the CO_2 laser trap and placed on both ends of the bichromatic lattice, as shown in Fig 3.5. These end caps prevent tunneling by providing extra confinement and preserve the atom number per unit area.

The end caps are particularly useful when investigating properties of the secondary $\lambda_2 = 532$ nm lattice alone. Atoms are repelled from the optical potential of a blue-detuned beam. By first loading atoms into an 1064 nm dipole trap and turning on two green end caps, the atoms are confined in a region between the two caps, even when the 1064 nm dipole trap is turned off. With the radial confinement of the soft CO_2 dipole trap, we can load the atoms into the green lattice by confining the atoms within the region inside the caps along the CO_2 laser beam. The power we use for each green sheet is nominally 850 mW.

The end caps contain two sheets, each has a waist of 10 μm-by-100 μm at the focal plane as shown in Fig 3.4. They are focused around the center of the CO_2 dipole trap with adjustable separation in between, as shown in Fig 3.5. To generate the end caps, the 532 nm light generated from a Verdi V-10 (Coherent) is split and coupled into

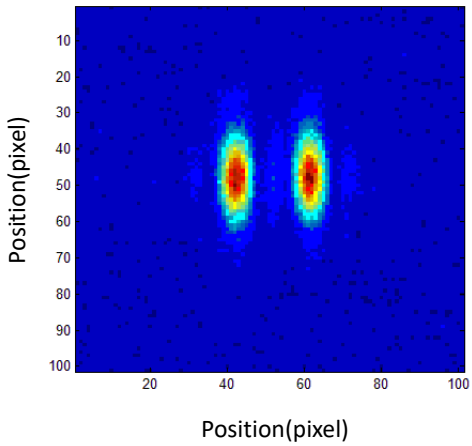

FIGURE 3.4: The profile of end caps taken by a CCD camera. The Gaussian waist size of each sheet is 10 μm-by-100 μm.

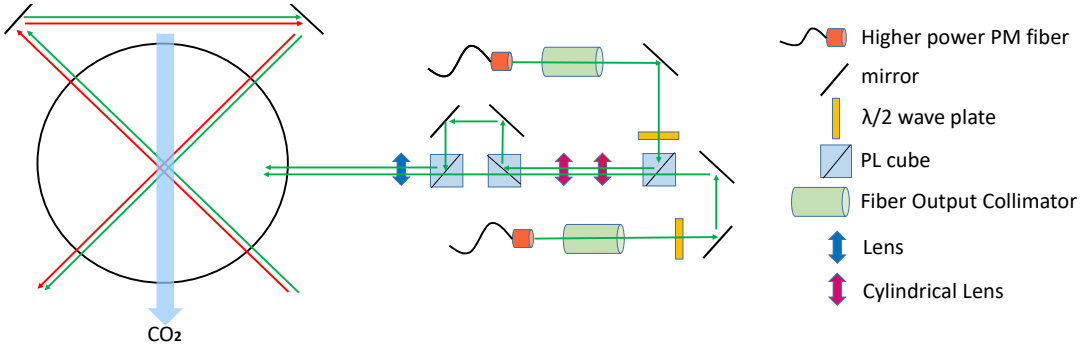

FIGURE 3.5: Cap beam optics. Two 1-inch cross-polarized green beams are combined before going through a common final focusing lens. The relative position between the two sheets can be adjusted by moving the two mirrors near the two cubes. End caps are focused on the CO_2 laser trap and placed on two ends of the optical lattice.

two high power PM fibers (Oz optics). The beam at each fiber output is expanded to 1 inch before going though a pair of cylindrical lenses to modify its aspect ratio to the desired dimension of the caps at the focal plane. The two beams are set to be cross polarized before being combined in order to prevent interference, and go through a common focusing lens. By going into the lens with slightly different incident angles, we create two parallel sheets around the focus of the lens. The relative position between the two sheets can be adjusted using the two mirrors near the two cubes.

3.4 Lattice Alignment

The lattice beam alignment procedure is as follows. First make sure the 1064 nm and 532 nm beams are on top of each other as closely as possible. This is very critical because the repulsive 532 nm trap cancels the attractive 1064 nm trap to some extent. Thus, any misalignment between the two beams leads to a nonuniform potential and therefore a very nonuniform atom distribution. We check the overlap at two spatial points with CCD cameras, to see that the center of two beams are aligned within the resolution of the camera, which is around 5 μm. The setup has sufficient stability that the two color alignment stays nominally the same throughout the day.

Since the two beams are propagating together after being combined on the dichroic beam splitter, it is to our convenience to align the beams on the atoms using only the red-detuned 1064 nm beam, since the blue-detuned 532 nm light does not trap atoms. Because the 1064 nm beam has a few cm long Rayleigh length, it is unlikely to miss its focal point of the CO_2 dipole trap along the propagation direction.

We measure the distances very carefully when initially setting up the beams. Apart from the first 1064 nm beam propagation direction $\hat{a}$ as noted in Fig 3.6, there are two other directions, one vertical denoted as $\hat{b}$, and the other along the the CO_2 laser beam propagation direction denoted as $\hat{c}$. We have two cameras in both the horizontal and the vertical direction to help us to do the alignment.

To begin with, we record the center position of the CO_2 laser dipole trap on both cameras. We ramp up the 1064 nm lattice beam adiabatically[1], with the second path blocked, immediately after the lowest point of forced evaporative cooling process of

[1] In order to load the atoms into the ground state of the optical lattice, the ramping process should be adiabatic. We use 200 ms for the exponential ramp time, and verified that cloud radii after ramping up and down of the lattice remains the same as that before the ramp, indicating no increase in energy.

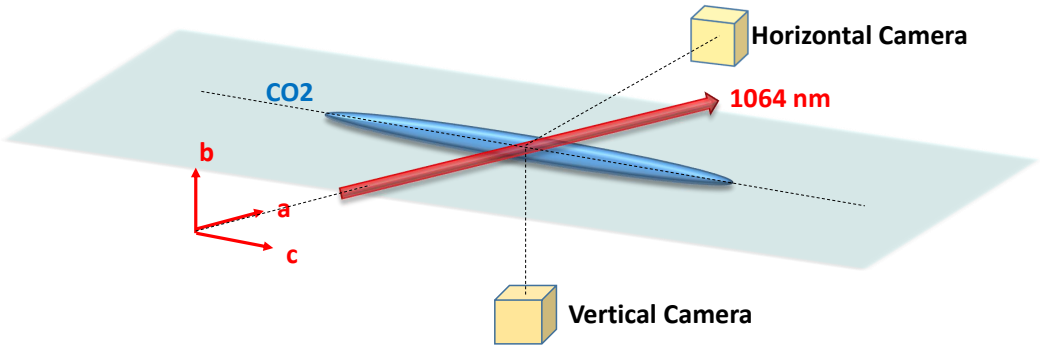

FIGURE 3.6: Lattice beam alignment using horizontal and vertical cameras. This figure illustrates the first 1064 nm lattice beam direction with respect to the CO_2 laser dipole trap, and the locations of the two cameras.

the CO_2 laser trap. Only when the first 1064 nm path is placed close enough ($\lesssim$200 μm) to the CO_2 laser trap will the atoms feel the extra confinement potential and shift the cloud position towards the global minimum of the combined trap. We place the first path vertically and horizontally such that the center position of the cloud remains the same as that of the cloud in the CO_2 trap alone, as shown in Fig 3.7(a). Then we move the translation stage along the propagation direction of the first 1064 nm path by several centimeter in and out, every time re-adjusting the other two directions so that the beams still align reasonably well with the CO_2 laser trap. Within a few cm range, there is not much difference in the loading. Thus, we conclude the focus is soft in this direction and further alignment is not needed. For the second 1064 nm lattice beam path, do the same thing by making the cloud center position the same as the cloud in the CO_2 laser trap alone, but this time we turn off the CO_2 for about 3 ms to allow the cloud to expand along the first lattice beam direction, as shown in Fig 3.7(b). Without turning off the CO_2 laser trap, the cloud will always be confined in the same radial region because radial confinement is dominated by the CO_2 laser dipole trap and one can not judge how well the second

lattice beam is aligned with the first one. Now that we have the first 1064 nm lattice beam and the first+second 1064 nm lattice beams all with the same center position as the CO_2 laser trap center, as shown in Fig 3.7(c), the alignment procedure is completed.[2]

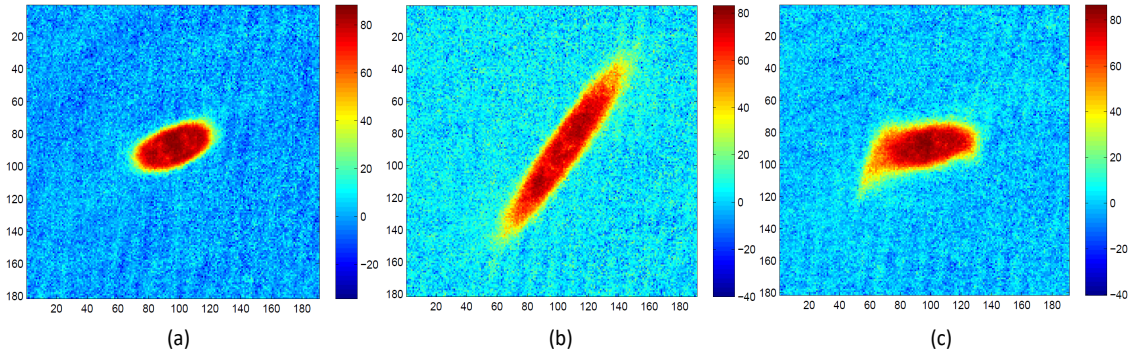

FIGURE 3.7: These three pictures illustrate how we align the two intersecting 1064 nm lattice beams. (a) Showing how the cloud looks when the first path cross the center of the CO_2 laser dipole trap. (b) Allowing atoms to expand along axial direction of the first infrared lattice beam dipole trap. (c) We complete the alignment procedure by aligning the second path to the same center position.

Since our lattice is formed by two intersecting beams rather than by retroreflected beams, it is important to measure the angle between these two beams in order to know two important scales, the lattice spacing d and the corresponding recoil energy E_R, for our lattice system. The first lattice beam direction can be found by turning off the CO_2 laser trap. Then the cloud would expand along the 1064 nm dipole trap as shown in Fig 3.8(b). For convenience, we rotate the camera such that the CO_2 trap axial direction lies nominally parallel to the horizontal axis of the camera CCD.

The angle between the first infrared beam and the CO_2 laser axial direction, α,

[2] For the application when caps are needed, the sheet beams are aligned to the CO_2 and placed at the edges of the atomic distribution of the infrared dipole trap or infrared lattice, depending on whichever one is needed.

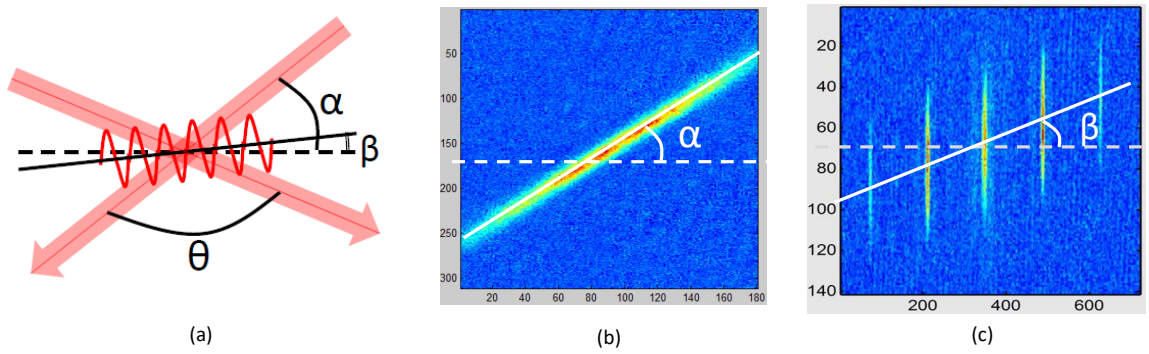

FIGURE 3.8: Measuring the intersection angle between the two lattice beams. The horizontal dashed line denotes the axial CO_2 laser dipole trap direction. (a) Angle between two lattice beams is $\theta = \pi - 2(\alpha - \beta) = 91°$. Effective lattice spacing $d = 0.746\,\mu$m and recoil energy of the 1064 nm lattice is $E_R = h \times 14.9$ kHz. (b) Angle between the first 1064 nm path and the CO_2 is $\alpha = 48.99°$. (c) Angle between the 1064 nm lattice and the CO_2 is $\beta = 4.48°$.

can be measured. Pulsing the lattice on the atoms imprints net momentum transfer along the lattice direction. Therefore by looking at the Kapitza-Dirac scattering pattern after the pulse and fitting the centers of each higher order diffraction to draw a straight line connecting those centers, we can find the direction of the lattice beam and extract its angle β, as shown in Fig 3.8(c). Notice that due to the limitation of the chamber geometry, the lattice is rotated slightly from the axial direction of the CO_2 laser beam. With α and β, the angle between the two intersecting beams is $\theta = \pi - 2(\alpha - \beta) = 91°$. Thus, our optical lattice as discussed in eq. 2.8, has a lattice spacing of $d = \frac{\lambda}{2\sin\left(\frac{\theta}{2}\right)} = 0.746\,\mu$m, which is smaller than the resolution of our imaging setup (3 μm). The recoil energy of the infrared lattice is $E_R = \frac{h^2 \sin^2\left(\frac{\theta}{2}\right)}{2m\lambda^2} = h \times 14.9$ kHz. The lattice depth is calibrated by Kapitza-Dirac scattering, presented in detail in Sec 3.6.

3.5 Lattice Loading

We start loading atoms into the lattices immediately after the CO_2 has reached the lowest point at the end of the forced evaporative cooling process. For example, consider the loading into a bichromatic lattice. The 1064 nm lattice ramps up adiabatically for 200 ms. Simultaneously the CO_2 laser trap is raised to a desired final shallow trap depth. The atoms sit inside the composite trap of full 1064 nm lattice and CO_2 for about 200 ms before ramping up the 532 nm lattice in 200 ms. We wait for 300 ms for the atoms to reach thermal equilibrium in the overall lattice before any manipulation.

Physical manipulation includes trap modulation for interband transitions, applying a radio-frequency pulse or resonant optical pulse to remove one spin state, or lowering the lattice to map out the band population. After the physical manipulation, we take absorption image in situ or with a time-of-flight. The timing is schematically shown in Fig 3.9.

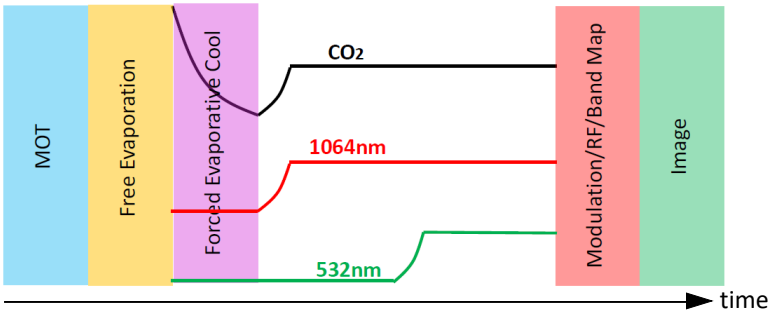

FIGURE 3.9: Loading atoms into a bichromatic lattice. Load into the 1064 nm lattice, wait to reach equilibrium, then turn on the 532 nm lattice, and wait to reach thermal equilibrium before physical manipulation.

To obtain a higher Fermi energy when needed, the caps can constrain atoms inside the superlattice region under stronger radial compression from the CO_2 laser trap. The time ordering sequence is complicated, as shown in Fig 3.10. First the

1064 nm lattice, then the end caps, and finally the CO_2 laser trap are raised up before the green lattice is turned on. Notice that the end caps have to be turned on before the CO_2 laser trap is raised to a higher trap depth to avoid atom loss.

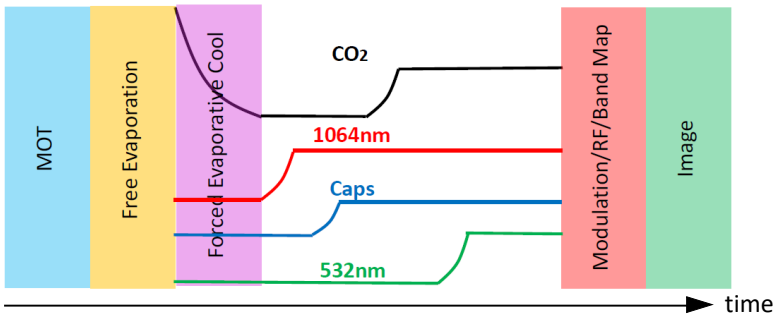

FIGURE 3.10: Loading atoms into a bichromatic lattice with higher Fermi energy from the CO_2 laser trap. We turn on the 1064 nm lattice, then the caps before the CO_2 laser trap goes up, and finally ramp up the 532 nm lattice.

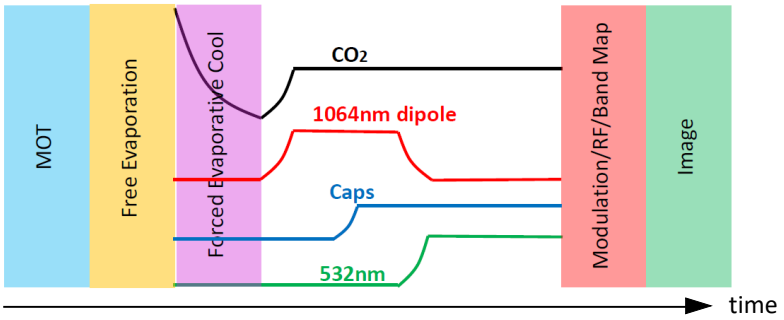

FIGURE 3.11: Loading atoms into a repulsive 532 nm lattice. We first load into the 1064 nm dipole trap before raising the caps. Then we simultaneously turn off the 1064 nm dipole trap and finally turn on the 532 nm lattice.

When investigating the repulsive 532 nm lattice alone, the use of the end caps is essential. The loading time scale is nominally the same. Atoms are first loaded into the 1064 nm dipole trap before raising up the caps. Then the 1064 nm dipole trap is turned off and the 532 nm lattice is turned on simultaneously as shown in Fig 3.11

3.6 Lattice Depth Calibration

We use the diffraction of the atoms from the standing wave lattice to measure the depth and the spacing of the periodic potentials. This technique, called Kapitza-Dirac scattering [63], is commonly used when calibrating the depth of optical lattices. It is very similar to the classical diffraction of light off a grating. However, in this case, it is the atoms scatter off from the light grating formed by the spatially periodic intensity of the light.

Scattering off the standing wave imprints discrete momentum transfer onto the atoms. We obtain a molecular BEC as described below after forced evaporative cooling using the CO_2 laser dipole trap. By pulsing the optical lattice on the BEC, the periodicity of the lattice potential and the lattice depth can be determined from the distances between the diffraction orders and the relative number of atoms transferred into different orders for different pulse times.

Consider a simplified condition, where the atomic motion during the interaction time can be ignored (called the Raman-Nath approximation). For the above condition to be valid, a short interaction time t much smaller than the inverse recoil frequency ($t \ll 1/\,\omega_{rec}$) is required. Then the kinetic energy term in the Hamiltonian can be neglected [64].

$$H = V_0 \sin^2 kz. \tag{3.1}$$

Assume the initial state is a BEC of momentum q, i.e., $\Psi(0) = e^{iqz}$. For a time-independent Hamiltonian, the state at time t is

$$\begin{aligned} \Psi(t) &= e^{\frac{-iHt}{\hbar}}\Psi(0) \\ &= e^{-\frac{i}{2\hbar}V_0 t} e^{\frac{i}{2\hbar}V_0 t \cos 2kz}\Psi(0). \end{aligned} \tag{3.2}$$

By using the identity

$$e^{i\alpha\cos\beta} = \sum_{n=-\infty}^{\infty} i^n J_n(\alpha) e^{in\beta}, \tag{3.3}$$

where $J_n(\alpha)$ is the n-th order Bessel function of the first kind, the state at time t can be written as:

$$\Psi(t) = e^{-\frac{i}{2\hbar}V_0 t} \sum_{n=-\infty}^{\infty} i^n J_n\left(\frac{V_0 t}{2\hbar}\right) e^{i(q+2nk)x}. \tag{3.4}$$

The atoms are transferred from momentum state q to $q+2nk$ with a time dependent probability $P_n(t) = J_n^2(\frac{V_0 t}{2\hbar})$, where the argument of $J_n(\frac{V_0 t}{2\hbar})$ is proportional to the pulse area $\frac{V_0 t}{2\hbar}$. In order to observe sufficient population transfer to higher momentum states with such short pulse duration, a high intensity lattice is needed.

To observe the diffraction pattern, we produce a molecular BEC by performing a two-stage forced evaporative cooling of a two-component Fermi gas first at the broad Feshbach resonance (832 G). Then we continue to cool while sweeping the bias magnetic field to the BEC side, at around 720 G. A molecular BEC is shown in Fig 3.12(a). By turning off the CO_2 laser dipole trap, the cloud expands very quickly in the vertical direction while it shrinks significantly along the axial direction of the original dipole trap, which is also the lattice direction. The shrinkage arises from the remaining magnetic confinement.[3] The fast expansion in the vertical direction due to the magnetic field curvature prevents us from efficiently transferring atoms into different diffraction orders. Therefore, it is important to use the maximum lattice depth that we have in order to see different scattering orders using short pulse durations.

We pulse a 1 W 1064 nm optical lattice on the BEC when its axial size (along the CO_2 laser trap direction) shrinks to about 50 μm and radial size of 30 μm so that it

[3] Refer to Fig 3.6 for definitions of directions.

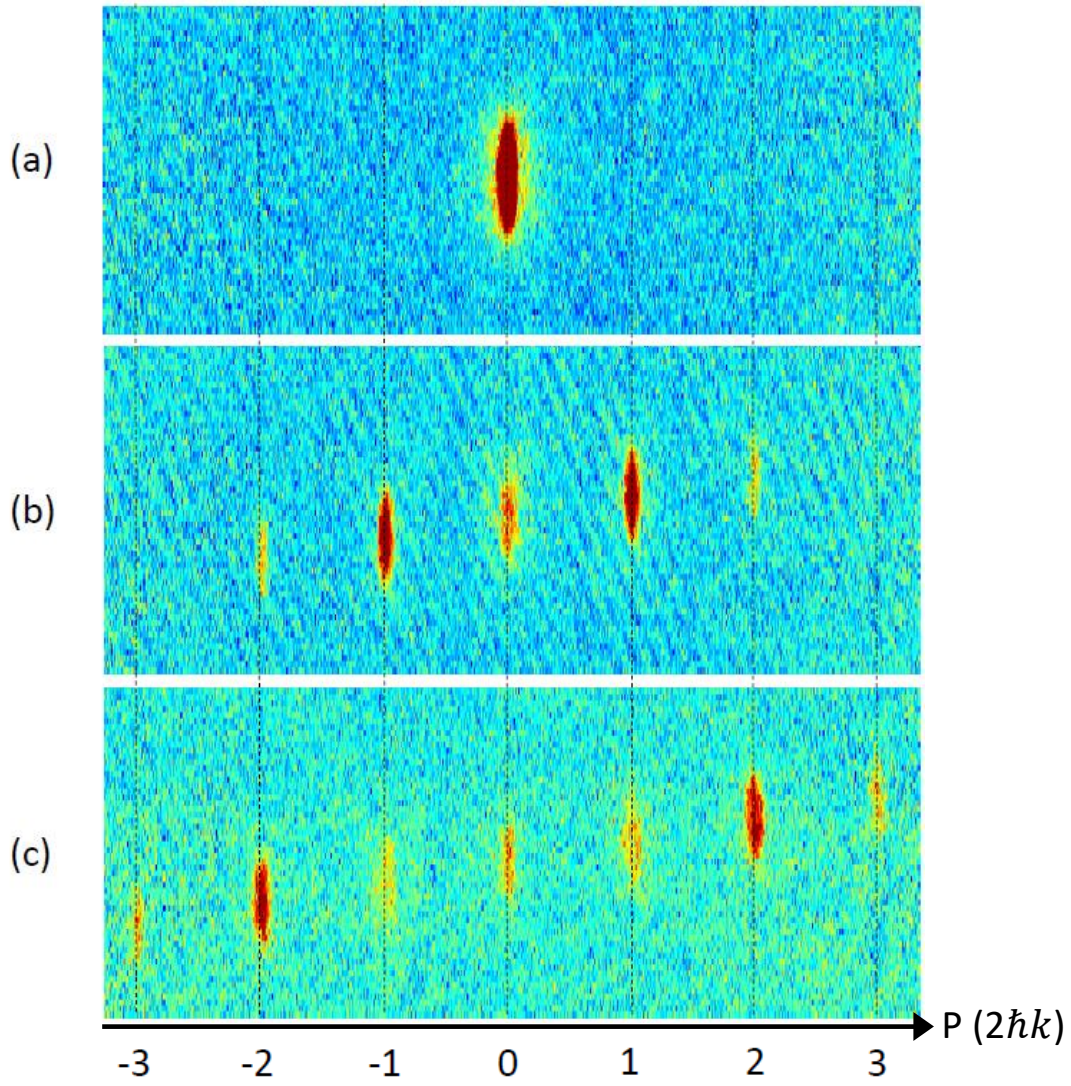

FIGURE 3.12: Kapitza-Dirac scattering for various pulse duration of a 1 W 1064 nm lattice. The pulse transfers atoms to various $2n\hbar k$ states. Here $k = \frac{2\pi}{\lambda \sin(\frac{\theta}{2})}$ is the effective wavevector of the 1064 nm light, θ is the lattice beams intersection angle, and $n = 0, \pm 1, \pm 2...$ as labeled by dashed lines. (a) A molecular BEC at 720 G at $t = 0$. (b) Momentum distribution of the BEC for lattice pulse duration of 1.6 μs, and (c) 2.8 μs. To measure the momentum distribution, we wait a time-of-flight of T/4 = 8 ms after the lattice pulse before taking the absorption image.

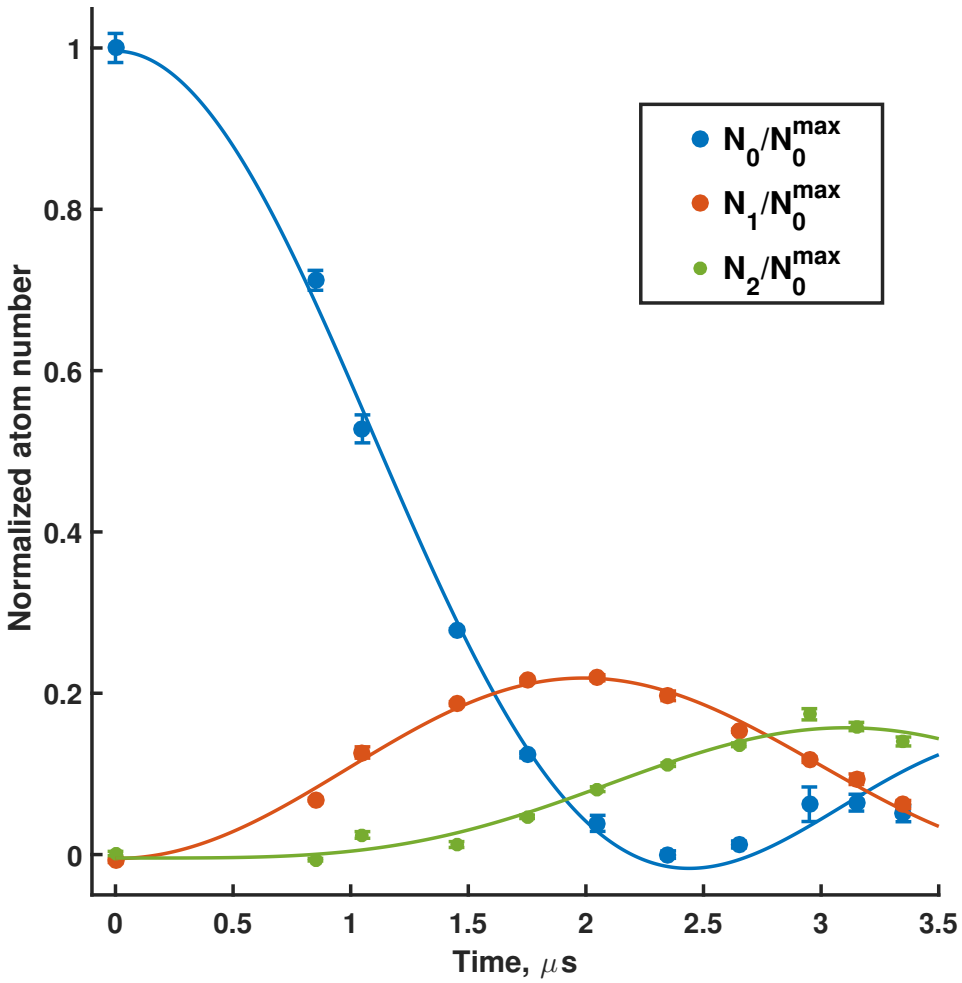

FIGURE 3.13: Normalized atom number in the lowest three scattering orders plotted as a function of pulse duration for a 1 W 1064 nm lattice. By fitting the time dependent probability using $P_n(t) = J_n^2(\frac{V_0 t}{2\hbar})$ for the lowest three orders where $n = 0$ (blue), $n = 1$ (red), and $n = 2$ (green), the extracted lattice depth is $21.00 \pm 0.34\, E_R^{1064}$, $19.72 \pm 0.20\, E_R^{1064}$, and $20.90 \pm 0.70\, E_R^{1064}$ respectively.

is small enough to see a uniform lattice, as shown in Fig 3.12(a). We vary the pulse duration and wait for the band map time before taking the absorption image. The band map time, as discussed in Sec 2.3 is a quarter of period T/4 = 8 ms, allowing different orders to reach $x = \frac{2n\hbar k}{m\omega}$, $n \in integers$. The absorption image is taken with the vertical camera, which integrates over the expanded direction. Here $k = \frac{2\pi}{\lambda \sin\left(\frac{\theta}{2}\right)}$ is the effective wavevector of the 1064 nm beam. Pictures for two different pulse

durations are presented in Fig 3.12(b) and (c). We find the atom number for each scattering order and fit using eq 3.4 to extract the lattice depth V_0, as shown in Fig 3.13. For a 1 W 1064 nm lattice beam, the average depth for all three orders is $20.6\,E_R^{1064}$ [4] ($E_R^{1064} \approx 14.8$ kHz denotes the recoil energy of the infrared lattice), which is close to our estimate of $19\,E_R^{1064}$ using the measured waist size of 100 μm at focus.

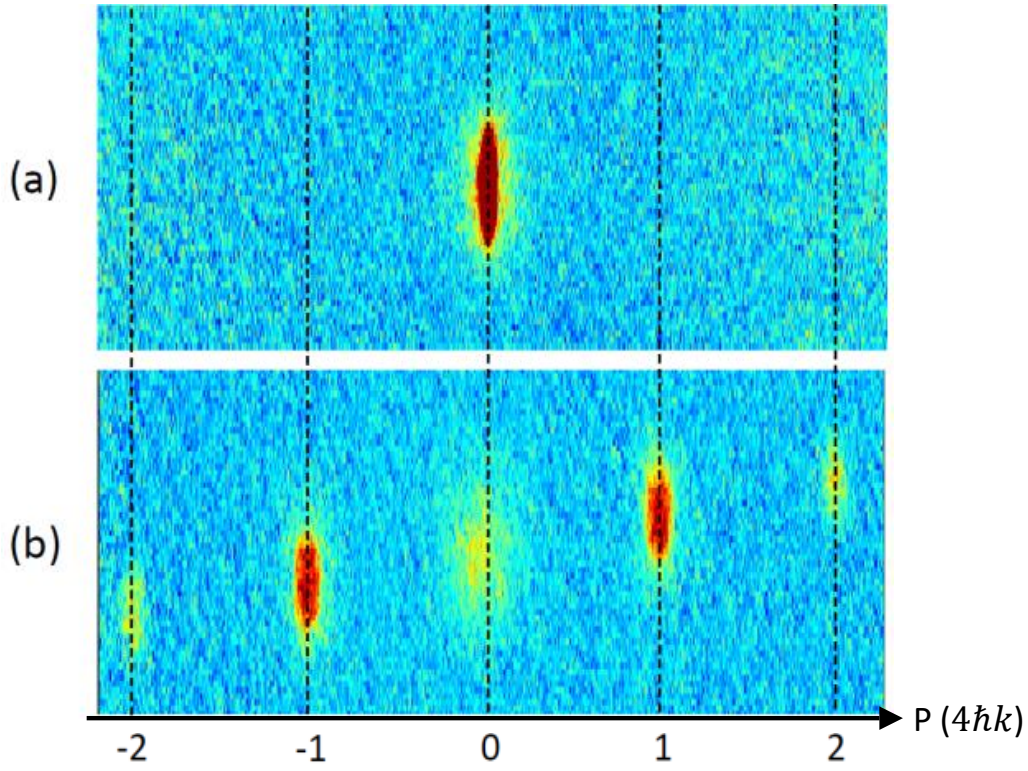

FIGURE 3.14: Kapitza-Dirac scattering for various pulse duration of 1 W 532 nm lattice. The pulse transfers atoms to various $4n\hbar k$ states. Here $k = \frac{2\pi}{\lambda \sin(\frac{\theta}{2})}$ is the effective wavevector of the 1064 nm light, θ is the lattice beams intersection angle, and $n = 0, \pm 1, \pm 2...$ as labeled by dashed lines. (a) A molecular BEC at 720 G at $t = 0$. (b) Momentum distribution of the BEC for lattice pulse duration of 1.6 μs. To measure the momentum distribution, we wait a time-of-flight of T/4 = 8 ms after the lattice pulse before taking the absorption image.

[4] For determination of E_R^{1064}, the lattice spacing, in other words the intersection angle between the two lattice beams, has to be measured with reasonable precision. This is presented in Sec 3.4

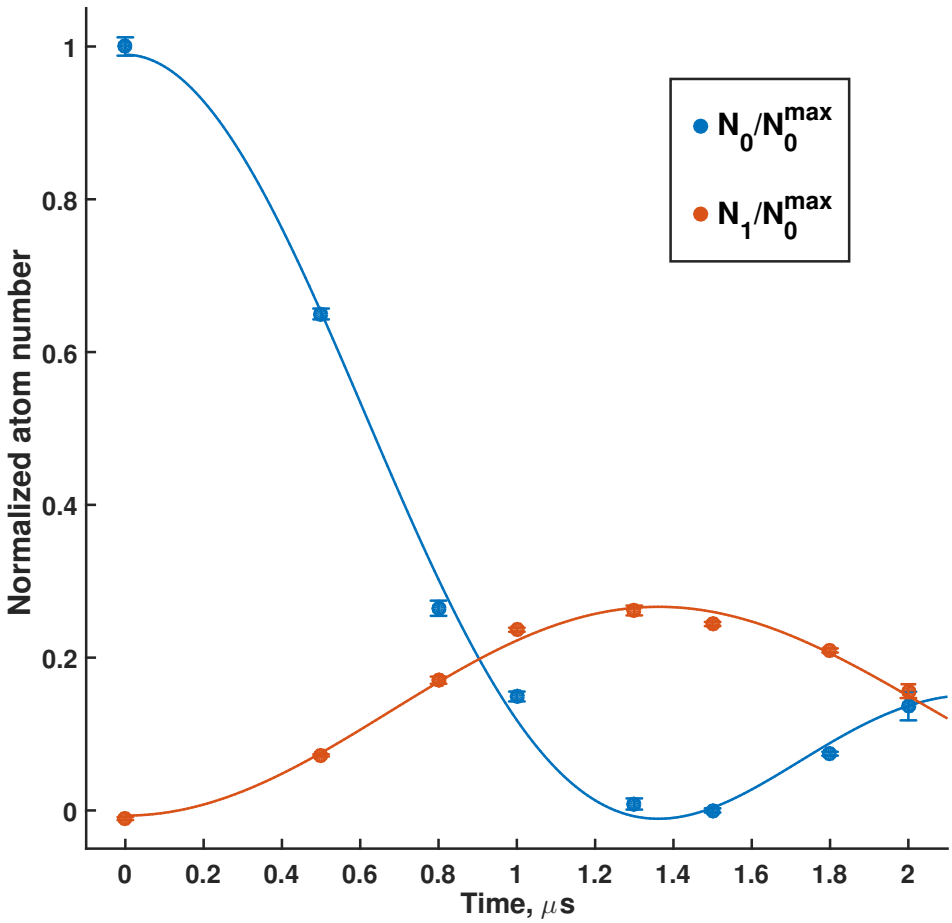

FIGURE 3.15: Normalized atom number in the lowest two scattering orders plotted as a function of pulse duration for a 1 W 532 nm lattice. By fitting the time dependent probability using $P_n(t) = J_n^2(\frac{V_0 t}{2\hbar})$ for the lowest two orders where $n = 0$ (blue), and $n = 1$ (red), the extracted lattice depth is $9.41 \pm 0.17\, E_R^{532}$, and $7.20 \pm 0.09 E_R^{532}$ respectively

We switch to pulsing a 1 W 532 nm lattice on the BEC, as shown in Fig 3.14. Varying the pulse duration and waiting T/4 for atoms to scatter into $x = \frac{4n\hbar k}{m\omega}$, $n \in$ *integers*, since 532 nm light has a wave vector twice of the 1064 nm light. A average lattice depth of 8.45 E_R^{532} [5] is found by extracting the V_0 for each order, as shown in Fig 3.15. However this result is less reliable since the recoil energy of the green lattice is 4 times that of the infrared due to its short wavelength, thus the lattice depth is not enough to sufficiently transfer the atoms for a pulse duration of $\tau \ll 1/\omega_{rec}$.

[5] $E_R^{532} = 4 \times E_R^{1064}$

3.7 Band Mapping

To calibrate the chemical potential of the system when atoms are loaded into the lattice, it is important to measure the quasi-momentum distribution of the gas by doing a band map. Band mapping is accomplished by ramping down the lattice potential gradually on a timescale that is fast compared to the tunneling timescale in the lowest band of the lattice, but adiabatic with respect to interband transitions [59, 60], such that the quasi-momentum distribution becomes the momentum distribution q is determind from the momentum distribution $p = nG_0 + q$. For band mapping inside a harmonic trap, the spatial distribution at quarter period $t = T/4$, recovers the momentum distribution at time zero regardless of the initial position distribution, as discussed in Sec 2.3.

When doing the band map, we first align the lattice beams to the center of a shallow (0.5% full depth) CO_2 laser trap at a magnetic field $B = 1200$ G.[6] We load the atoms into the lattice after forced evaporative cooling of a mixture of the lowest two hyperfine states of ^{6}Li, denoted as $|1\rangle$ and $|2\rangle$, in a CO_2 dipole trap as described in previous sections. After loading into the lattice, we sweep to 1200 G where the two-body interaction is suppressed and remove state $|2\rangle$ with a resonant optical imaging pulse. After removing state $|2\rangle$, we are left only with noninteracting state $|1\rangle$ which preserves momentum during expansion.

To transfer the quasi-momentum into momentum, for a $20\,E_R$ 1064 nm lattice, we exponentially lower the lattice for $800\,\mu$s. We then wait T/4 = 8 ms for the cloud to expand along the lattice direction in the shallow harmonic confinement of a 0.5% CO_2 laser trap and the magnetic bowl arising from the bias magnetic field. The result is shown in Fig 3.16(a). The edge of the cloud falls off abruptly at

[6] The CO_2 trap center slightly shifts for different magnetic field. It is therefore better to align to the center of the final trap in which the atoms will expend.

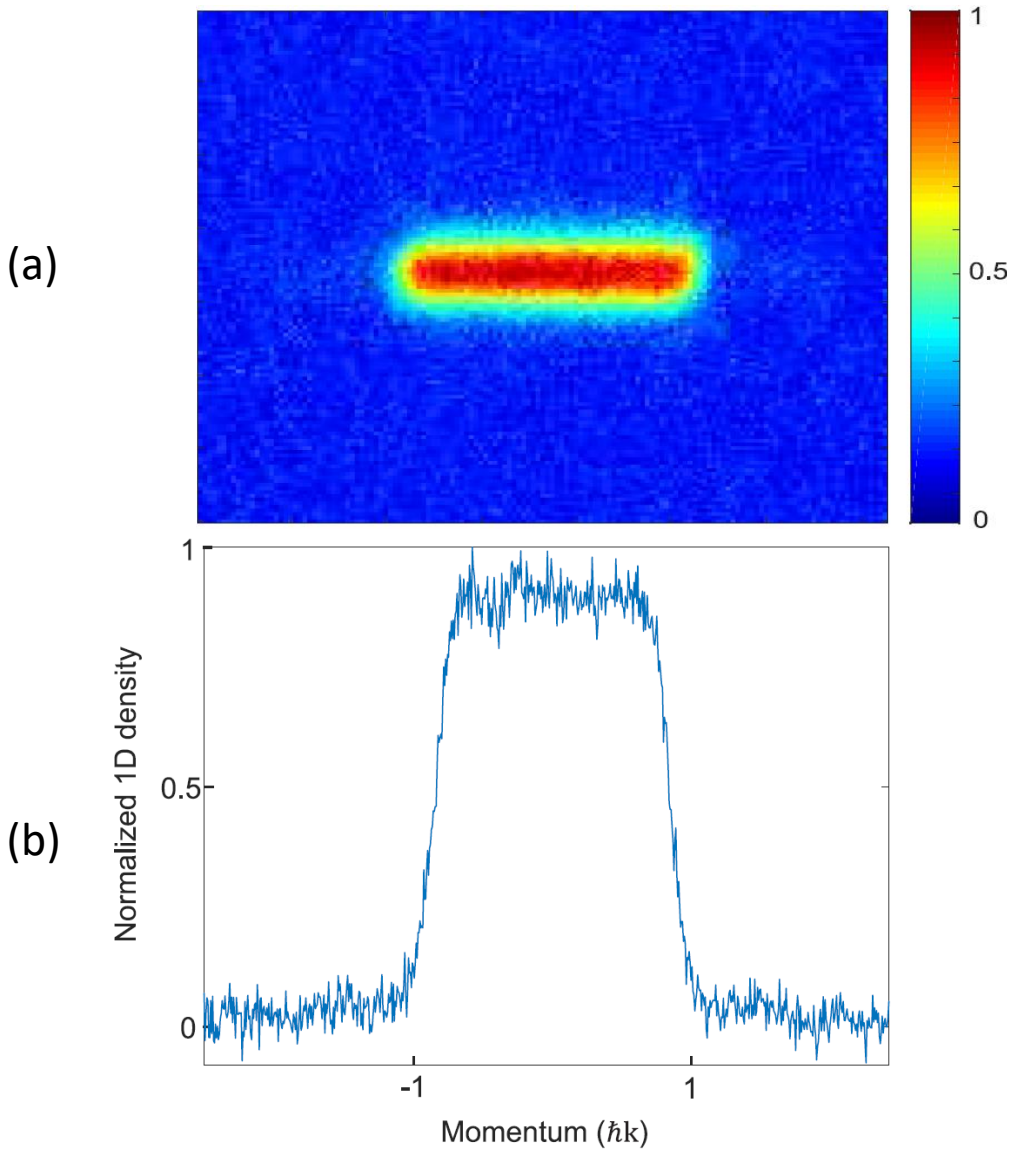

FIGURE 3.16: Band mapping of a $s_1 = 20$ $\lambda_1 = 1064$ nm lattice. (a) Absorption image taken after ramping down the lattice for 800 μs and waiting T/4 = 8 ms for the cloud to expand along the lattice direction inside the harmonic trap. (b) The two dimensional density distribution in (a) is integrated radially. Note that the images are binned every 4 pixels in the horizontal direction.

$x = \pm\frac{\hbar k}{m\omega}$ with respect to the center of the cloud, where $k = \frac{2\pi}{\lambda \sin\left(\frac{\theta}{2}\right)}$ is the 1064 nm beam effective wave vector. The fall-off matches the first Brillouin zone boundary at quasi-momentum $q = \pm\hbar G_0/2$ where the reciprocal lattice vector $G_0 = 2k$. The radially integrated profile, which shows better visibility of the shoulder at the zone

boundary is presented in Fig 3.16(b).

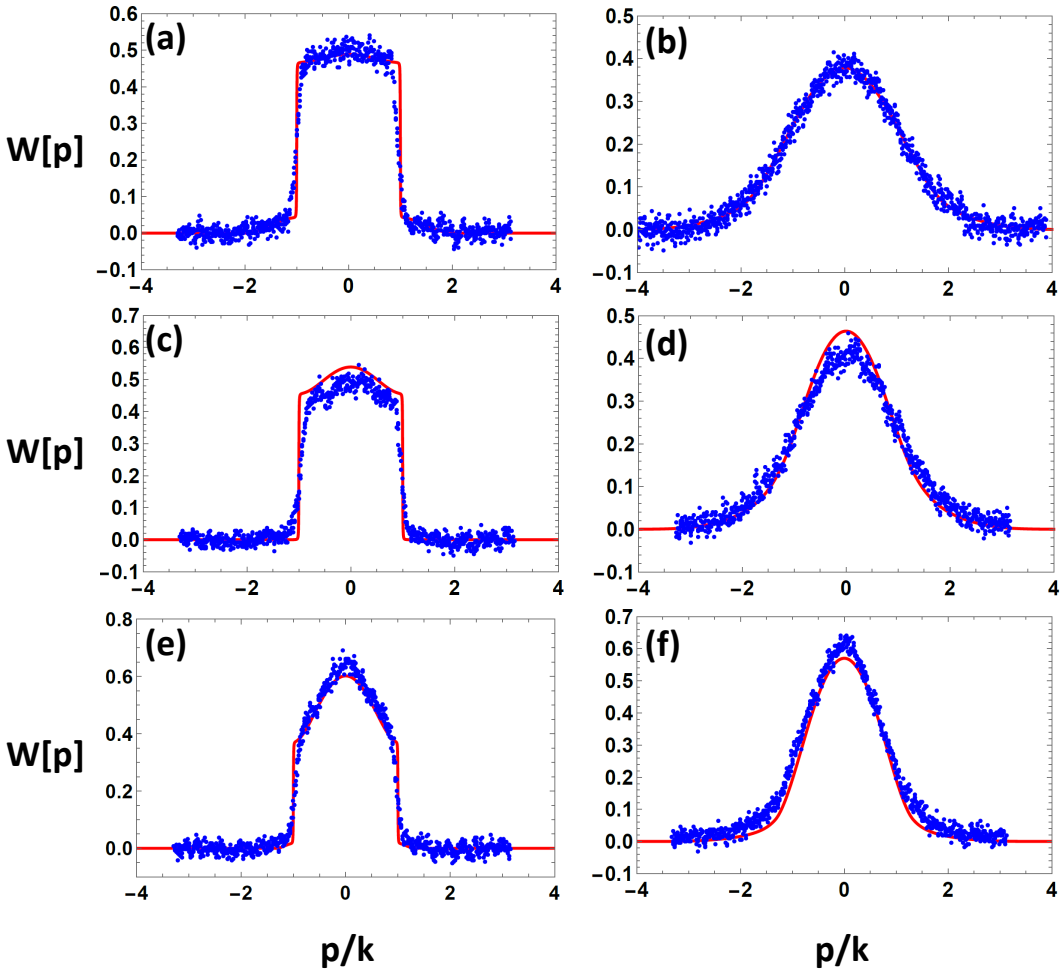

FIGURE 3.17: Quasi-momentum and momentum distributions for various chemical potentials μ and lattice depths s_1. The red curves are theoretical prediction using equations derived in Sec 2.3. (a) Quasi-momentum distribution and (b) momentum distribution for $\mu = 4E_R$ and $s_1 = 8$. (c) Quasi-momentum distribution and (d) momentum distribution for $\mu = 2E_R$ and $s_1 = 5.5$. (e) Quasi-momentum distribution and (f) momentum distribution for $\mu = 2E_R$ and $s_1 = 2.8$.

To observe the effect of chemical potential on band maps, we vary the chemical potential by changing the atom number or the CO_2 trap potential. As shown in Fig 3.17, the left column shows the quasi-momentum distribution, which corre-

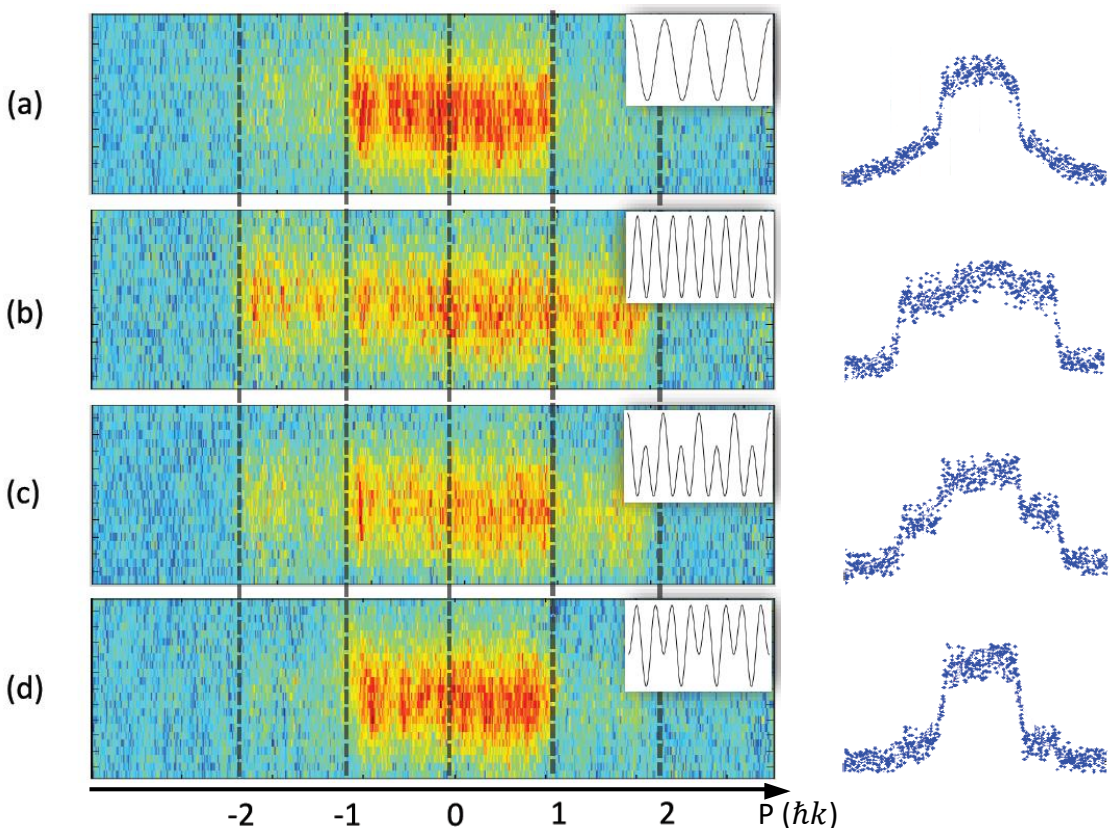

FIGURE 3.18: Comparison between several band maps. Band map of (a) A 1064 nm lattice of $s_1 = 10$; (b) A 532 nm lattice of $s_2 = 20$; (c) A bichromatic lattice of $s_1 = 10$, $s_2 = 20$, $\phi = 0$ and (d) $s_1 = 10$, $s_2 = 20$, $\phi = \pi$. Atom numbers are the same for all cases. All absorption image taken after ramping down the lattice for 800 μs and waiting T/4 = 8 ms for the cloud to expand along the 4% CO_2 axial direction. The dashed lines denote the Brillouin zone center at 0 and zone boundaries at $\pm\hbar k$ and $\pm 2\hbar k$. Here $k = \frac{2\pi}{\lambda \sin\left(\frac{\theta}{2}\right)}$ is the effective 1064 nm lattice wave vector. Insets show the lattice potential, and the radially integrated profiles are shown in the right column.

sponds to adiabatic lowering of the lattice potential, while the right column shows the momentum distribution corresponding to abrupt turning off of the lattice. The red curves show theoretical prediction using equations derived in Sec 2.3. One sees that less chemical potential results in a band map picture that is rounded on the top.

We fix the atom number at $N_0 \approx 60,000$ for band mapping of various lattices,

as shown in Fig 3.18. Fig 3.18(a) shows the band map of a $10\,E_R$ 1064 nm lattice. The atomic density distribution has a sharp shoulder at $p = \pm\hbar k$. A pedestal-like profile extending towards $p = \pm 2\hbar k$ implies the chemical potential falls in between the ground and first excited band. In Fig 3.18(b), the band map of a $10\,E_R$ 532 nm lattice has a sharp cutoff at $p = \pm 2\hbar k$. The cutoff position corresponds to the 1st Brillouin zone boundary of a wave vector $2k$.

Fig 3.18(c) shows the band map of a bichromatic lattice of $V(z) = V_1 \cos^2(kz) + V_2 \cos^2\left(2kz + \frac{\phi}{2}\right)$, where $V_1 \equiv -s_1 E_R < 0$ for the red-detuned 1064 nm lattice and $V_2 \equiv s_2 E_R > 0$ for the blue-detuned 532 nm lattice and $s_1, s_2 > 0$ as defined in Sec 2.2. For $s_1 = 10$, $s_2 = 20$, and relative phase $\phi = 0$, a superlattice with symmetric double wells is formed. Recall Fig 2.4(b), when introducing the secondary lattice and choosing relative phase to be $\phi = 0$, the superlattice becomes a periodic structure of symmetric double wells, which brings the ground and first excited bands close to degeneracy. Therefore, for a similar chemical potential to Fig 3.18(a), the lowest two bands are occupied. As can be seen in Fig 3.18(c), the band map picture extends to $p = \pm 2\hbar k$ as one would expect. Fig 3.18(d) is the band map of the bichromatic lattice when $\phi = \pi$, where regions in between $\hbar k$ and $2\hbar k$ almost vanishes, since the degeneracy between lowest two bands is lifted due to the phase, as we previously showed in Fig 2.4(d).

3.8 Trap Frequency Measurement

For single beam optical traps or in deep optical lattices, the effective trap potential for atoms is approximately harmonic. To characterize the harmonic potential, we measure the oscillation frequencies of noninteracting atoms. When the trap depth is modulated sinusoidally at twice the harmonic trap frequency, the atoms are para-

metrically excited from the ground to second excited harmonic oscillator state[7] and its energy exponentially increases with time. As a consequence, one observes an increase of the cloud size, or a loss of atoms, at the resonance frequency for each direction.

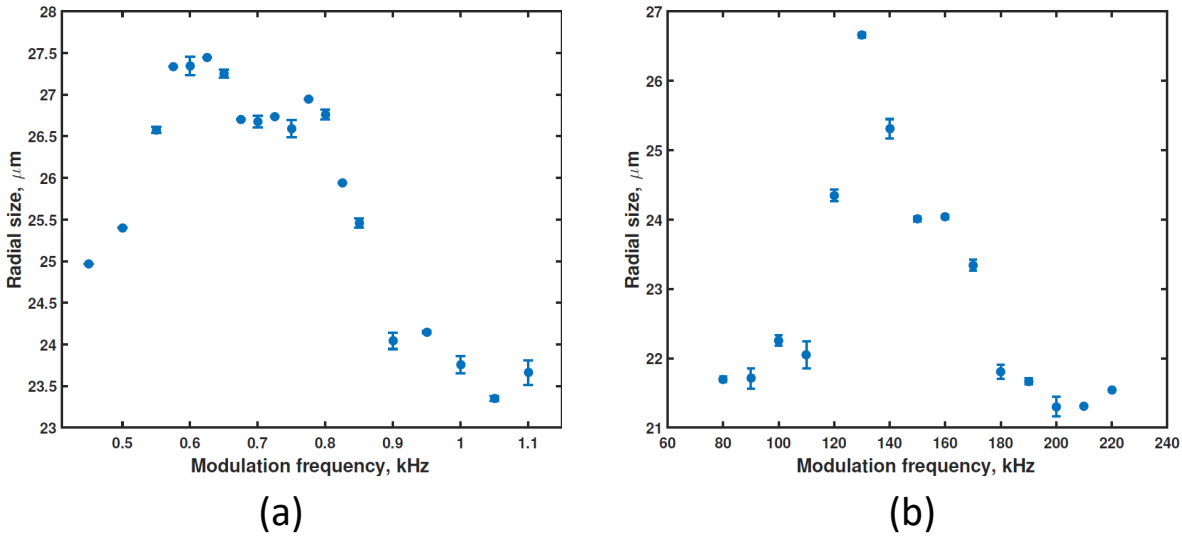

FIGURE 3.19: Lattice frequency measurement for a 1064 nm lattice of $s_1 = 13$ using parametric resonance. When modulating the lattice depth at the resonant frequency, the size of the cloud increases. We show here the growth in radial size. (a) Radial resonance occurs around 600 Hz and 800 Hz. (b) Axial resonance has a peak at 140 kHz, a slow rise at 120 kHz and a sharp fall at 180 kHz.

To estimate the resonance frequencies, we consider a simple case as follows. By retro-reflecting a cylindrically symmetric Gaussian beam of Rayleigh length z_R and waist w_0, a standing wave potential has a fast periodic spatial modulation along the beam propagating direction z,

$$V(r,z) = -\frac{V\cos^2 kz}{1+(z/z_R)^2}\, e^{-\frac{2r^2}{w_0^2}}. \tag{3.5}$$

We can write V in units of E_R, i.e. $V \equiv sE_R$. Omitting the relatively slowly-varying

[7] Transitions between ground and first excited state in a harmonic potential induced by modulating the trap depth are not allowed due to the symmetry of the potential V, thus $\langle\Psi_0|V|\Psi_1\rangle = 0$.

z-dependence of z^2/z_R^2, one can obtain the expression

$$\begin{aligned} V(r,z) &= -sE_R(1-k^2z^2+O(z^4))\left(1-\frac{2r^2}{w_0^2}\right) \\ &\approx \frac{1}{2}m\omega_z^2z^2+\frac{1}{2}m\omega_r^2r^2. \end{aligned} \tag{3.6}$$

Thus the axial and the radial harmonic frequencies are

$$\omega_z=\frac{2\sqrt{s}E_R}{\hbar},\ \omega_r\equiv\sqrt{\omega_z\omega_y}=\sqrt{\frac{4sE_R}{mw_0^2}}\ . \tag{3.7}$$

For a 1064 nm lattice of depth $s = 13$ and waist w_0=100 μm, the estimated harmonic trap frequencies are $\omega_r = 2\pi * 360$ Hz, $\omega_z = 2\pi * 110$ kHz. Fig 3.19(a) shows two radial parametric frequencies around 600 Hz and 800 Hz, due to anisotropy in the two radial directions. The peak positions are close to twice the estimated harmonic trap radial frequency using eq. 3.7, i.e. $2 * 360 = 720$ Hz.

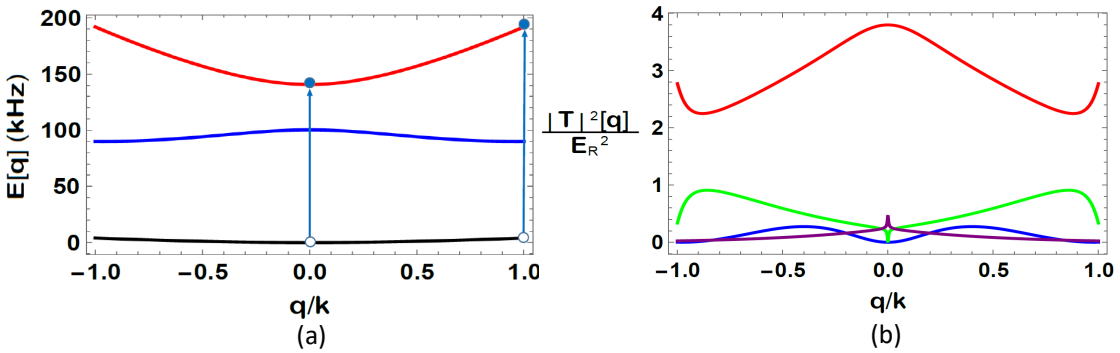

FIGURE 3.20: Ground to second excited band transition frequency and transition matrix element squared of a $s_1 = 13$ lattice. (a) The transition frequency has a range of $f \in [140, 185]$ kHz. 140 kHz corresponds to a $|1\rangle$-$|3\rangle$ transition frequency at $q = 0$. 185 kHz corresponds to a $|1\rangle$-$|3\rangle$ transition frequency at $q = k$. Note that q is conserved for the transition. (b) The quasi-momentum dependent transition matrix element squared. Blue: 1→2, Red: 1→3, Green: 1→4, Purple: 1→5.

However, for a moderate lattice depth, the harmonic well description is not appropriate. We solve for the band structure to figure out the transition frequencies

required for transitions from ground to second excited band denoted as $1 \rightarrow 3$. For a lattice depth of $s = 13$, the $1 \rightarrow 3$ transition frequency according to a band calculation has a range of $f \in [140, 185]$ kHz, as shown in Fig 3.20(a). 140 kHz corresponds to a $|1\rangle$-$|3\rangle$ transition frequency at $q = 0$. 185 kHz corresponds to a $|1\rangle$-$|3\rangle$ transition frequency at $q = k$. The quasi-momentum dependent transition matrix element squared is shown in Fig 3.20(b). We compare this result to a parametric measurement spectrum shown in Fig 3.19(b). When modulating at the $1 \rightarrow 3$ frequency, the atoms are transferred to the second excited band which has a larger tunneling rate, therefore the cloud size increases. We show the radial size measurement has a peak at a modulating frequency of 140 kHz and a sharp fall at 180 kHz. The sharp cutoff corresponds to the band gap, and the range agrees reasonably well with prediction. The slow rise from 120 kHz is due to the radial variation of the lattice intensity.

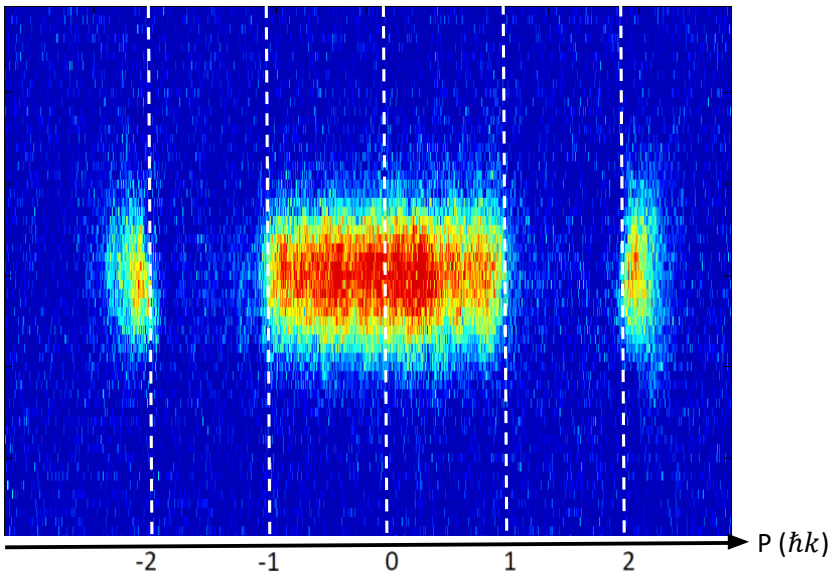

FIGURE 3.21: Band map for a sinusoidally modulated 1064 nm lattice of $s_1 = 20$, with modulation amplitude of 13% for 1.3 ms at 110 kHz for $1 \rightarrow 3$ transition.

We find that extracting the lattice depth using Kapitza-Dirac scattering is more

reliable than parametric resonance, since there's one fit parameter, i.e., the lattice depth, for all scattering orders at different times, while modulation spectroscopy provides a range of frequencies, which requires more interpretation.

We also show in Fig 3.21 the band map after sinusoidally modulating a $s_1 = 20$ 1064 nm lattice by 13% for 1.3 ms at 110 kHz for $1 \rightarrow 3$ transition. After lattice modulation, we do a band map by ramping down the lattice adiabatically for 800 μs, and allowing the gas to expand in the harmonic trap for a time-of-flight of T/4 = 8 ms before taking the absorption image. The quasi-momentum is transferred into the measured momentum distribution. Modulating at 110 kHz transfers atoms from ground to second excited band, therefore atomic density distribution shows up in $|p| > 4\hbar k$ regions in the band map.

3.9 Calibrating the Relative Phase of the Bichromatic Lattice

We used the Soleil-Babinet phase Compensator to control the relative phase between the two lattices to construct periodic double well structures of various symmetries. The Babinet compensator is made with crystal quartz and is a continuously variable phase retarder that operates over a wide range of wavelength. It consists of two birefringent wedges, a fixed one and another one with adjustable position mounted on a translational stage. By moving the position of one wedge to change the optical path length through the crystal, one can continuously vary the phase retardation.

The 1064 nm and 532 nm lattice beams are orthogonally polarized and aligned to the fast and slow axis of the birefringent crystal to maximize the relative phase retardation between the two. To calibrate the relative phase difference after passing through the Babinet compensator, we combine the two color beams and intersect them at a small angle ($\theta \approx 2^\circ$) to interfere. We image the interference pattern directly with a camera.

As shown in Fig 3.22, the top half is the interference pattern of the 1064 nm

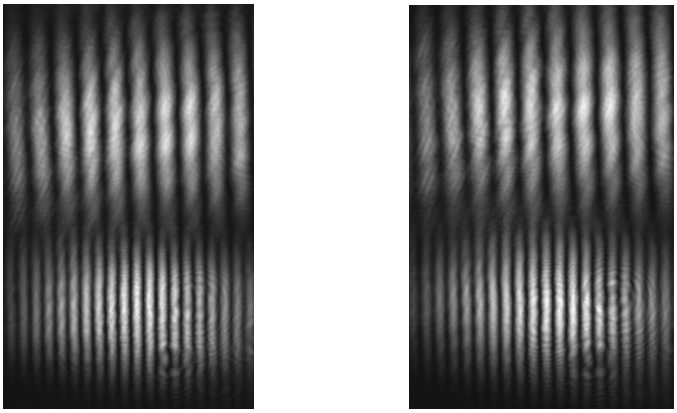

FIGURE 3.22: The top half is the interference pattern of the infrared beam, and the lower is that of the green. By changing the Babinet micrometer position, the relative pattern shifts. (a) Micrometer at 0, and (b) micrometer at 1.75 mm.

beam, and the lower half is for the 532 nm beam. By turning the micrometer to adjust the wedge position, the interference patterns shift with respect to each other. The relative interference patterns repeat after moving the micrometer by 3.5 mm, which corresponds to a relative phase change of 2π.

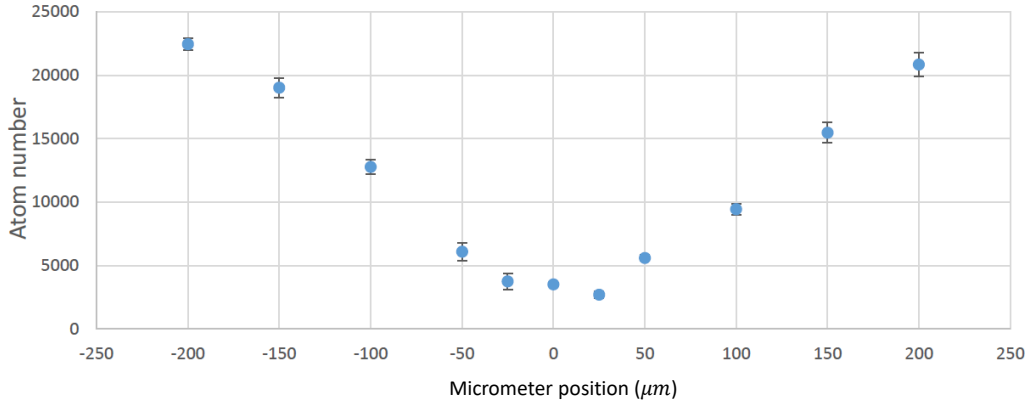

FIGURE 3.23: Phase dependent loading for a bichromatic lattice of $s_1 = 20$, $s_2 = 10$ when varying the relative phase ϕ. When $\phi = 0$, which corresponds to the zero in the horizontal axis, presumably we have a symmetric double well superlattice configuration.

When atoms are loaded into the bichromatic optical lattice, we can determine the relative phase indirectly by measuring the phase dependent loading. When the node of the green lattice is aligned to the node of the infrared, naively speaking one would expect to observe minimum atom loading because the attractive force is maximally canceled. To observe atom loss with better sensitivity, we choose to load the atoms into a bichromatic lattice of $s_1 = 20$, $s_2 = 10$ (E_R is the recoil energy of the 1064 nm lattice.) and a relatively weak radial confinement of CO_2 laser trap to record the phase dependent atom number. We use a CO_2 laser trap which is 0.25% of the maximum trap depth. As can be seen from Fig 3.23, the atom number is not sensitive within a ± 50 μm ($d\phi = 2\pi/35$) range where the atom number reaches its minimum. We normally place the Babinet compensator within this range and define the relative phase to be 0, where each site of the superlattice is presumably a symmetric double well, where the 1064 nm attractive and the 532 nm repulsive lattice potentials are of opposite sign.

4

Fermi Gases from 2D to Quasi-2D

We present in this thesis work the first systematic study of both pairing and thermodynamics of ultracold Fermi gases continuously varied from two dimensional (2D) to quasi-2D. A system is 2D if it is free to move in two dimensions x and y while tightly confined in the third direction z, such that only the ground state in the z direction is occupied. Assuming harmonic confinement, a gas is 2D if only the z harmonic oscillator ground state, whose energy is $\frac{1}{2}h\nu_z$, is occupied. Conversely, the system is quasi-2D if higher states in the tightly confined direction are also occupied. For a gas loaded in a deep one dimensional optical lattice, when the radial Fermi energy E_F is small compared to $h\nu_z$, the energy difference between two states in the tight confinement direction, the gas is 2D, as shown in Fig 4.1. In contrast, the gas is quasi-2D when E_F and $h\nu_z$ are comparable, such that higher axial states are occupied.

Quasi-two-dimensional (quasi-2D) geometries play important roles in high temperature superconductors [65], layered organic superconductors [66], and semiconductor interfaces [67]. In high-transition temperature copper oxide and organic superconductors, electrons are confined in a quasi-two-dimensional configuration, creating

complex, strongly interacting many-body systems, for which the phase diagrams are not well understood [68]. Enhancement of the critical temperature T_c for the quasi-2D regime, as compared to true 2D regime, has been predicted for thin films in parallel magnetic fields [69] and for quasi-2D Fermi gases containing atoms in excited states of the tightly confined direction [29], where T_c may exceed the 3D value. Ultracold atomic Fermi gases in 2D and quasi-2D geometries provide model systems, which have been the subject of numerous predictions [5, 22, 23, 24, 29, 30, 70, 71, 72, 73, 74, 75, 76, 77] and experiments [3, 4, 6, 7, 8, 9, 10, 11, 12, 78, 79, 80, 81].

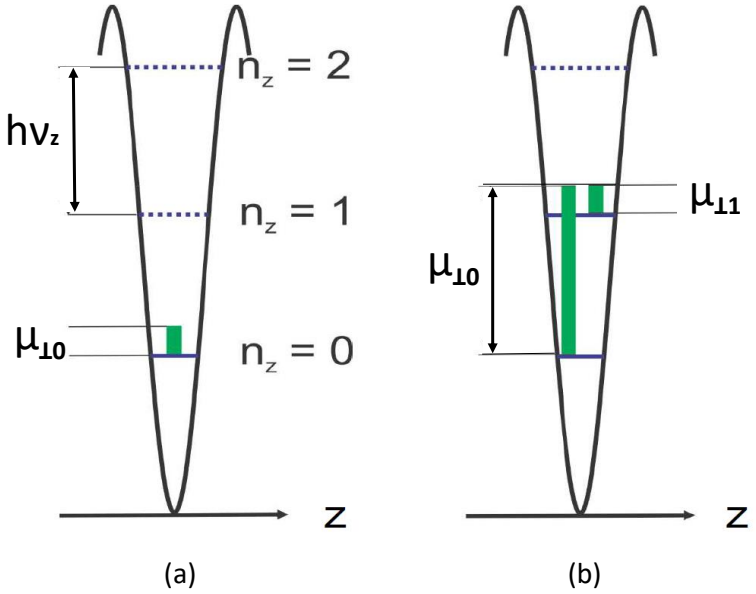

FIGURE 4.1: Defining the dimensionality of the gas. A deep optical lattice is generated along the z-direction by intersecting two $\lambda = 1064$ nm beams. (a) When the radial chemical potential $\mu_\perp$ is small compared to $h\nu_z$, the gas is 2D. (b) The gas is quasi-2D when the radial chemical potential is comparable to $h\nu_z$, when higher axial states are occupied.

In 2D systems, the dimer binding energy $E_b \geqslant 0$ sets the natural scale of length for scattering interactions [20], but a many-body treatment is required for $E_F > E_b$, as the inter-atom spacing is then smaller than the dimer size [5]. 2D-BCS mean field theory (MFT) [5] provides an elegant treatment of this problem, but MFT is expected to fail in 2D systems, as noted by Randeria and Taylor [21] and shown

in many recent predictions [22, 23, 24, 25, 26, 27, 28]. For quasi-2D systems, the effect of the third dimension on the equation of state and pairing energies is not yet understood [29, 30].

Radio frequency spectra obtained with $E_F/h\nu_z << 1$, in the 2D regime [3, 4], reveal that the absorption threshold is close to E_b, a 2D-BCS (Bardeen-Cooper-Schrieffer) mean field prediction [5] that one would not have expected to be quantitatively valid in 2D [21]. Although one might expect similar 2D-behavior for a quasi-2D gas with $E_F/h\nu_z \simeq 1$, the measured spectra are in strong disagreement with BCS mean field theory [6], as are the measured thermodynamic properties [7, 8, 9, 10, 11, 12], which require a beyond mean field treatment. However, prior to this thesis work there has been no experimental study of the thermodynamic properties in the 2D regime. We study a two-component ^{6}Li Fermi gas in a new trap geometry that can be smoothly tuned from 2D to quasi-2D. The dimensionality of the gas within each single layer is tuned from 2D to quasi-2D by continuously by increasing the radial Fermi energy using the adjustable radial confinement of a CO_2 laser potential. We are able to measure both the radio frequency spectra and radial cloud profiles under identical conditions for each regime. For the quasi-2D gas, we find that the spectra are inconsistent with 2D-BCS theory. For the 2D gas, we find that the spectra can be fit by 2D-BCS mean field theory, consistent with previous work[3, 13]. In contrast to the spectra, we find that the radii for 2D clouds are much smaller than those predicted by 2D-BCS mean field theory, which yields ideal gas density profiles[14]. Our results show that there is no transition between 2D and quasi-2D systems and that beyond mean field descriptions are required in both regimes, consistent with predictions.

4.1 Experimental Realization of Dimensional Crossover

For this experiment, we use only the fundamental lattice of wavelength $\lambda_1 = 1064$ nm from our bichromatic optical lattice setup. Two 1064 nm beams intersecting at an angle of $\theta = 91^\circ$, create an optical lattice with lattice spacing of 0.746 μm, which tightly confine atoms along the z direction. This lattice is superposed on a CO_2 laser dipole trap, as shown in Fig 2.2(a), which provides radial confinement. By changing the CO_2 laser trap depth, one has control over the radial harmonic oscillator frequency $\omega_\perp$.

The interaction strength of a balanced (50-50) mixture of atoms in the two lowest hyperfine components, denoted $|1\rangle$ and $|2\rangle$, of ^{6}Li is tuned using the broad Feshbach resonance at 832.2 G [18, 19]. The radial trap frequency $\omega_\perp$ and the total number of atoms in one site N$\approx$ 2000 determines the ideal 2D gas radial Fermi energy, $E_F = \hbar\omega_\perp\sqrt{N}$. The interaction strength is characterized by the parameter E_F/Eb_{12}, where Eb_{12} is the binding energy of a 1-2 dimer inside the lattice. We change the dimensionality of each site by tuning the ratio of E_F to the harmonic oscillator energy level spacing $h\nu_z \equiv 2\sqrt{s}E_R$ in the tightly confined z-direction, with s being the lattice depth in units of E_R. For $s = 15$, $h\nu_z$ is $h \times 116$ kHz. As shown in Fig 4.1, at zero temperature, the gas is 2D for $E_F/h\nu_z \ll 1$, since all atoms are in the ground axial state of the lattice. For $E_F/h\nu z \approx 1$, the gas is quasi-2D, since higher axial states are populated.

4.2 RF Spectroscopy from 2D to Quasi-2D

Radio frequency spectroscopy is a very powerful tool to study the pairing energy. With this new trap geometry that is smoothly tunable from 2D to quasi-2D, we are able to measure rf spectra for each regime. We begin by calculating the transition

spectrum using Fermi's golden rule and compare it to the measured spectrum.

4.2.1 Calculating the RF Transition Spectrum

The Hamiltonian for the ^{6}Li ground state hyperfine interactions in a magnetic field is

$$H = \frac{a_{hf}}{\hbar^2}\mathbf{S}\cdot\mathbf{I} - \frac{\mu_0}{\hbar}(g_J\mathbf{S} + g_I\mathbf{I})\cdot\mathbf{B}. \tag{4.1}$$

The first term comes from the hyperfine interaction and the second term comes from magnetic field Zeeman shift $-\mathbf{m}\cdot\mathbf{B}$. The magnetic moment is $\mathbf{m} = \frac{\mu_0}{\hbar}(g_J\mathbf{S} + g_I\mathbf{I})$ contains both electric-spin and nuclear magnetic dipole moments, which interact with the bias magnetic field $\mathbf{B} = B\hat{\mathbf{e}}_z$.

For ^{6}Li which has S=1/2 and I=1, there are six hyperfine states, as shown in Fig 4.2. The original degenerate states for both $F = \frac{3}{2}$ (blue lines) and $F = \frac{1}{2}$ (red lines) split into six different states as the magnetic field increases. Here we only list the lowest 3 in increasing order of energy from $|1\rangle$ to $|3\rangle$. We normally trap and work with the lowest two states $|1\rangle$ and $|2\rangle$ in our experiments.

$$\begin{aligned}
|1\rangle &\equiv |(S=\frac{1}{2}, I=1), F=\frac{1}{2}, m_F=\frac{1}{2}\rangle \\
&= -\sin\theta_+|m_S=\frac{1}{2}, m_I=0\rangle + \cos\theta_+|m_S=-\frac{1}{2}, m_I=1\rangle \\
|2\rangle &\equiv |(S=\frac{1}{2}, I=1), F=\frac{1}{2}, m_F=-\frac{1}{2}\rangle \\
&= -\sin\theta_-|m_S=\frac{1}{2}, m_I=-1\rangle + \cos\theta_-|m_S=-\frac{1}{2}, m_I=0\rangle \\
|3\rangle &\equiv |(S=\frac{1}{2}, I=1), F=\frac{3}{2}, m_F=-\frac{3}{2}\rangle \\
&= |m_S=-\frac{1}{2}, m_I=-1\rangle.
\end{aligned} \tag{4.2}$$

In eq. 4.2, $\sin\theta_\pm = [1+(Z_\pm+R_\pm)^2/2]^{-1/2}$, $\cos^2\theta_\pm = 1-\sin^2\theta_\pm$, and $Z_\pm = \frac{\mu_0 B}{a_{hf}}(-g_J+$

$g_I) \pm \frac{1}{2}$, $R_\pm = \sqrt{2 + (Z_\pm)^2}$. For large $\mathbf{B}$, $R_\pm \to \infty$ and $Z_\pm \to \infty$, $\sin\theta_\pm$ terms vanish and $\cos\theta_\pm \to 1$.

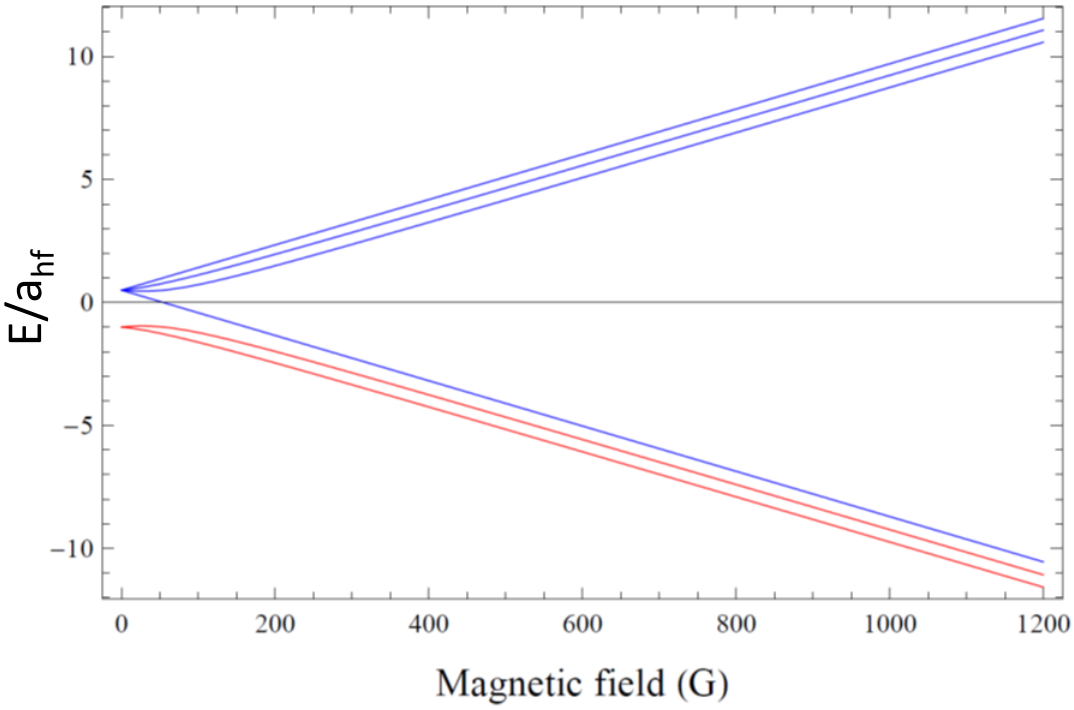

FIGURE 4.2: Hyperfine energies of ^{6}Li versus magnetic fields. E_1 lowest to E_6 highest.

The magnetic dipole interaction for a radio frequency (rf) pulse is $V(t) = -\mathbf{m} \cdot \mathbf{B}_{rf}(t)$, where $\mathbf{B}_{rf}(t) = \hat{\mathbf{e}}_x B^0_{rf} \cos\omega t$ and $\mathbf{m}$ is the magnetic dipole moment. It is important to note that the rf field must be perpendicular to the quantization axis of the states (in this case the B-field lies along the z-axis while rf B-field is in the x direction) in order to make transitions that change the magnetic quantum number m. Since $|g_I|$ is very small compared to $|g_J|$, we can ignore the nuclear magnetic moment term and write $m_x \simeq g_J \mu_0 S_x/\hbar \simeq -2\mu_0 \frac{S_+ + S_-}{2\hbar}$. One sees that rf transitions can not occur between states $|1\rangle$ and $|3\rangle$, since $|\Delta m| = 2$. For transitions between states $|1\rangle$ and $|2\rangle$ or between states $|2\rangle$ and $|3\rangle$, since $|\Delta m| = 1$, transitions are allowed. The Rabi frequency $\Omega_{kn} = \frac{1}{\hbar}\langle k|m_x|n\rangle B^0_{rf}$ is proportional to both the rf magnetic field

amplitude B^0_{rf}, and the magnetic dipole matrix element $\langle k|m_x|n\rangle$.

In our experiment, we start with a mixture of states $|1\rangle$ and $|2\rangle$. We drive an rf transition from $|2\rangle$ to $|3\rangle$ and monitor the remaining number of atoms in state $|2\rangle$. The initial and final state two-atom wavefunctions are

$$\begin{aligned} |\,i\rangle &= \frac{1}{\sqrt{2}}(|1\rangle_a|2\rangle_b - |1\rangle_b|2\rangle_a)|I\rangle, \\ |f\rangle &= \frac{1}{\sqrt{2}}(|1\rangle_a|3\rangle_b - |1\rangle_b|3\rangle_a)|F\rangle. \end{aligned} \tag{4.3}$$

Here, a and b denote the two atoms, $|1\rangle$, $|2\rangle$, $|3\rangle$, are hyperfine states. The relative motion states(dimer or scattering) that are denoted as $|I\rangle$ and $|F\rangle$ are symmetric under exchange of atoms, where a and b denotes different atoms. To anti-symmetrize the whole wavefunction, we make the atom pair hyperfine state anti-symmetric.

From Fermi's golden rule, the radio frequency induced transition rate out of the initial state i to all possible final states f is

$$R_i(\omega_{rf}) = \frac{2\pi}{\hbar}\sum_f |V_{fi}|^2 \delta(E_f - E_i - \hbar\omega_{rf}). \tag{4.4}$$

The transition matrix element $|V_{fi}|$ is

$$\begin{aligned} V_{fi} &= \frac{1}{2}\left(\langle 1|_a\langle 3|_b - \langle 1|_b\langle 3|_a\right) m_x \left(|1\rangle_a|2\rangle_b - |1\rangle_b|2\rangle_a\right) B^0_{rf}\langle F|I\rangle \\ &= \hbar\,\Omega_{32}\langle F|I\rangle. \end{aligned} \tag{4.5}$$

Ignoring the many-body physics and treating the two-body problem interacting via s-wave scattering, we can solve for the atom-pair(dimer) binding energy inside a harmonic potential using a self-consistent integral equation [82],

$$\frac{l_z}{a} = \int_0^\infty \frac{du}{\sqrt{4\pi u^3}}\left[1 - \prod_j \left(\frac{2\beta_j u}{1-e^{-2\beta_j u}}\right)^{1/2} e^{-\epsilon_b u}\right]. \tag{4.6}$$

Here $E_b = \epsilon_b \hbar\omega_z$ is the pair binding energy, $\beta_j = \frac{\omega_j}{\omega_z}$ is the ratio between harmonic trap frequencies, $l_z = \sqrt{\hbar/(m\omega_z)}$ is the harmonic oscillator length scale, and $a = a(B)$ is the s-wave scattering length. A Green's function approach is used obtain eq. 4.6 for the binding energies and eigenfunctions for bound and scattering states. See Sec 5.1 for detailed derivation.

The solution of the relative motion part wavefunction for an initial $|1\rangle$-$|2\rangle$ paired state is

$$|I\rangle = \phi_0(z)\psi_{12}(\rho) = \frac{\kappa_{12}}{\sqrt{\pi}}\phi_0(z)K_0\left(\kappa_{12}\rho\right).$$

The rf pulse can drive a $|2\rangle \rightarrow |3\rangle$ transition and leads to a final $|1\rangle$-$|3\rangle$ paired state, or a $|1\rangle$-$|3\rangle$ scattering state. The corresponding wavefunctions are [82]

$$\langle\rho|F\rangle_{paired} = \frac{\kappa_{13}}{\sqrt{\pi}}\phi_0(z)K_0\left(\kappa_{13}\rho\right), \tag{4.7}$$

$$\langle\rho|F\rangle_{scatter} = \phi_0(z)\frac{1}{\sqrt{A}}\left[J_0(k_{13\perp}\,\rho) - \frac{\pi i}{\pi i + \ln\left(\frac{E_b^{13}}{E_f^{13}}\right)}H_0^{(1)}(k_{13\perp}\,\rho)\right]. \tag{4.8}$$

Here $\phi_0(z)$ is the ground state axial harmonic oscillator wave function

$$\phi_0(z) = \frac{1}{(2\pi l_z^2)^{1/4}}e^{-(\frac{z}{2l_z})^2}, \tag{4.9}$$

, K_0 is a modified Bessel function with $\kappa_{ij} = \sqrt{\epsilon_{b\,ij}}/l_z$, the $|1\rangle$-$|3\rangle$ binding energy $E_b^{13} = \epsilon_{b\,13}\hbar\omega_z$, the transverse kinetic energy $E_f^{13} = \frac{\hbar^2 k_{13\perp}^2}{m}$, and A is the transverse area for a box-normalized plane wave.

Using Fermi's golden rule, eq. 4.4 and 4.5, we obtain the normalized transition spectrum for a $|1\rangle$-$|2\rangle$ bound state to a $|1\rangle$-$|3\rangle$ bound state,

$$R_{12b\rightarrow 13b}(\nu) = \pi^2\Omega_{fi}^2\frac{q^2}{4\,\sinh^2\left(\frac{q}{2}\right)}\,\delta\left(\nu - \frac{E_b^{12} - E_b^{13}}{h}\right), \tag{4.10}$$

where $q = \ln(E_b^{12}/E_b^{13})$. The normalized transition spectrum for a $|1\rangle$-$|2\rangle$ bound state to a $|1\rangle$-$|3\rangle$ scattering state has the following form [6]

$$R_{12b\to 13f}(\nu) = \pi^2 \Omega_{fi}^2 \frac{E_b^{12}}{h\nu^2} \frac{q^2 \Theta(\nu - E_b^{12}/h)}{\left[q - \ln\left(\frac{h\nu}{E_b^{12}} - 1\right)\right]^2 + \pi^2}. \tag{4.11}$$

4.2.2 RF Spectra for 2D and Quasi-2D Fermi Gases

To probe the pairing energy, we probe the transition from the atomic hyperfine state $|2\rangle$ to a higher lying, initially empty hyperfine state $|3\rangle$. We record the number of atoms remaining in $|2\rangle$ as a function of the excitation frequency relative to the bare atom hyperfine transition frequency, ν_{32}^0 i.e., $\Delta\nu_{RF} \equiv \nu_{RF} - \nu_{32}^0$. We measure ν_{32}^0 using a high temperature, low density $|1\rangle$-$|2\rangle$ mixture, which agrees with measurements for a noninteracting cloud containing atoms only in $|2\rangle$. We then observe the rf spectra in low temperature mixtures, which exhibit a shifted pairing peak, as shown in Fig. 4.3 for $B = 1005$ G and in Fig. 4.4 for $B = 834$ G.

We consider first the measurements in the 2D regime, the upper spectra in Fig. 4.3 and Fig. 4.4. In our experiments, where $E_F \geqslant E_{b12}$, we expect many-body physics to be important, as the interparticle spacing is then comparable to or smaller than the dimer size. For the 2D regime, we can try to apply 2D-BCS theory for a true 2D system [72]. In this case, the 2D-BCS prediction for a $|2\rangle \to |3\rangle$ transition with a noninteracting final state ($E_{b13} << E_{b12}$) is $h\Delta\nu_{RF} = E_{b12}$, precisely the dimer pairing energy, as noted previously [4, 6]. However, in our experiments E_{b13} is not negligible, so we determine the 2D spectrum including the $\ln(E_{b13}/E_{b12})$-dependence arising from final state interactions according to eq. 4.10 and eq. 4.11 [6, 83]. For our case, the bound to bound transition dominates.

For a lattice of depth only 15 E_R, the energy levels are not equally spaced by $h\nu_z$, as for a harmonic oscillator. Therefore, instead of using eq. 4.6 to calculate the dimer binding energies inside a harmonic well, we determine the dimer binding

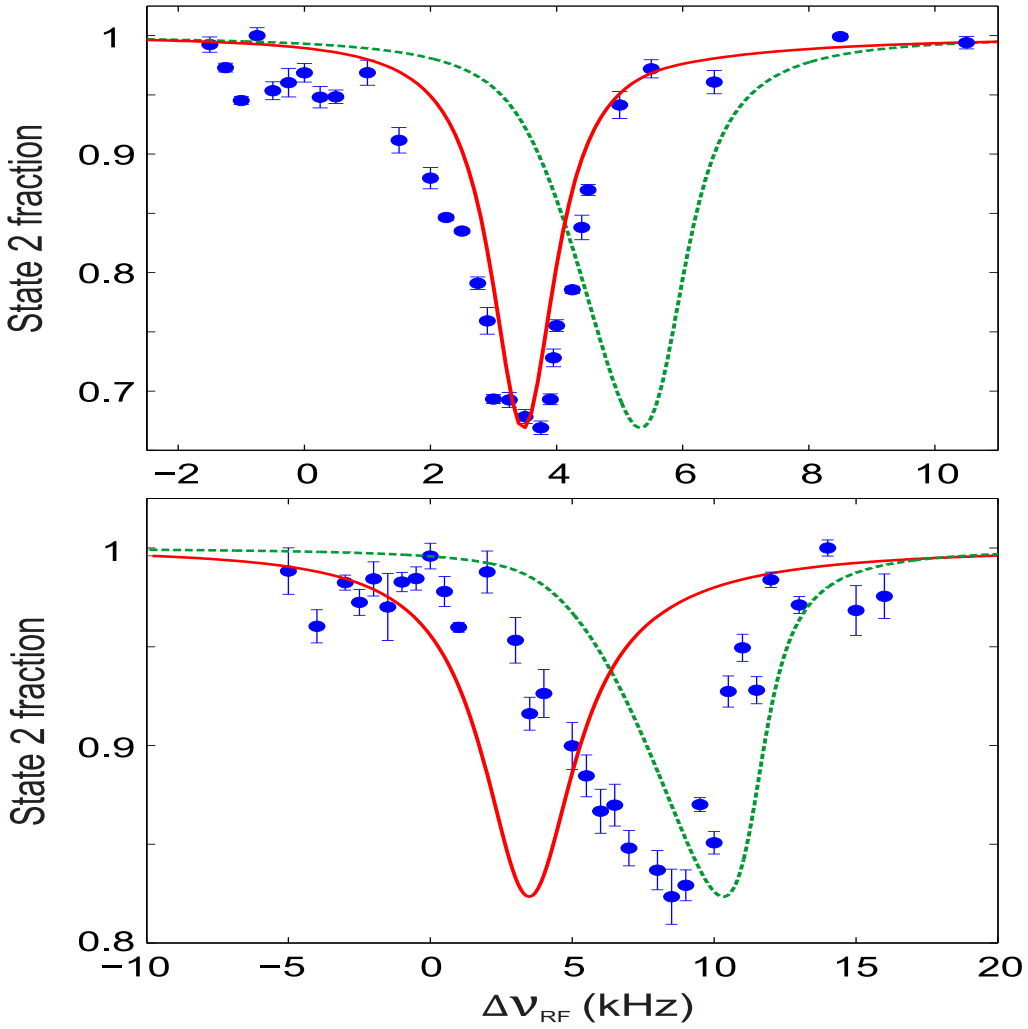

FIGURE 4.3: Radio-frequency spectra at $B = 1005$ G with $\nu_z = 116$ kHz. Top: 2D regime with $E_F/h\nu_z = 0.16$, $E_{b12}/h\nu_z = 0.044$, $E_F/E_{b12} = 3.57$, and $E_{b13}/h\nu_z = 0.016$. Bottom: Quasi-2D regime with $E_F/h\nu_z = 0.75$, $E_{b12}/h\nu_z = 0.044$, $E_F/E_{b12} = 17.1$, and $E_{b13}/h\nu_z = 0.016$. The fraction of atoms remaining in hyperfine state 2 is measured as a function of radio-frequency relative to the bare atom $2 \rightarrow 3$ resonance frequency. The solid-red (dashed-green) curves denote the dimer (polaron) prediction with no free parameters (top) and fitted width $w = 4$ kHz (bottom)

.

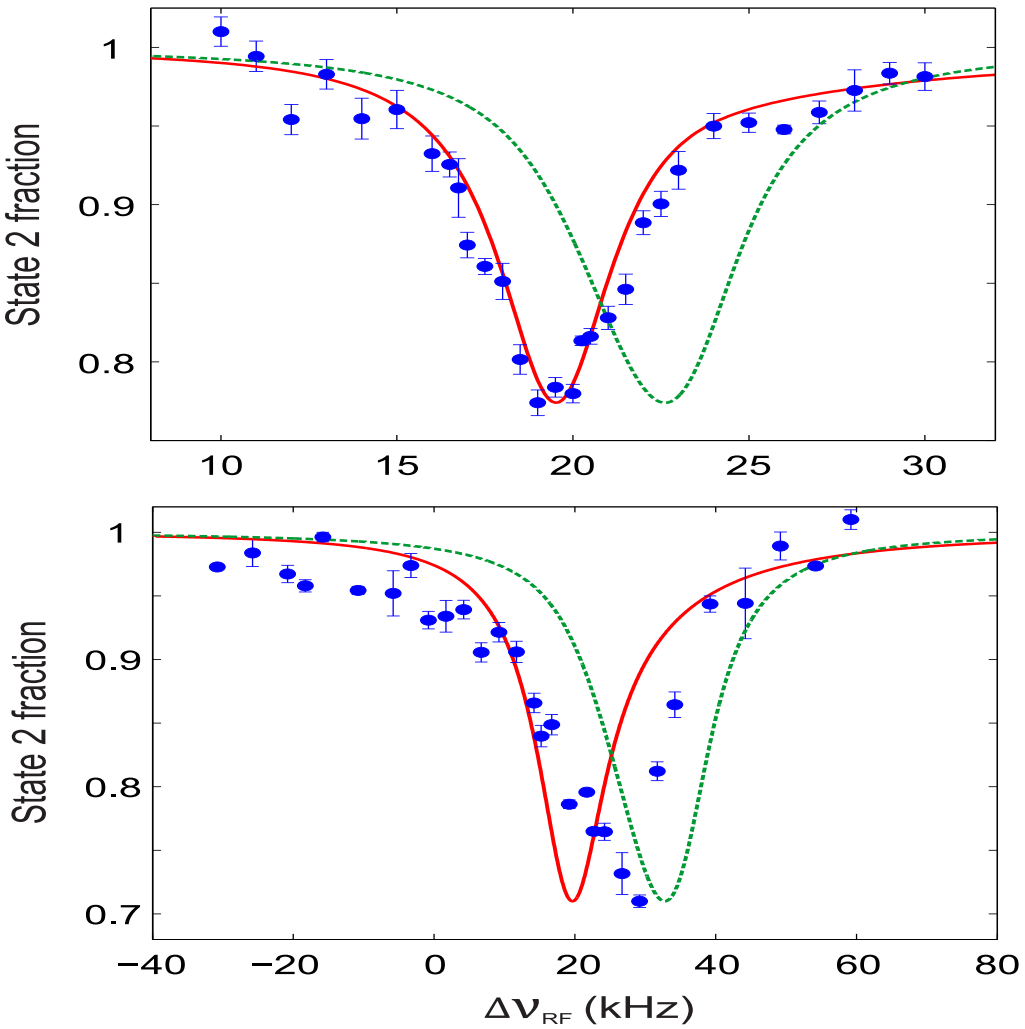

FIGURE 4.4: Radio-frequency spectra at $B = 834$ G with $\nu_z = 116$ kHz. Top: 2D regime with $E_F/h\nu_z = 0.125$, $E_{b12}/h\nu_z = 0.20$, $E_F/E_{b12} = 0.62$, and $E_{b13}/h\nu_z = 0.032$. Bottom: Quasi-2D regime with $E_F/h\nu_z = 0.67$, $E_{b12}/h\nu_z = 0.20$, $E_F/E_{b12} = 3.32$, and $E_{b13}/h\nu_z = 0.032$. The fraction of atoms remaining in hyperfine state 2 is measured as a function of radio-frequency relative to the bare atom $2 \rightarrow 3$ resonance frequency. The solid-red (dashed-green) curves denote the dimer (polaron) prediction with no free parameters (top) and fitted width $w = 12$ kHz (bottom).

energies in the finite-depth optical lattice using the technique we present in detail in Sec 5.2 [84]. The sum of the calculated 2D spectra determined by eq. 4.10 and eq. 4.11 are convolved with a Lorentzian of width w (FWHM). We believe that the linewidth w arises from the short lifetime of the excited state $|3\rangle$ in the $|1\rangle - |2\rangle$ mixture, as we were not limited by spectroscopic resolution with our pulse duration of 30 ms. For the 2D data, we measure $w = 1.3$ kHz at 1005 G and $w = 4.3$ kHz at 834 G, using the observable atomic $|2\rangle \rightarrow |3\rangle$ resonance. For the quasi-2D data, the corresponding widths of 4 kHz and 12 kHz are found by fitting, as we could not measure the spectrum of the atomic resonance contribution. For the upper (2D) spectra in Fig 4.3 and in Fig 4.4, where $E_F/h\nu_z = 0.16$ and 0.13, respectively, we find that dimer spectra, as predicted by 2D-BCS theory, are in very good agreement with the data, as shown by the calculated red curves.

Now we examine the measurements in the quasi-2D regime, shown as the lower spectra in Fig 4.3 and Fig 4.4, where $E_F/h\nu_z \geqslant 0.67$. Here, we find that 2D-BCS theory does not fit the data. Recently, zero temperature 2D-BCS theory has been extended to include higher axial states [30], which one expects would contribute in the quasi-2D regime. The predictions show that in the quasi-2D regime, the pairing resonances should be significantly shifted upward in frequency as observed, but quantitative agreement is not obtained [85].

We also consider a 2D-Fermi-polaron model, where spin-down atoms act as impurities dressed by particle-hole clouds in a sea of spin-up atoms. We extend this picture by assuming that the polarons are fermionic and weakly interacting, so that the model is applicable even for a 50-50 mixture of both spin states. This heuristic model predicts several features of our previous data in the quasi-2D regime [6, 8] and is consistent with more detailed treatments based on the Bethe-Goldstone equation [86, 87], which describes two-body interactions in a many-body system.

In the spectra, the model predicts a resonance for $h\Delta\nu_{RF} = E_{p13} - E_{p12}$, where

the energy of each state is given by

$$E_p = y(q)\epsilon_F. \tag{4.12}$$

Here, $\epsilon_F = \pi\hbar^2\, n/m$ is the local Fermi energy, m is the atom mass, and n is the total density for the 50-50 mixture. An approximate form for the dimensionless factor $y(q)$ is [86, 87],

$$y(q) = \frac{-2}{\ln(1+2\,q)}, \tag{4.13}$$

where $q \equiv \epsilon_F/E_b$. This analytic result interpolates between the molecular regime (neglecting the molecular mean field) at magnetic fields well below the Feshbach resonance and agrees with the Fermi polaron approximation [6] and recent QMC predictions [88] for $\epsilon_F/E_b > 3$.

The dashed-green curves in the spectra of Fig 4.3 and Fig 4.4 show the predictions using eq. 4.13, with

$$I(\Delta\nu) \propto \int \frac{2\pi\rho\, d\rho\, n(\rho)}{1+(2/w)^2\left[\Delta\nu - (E_{p13}-E_{p12})/h\right]^2}, \tag{4.14}$$

where the 2D-density $n(\rho)$ is determined from fits to the measured column density profiles. As the density decreases, the local Fermi energy decreases from its maximum value, producing a downward sweeping broad spectrum, consistent with the data. We see that the 2D-polaron spectrum based on eq. 4.13 predicts resonances in reasonable agreement with the quasi-2D data.

4.3 Cloud Radii for 2D and Quasi-2D Fermi Gases

The cloud radii can be a measure of the equation of state, which determines the density profile of the trapped gas. In previous studies of quasi-2D spin-imbalanced and spin-balanced clouds [8], we have measured both the cloud radii and the pressure for $E_F/h\nu_z = 1.5$. There, we find that the 2D-polaron model gives a reasonable fit

for the measured radii and pressure, while 2D-BCS theory for a balanced gas predicts an ideal gas pressure and ideal gas cloud profiles [8, 72], in strong disagreement with the measurements.

Fischer and Parish [29] have extended finite temperature 2D-BCS theory to include higher axial states, which are expected to contribute to the thermodynamics in the quasi-2D regime. In this case, the predicted pressure decreases below the ideal gas pressure with increasing $E_F/h\nu_z$, but it is well above the 2D-polaron prediction [8], which agrees with measurements in the quasi-2D regime [8, 12].

With this new trap geometry that is smoothly tunable from 2D to quasi-2D, we are able to measure radial cloud profile for each regime.

4.3.1 Phase-Contrast Imaging

Due to the high density of the 2D atomic samples, we choose to use phase-contrast imaging technique instead of absorption imaging. With this technique, we can image using a detuned beam and avoid accelerating atoms when imaging with a large intensity resonant probe beam, which would be needed to penetrate the high density cloud.

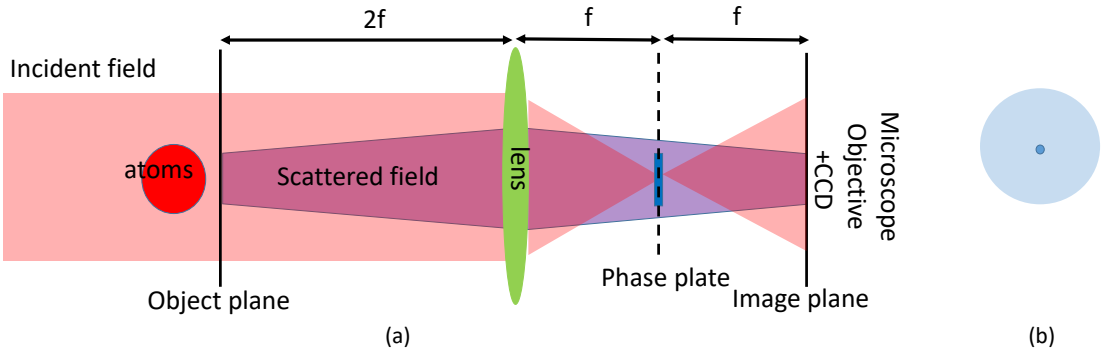

FIGURE 4.5: Setup for phase-contrast imaging. (a) The incident field is phase shifted by the phase plate, whereas the scattered field is not. (b) Front view of the phase plate. A dot of 0.5 mm diameter is coated in the center of a thin window for $\lambda/4$ phase retardation.

In phase-contrast imaging, we place a phase plate at the focal plane of the imaging lens, as shown in Fig 4.5. This phase plate has a dot of 0.5 mm diameter coated in the center of a thin window. The collimated incident field focuses tightly in the focal plane and is intercepted by the phase plate which retards the incident field by $\lambda/4$. The scattered field is uncollimated, thus large in the Fourier plane, and is not affected by the phase plate. The two beams interfere at the image plane, which in turn is imaged onto a ccd array.

As the probe beam pass through the atoms, it gets attenuated by the transition amplitude t and gains an extra phase shift $e^{i\phi}$. We can write the electric field strength in the object plane immediately after the atomic cloud as [89, 90],

$$E(x,y) = tE_0(x,y)e^{i\phi}. \tag{4.15}$$

Both the attenuation coefficient t and the phase shift ϕ depend on the off-resonance optical density $\tilde{D} = \tilde{n}\sigma_0/(1+\delta^2)$ in the following form,

$$t = e^{-\frac{\tilde{D}}{2}} \; ; \phi = -\delta\frac{\tilde{D}}{2}. \tag{4.16}$$

Here the column density $\tilde{n} = \int n(\mathbf{r})dz$, is the three dimensional density distribution $n(\mathbf{r})$ integrated over the probe beam propagation direction z, $\delta = \frac{2(w-w_0)}{\Gamma}$ is the detunning in units of half linewidth, and σ_0 is the resonant optical cross-section. The D2 line of ^{6}Li has a linewidth of $\Gamma = 2\pi \times 5.87$ MHz. In the following discussion, for simplicity, we approximate $t \to 1$ for large detuning δ.

The electric field in the object plane can be decomposed into two parts, the incident field $E_0(x,y)$, and the scattered field $E_0(x,y)(te^{i\phi}-1)$. For a 2f-to-2f imaging setup, the scattered field is not affected by the phase plate, so $E_{scat} = -E_0(-x,-y)(te^{i\phi}-1)\exp[\frac{-iq(x^2+y^2)}{2f}]$ at the image plane[1]. Here q is the propagation wave vector and f is the focal length of lens. We assume that the phase plate only

[1] We use the paraxial propagator $g(x-x';y-y';d) = \frac{-iq}{2\pi d}\exp[\frac{iq}{2d}((x-x')^2+(y-y')^2)]$

causes a phase shift of $\alpha = \pi/2$, without attenuating the incident field, so $t \simeq 1$. The incident field reaching the image plane is $E_{inc} = -e^{i\alpha} E_0(-x,-y) \exp[\frac{-iq(x^2+y^2)}{2f}]$.

At the image plane, for the 4f configuration the intensity distribution $I(x,y)$ is proportional to the square of the total field with a coefficient $C = \frac{c\epsilon_0}{2}$, where c is the speed of light, ϵ_0 is the permittivity,

$$\begin{aligned} I(x,y) &= C|E_{scat} + E_{inc}|^2 \\ &= C|E_0|^2 \, |e^{i\alpha} + (e^{i\phi} - 1)|^2 \\ &= C|E_0|^2 \, [3 - 2\sqrt{2}\cos(\phi + \frac{\pi}{4})]. \end{aligned} \tag{4.17}$$

The corresponding reference image when no cloud is present, is

$$I_0(x,y) = C|E_0|^2 \, [3 - 2\sqrt{2}\cos(\frac{\pi}{4})]. \tag{4.18}$$

Normalizing the intensity distribution, we obtain,

$$\frac{I(x,y) - I_0(x,y)}{I_0(x,y)} = 2[1 - \sqrt{2}\cos(\phi + \frac{\pi}{4})]. \tag{4.19}$$

In reality, we do not have to take the limit of $t \to 1$, thus eq. 4.19 is a function of t and ϕ as defined in eq. 4.16. We numerically extract the density by properly choosing the detuning so that $\cos(\phi + \frac{\pi}{4})$ for local density n is single valued. Taking $t \to 1$ results in a 10% error. For our measurements, we use a detuning of about 13 linewidths.

4.3.2 Measured Cloud Radii for 2D and Quasi-2D Fermi Gases

Our measured spectra for the 2D regime appear to agree with 2D-BCS mean field theory, which predicts dimer spectra, consistent with the 2D spectra obtained in Refs. [3, 4]. To examine the 2D-BCS predictions further, we use the in-situ phase-contrast method to image the dense clouds in the 2D regime with $E_F/h\nu_z \leqslant 0.18$.

From the atom number and peak column density [8], we obtain the cloud radii shown in Fig 4.6.

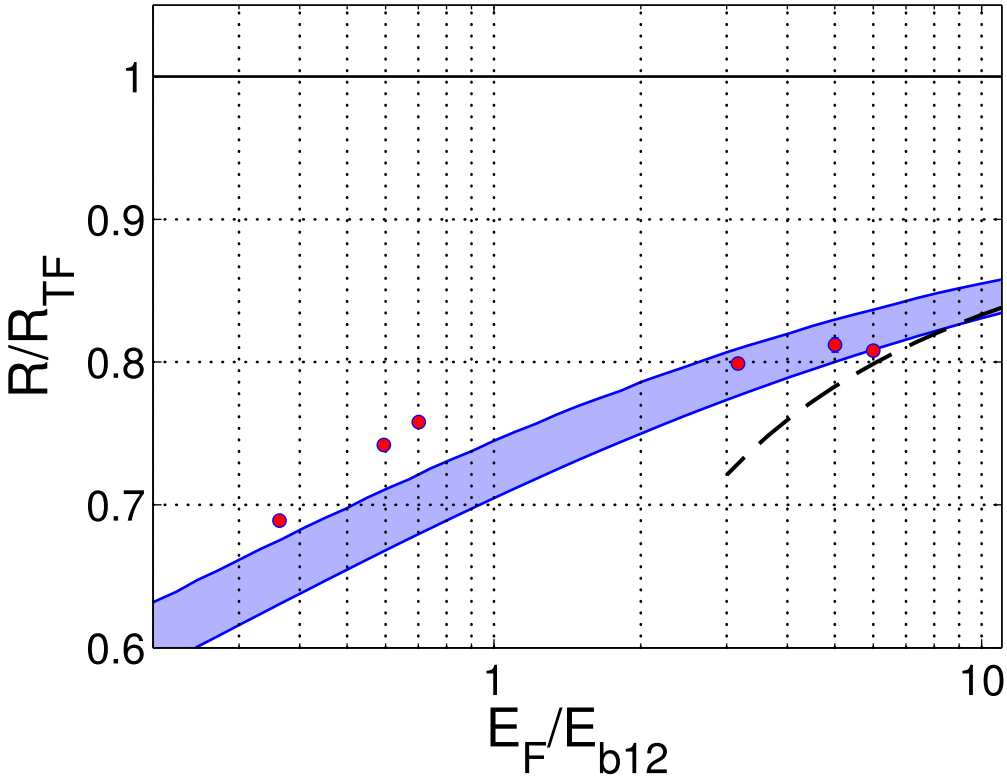

FIGURE 4.6: Cloud radii versus E_F/E_b, where E_F is the radial Fermi energy for an ideal gas, R_{TF} is the Thomas-Fermi radius, and E_{b12} is the 2D dimer binding energy of a $1-2$ atom pair. The blue band shows 2D-polaron model prediction at $T=0$ (lower side) and $T/T_F=0.2$ (upper side). The solid line at $R/R_{TF}=1$ is the 2D-BCS prediction. The dashed curve is the Fermi liquid limit, $R/R_{TF}\simeq 1-0.5/\ln(2E_F/E_{b12})$. Note that the statistical error bars are comparable to the point size.

The 1D column density in a harmonic trap can be well fit by a function

$$n_{1D}(x)=n_{1D}(0)\left(1-\frac{x^2}{R^2}\right)^{\gamma}\Theta[R-|x|], \tag{4.20}$$

which is weakly dependent on a power law exponent γ. Here Θ is a Heaviside function that has a cutoff at $x=R$. The peak column density $n_{1D}(0)$, and the exponent n are determined from the fit. To find the peak column density we fit the data with a

parabola within 70% of the apparent Thomas-Fermi radius in order to avoid fitting the wings where relatively high noise is located. Normalizing the x-integral of the 1-D density distribution in eq. 4.20 to number of atoms per spin state N_1, determines the cloud radius

$$R = \frac{N_1}{n_{1D}(0)\sqrt{\pi}} \frac{\Gamma(\gamma + 3/2)}{\Gamma(\gamma + 1)}. \tag{4.21}$$

R is determined from the measured atom number per spin state N_1 and peak column density $n_{1D}(0)$.

Over the measured range of E_F/E_b, we see that the cloud radii are well below the ideal gas limit $R/R_{TF} = 1$ as shown in Fig. 4.6, where $R_{TF} = \sqrt{2E_F/m\omega_\perp^2}$ is the Thomas-Fermi radius. In contrast, 2D-BCS theory for a true 2D system predicts ideal gas Thomas-Fermi profiles [8, 72], $R/R_{TF} = 1$, in strong disagreement with the data.

Now we consider the 2D-polaron model prediction, shown as the the lower side of the blue band in Fig. 4.6. The cloud radii are determined from the local chemical potential $\mu = \partial f/\partial n$, which is determined from the approximate free energy density for the balanced gas [8, 87],

$$f = \frac{n}{2}\,\epsilon_F\,[1 + y(q)]. \tag{4.22}$$

For the spin-balanced $|1\rangle$-$|2\rangle$ mixture, using eq. 4.13, we obtain the cloud radii in units of the ideal gas Thomas-Fermi radius [8],

$$\frac{R}{R_{TF}} = \sqrt{\tilde{\mu}(0) + \frac{E_{b12}}{2E_F}}, \tag{4.23}$$

where $\tilde{\mu}(0)$ is the chemical potential at the center of the cloud in units of E_F, which is self-consistently determined [91]. Details are provided in Appendix A.

For large values of $\eta \equiv \ln(\sqrt{2E_F/E_{b12}}) \simeq \ln(k_F a_{2D})$, expansion of eq. 4.23 to lowest order in $1/\eta$ leads to $R/R_{TF} \simeq 1 - 1/(4\eta)$, the density profile of a Fermi

liquid [92] in a harmonic trap. Here, $k_F a$ is the Fermi momentum and a_{2D} is the 2D scattering length. We plot the Fermi liquid result as the dashed curve in Fig 4.6.

For these experiments, we are not able to cool the cloud as efficiently as in our previous studies in a CO_2 laser lattice, where we obtained $T/T_F < 0.2$. We estimate the effect of finite temperature by using ideal gas temperature scaling for the zero temperature radii. For $T/T_F = 0.2$, we obtain the upper side of the blue band in Fig. 4.6.

4.4 Conclusion

We have smoothly tuned the dimensionality of pancake-shaped ^{6}Li Fermi gas clouds from quasi-2D to 2D to measure radio-frequency spectra and cloud profiles in both regimes. In the quasi-2D case, where $E_F/h\nu_z \simeq 1$, with E_F the Fermi energy and $h\nu_z$ the harmonic oscillator energy in the tightly confined direction, we confirm that the radio-frequency spectra strongly disagree with 2D-mean field theory. Then we tune to the 2D regime, $E_F << h\nu_z$, where the measured radio frequency spectra are in very good agreement with 2D-mean field theory. Nevertheless, the measured cloud profiles also strongly disagree with 2D-mean field theory, confirming predictions that a beyond mean field approach is required throughout the 2D to quasi-2D crossover.

5

Pairing in a Bichromatic Lattice

In two dimensional quantum gases, atom-pairs can be formed on both the molecular BEC side of the Feshbach resonance as in three dimensions, and also in the BCS region. On the BCS side, stable pairs are caused by the confinement of the two dimensional geometry[5, 20], and are therefore called confinement-induced dimers. In this chapter, I will describe how to calculate the dimer binding energies first for a harmonically trapped gas. Next I will move on to an optical standing-wave lattice, and I will discuss the pairing energies for the bilayer gas in our bichromatic optical lattice. Finally I will describe our initial measurements of radio-frequency spectra to measure the pairing energy in a bichromatiac lattice.

5.1 Theory of Pairing in a Harmonic Potential

To determine the dimer pairing energy in a harmonic trap, we solve the Schrödinger equation for a harmonically-trapped two-atom system by using a time-dependent Green's function. Then we obtain the stationary Green's function. The stationary Green's function is used in a self-consistent integral equation to find the pair binding energy.

The Hamiltonian for two particles interacting via s-wave interaction in an external potential $V(\mathbf{r})$ is

$$\begin{aligned} H &= H_0 + V_s(\mathbf{r}), \\ H_0 &= \frac{\mathbf{p_1}^2}{2m} + \frac{\mathbf{p_2}^2}{2m} + V(\mathbf{r_1}) + V(\mathbf{r_2}), \end{aligned} \tag{5.1}$$

where $\mathbf{r_1}$ and $\mathbf{r_2}$ are the position of particles 1 and 2, $\mathbf{r} = \mathbf{r_1} - \mathbf{r_2}$ is the relative coordinate. The pseudo-potential form of the contact s-wave interaction is [16]

$$V_s(\mathbf{r}) = g\delta(\mathbf{r})\frac{\partial}{\partial r}\left[r...\right], \tag{5.2}$$

with $g \equiv \frac{4\pi\hbar^2 a}{m}$ and a the s-wave scattering length.

For the case of harmonic confinement, H_0 can be written as

$$H_0 = \frac{\mathbf{p}^2}{2\mu} + \frac{1}{2}\mu\sum_{i=x,y,z}\omega_i^2\mathbf{r}_i^2 + \frac{\mathbf{P}^2}{2M} + \frac{1}{2}M\sum_{i=x,y,z}\omega_i^2\mathbf{R}_i^2, \tag{5.3}$$

where $\mathbf{r} = \mathbf{r_1} - \mathbf{r_2}$ is the relative coordinate and $\mathbf{R} = \frac{\mathbf{r_1}+\mathbf{r_2}}{2}$ is the CM coordinate, $\mu = \frac{m}{2}$ is the reduced mass and $M = 2m$ is the total mass. For a simple harmonic oscillator external potential, the CM part and the relative motion part are separable. Since rf-excitation does not change the CM motion, when considering the pair binding problem, one can ignore the CM motion and only deal with the relative part of the Hamiltonian. Thus, H_0 can be reduced to just the relative motion part,

$$H_0 = \frac{\mathbf{p}^2}{2\mu} + \frac{1}{2}\mu\sum_{i=x,y,z}\omega_i^2\mathbf{r}_i^2. \tag{5.4}$$

The total Hamiltonian for the relative motion of the two-atom system inside a harmonic confinement with s-wave interaction is

$$H_{\mathbf{r}} = H_0 + V_s(\mathbf{r}). \tag{5.5}$$

We use a Green's function method to solve the Schrödinger equation for the bound state pairing energy. The time-dependent Schrödinger equation is

$$\left[H_0 - i\hbar\frac{\partial}{\partial t}\right]\psi(\mathbf{r},t) = -V_s(\mathbf{r})\psi(\mathbf{r},t). \tag{5.6}$$

To solve this, we use a time dependent Green's function

$$\left[H_0 - i\hbar\frac{\partial}{\partial t}\right]G(\mathbf{r},\mathbf{r}',t-t') = \delta(t-t')\delta(\mathbf{r}-\mathbf{r}'). \tag{5.7}$$

Then the solution to eq. 5.6 is

$$\psi(\mathbf{r},t) = \psi^{(0)}(\mathbf{r},t) - \int_{-\infty}^{\infty}dt'\int d^3\mathbf{r}'G(\mathbf{r},\mathbf{r}',t-t')V_s(\mathbf{r}')\psi(\mathbf{r}',t') \tag{5.8}$$

Where $\psi^{(0)}(\mathbf{r},t)$ is the homogeneous solution, i.e., $[H_0 - i\hbar\frac{\partial}{\partial t}]\psi^{(0)}(\mathbf{r},t) = 0$. The time dependent Green's function for a three dimensional harmonic trap, with trap frequencies $\omega_{i=x,y,z}$, is [82]

$$\begin{aligned} G(\mathbf{r},\mathbf{r}',t-t') &= \frac{i}{\hbar}\theta(t-t')\left[\left(\frac{\mu}{2\pi i\hbar}\right)^3\frac{\omega_x\omega_y\omega_z}{\sin\theta_x\sin\theta_y\sin\theta_z}\right]^{\frac{1}{2}} \\ &\cdot e^{\frac{i\mu\omega_x}{\hbar\sin\theta_x}\left[\cos\theta_x\frac{x^2+x'^2}{2}-xx'\right]} \\ &\cdot e^{\frac{i\mu\omega_y}{\hbar\sin\theta_y}[\cos\theta_y\frac{y^2+y'^2}{2}-yy']} \\ &\cdot e^{\frac{i\mu\omega_z}{\hbar\sin\theta_z}[\cos\theta_z\frac{z^2+z'^2}{2}-zz']}, \end{aligned} \tag{5.9}$$

where $\theta_i \equiv \omega_i(t-t')$.

For H_0, which has no explicit time dependence, the time-evolution of a state ψ follows

$$\psi(\mathbf{r},t) = e^{-\frac{iEt}{\hbar}}\psi_E(\mathbf{r}) \tag{5.10}$$

$$H_0\psi_E(\mathbf{r}) = E\psi_E(\mathbf{r}). \tag{5.11}$$

For a bound state, there is no input and $\psi_E^{(0)} = 0$, then eq. 5.8 becomes

$$e^{-\frac{i}{\hbar}Et}\psi_E(\mathbf{r}) = -\int_{-\infty}^{\infty} dt' \int d^3\mathbf{r}'\, G(\mathbf{r},\mathbf{r}',t,t')V_s(\mathbf{r}')e^{-\frac{i}{\hbar}Et'}\psi_E(\mathbf{r}'). \tag{5.12}$$

This can be expressed as

$$\psi_E(\mathbf{r}) = -\int d^3\mathbf{r}'\, G_E(\mathbf{r},\mathbf{r}')V_s(\mathbf{r}')\psi_E(\mathbf{r}'), \tag{5.13}$$

where the stationary Green's function $G_E(\mathbf{r},\mathbf{r}')$ is defined as

$$G_E(\mathbf{r},\mathbf{r}') \equiv \int_0^{\infty} d\tau e^{\frac{i}{\hbar}E\tau} G(\mathbf{r},\mathbf{r}',\tau). \tag{5.14}$$

Notice the integtal $\tau = t - t'$ starts from zero instead of $-\infty$ due to causality ($\Theta(t-t')$ in eq. 5.9).

Hitting both sides of eq. 5.13 with $\frac{\partial}{\partial r}[r...]|_{r\to 0}$, and inserting the form of the pseudo-potential in eq. 5.2 one obtains

$$\frac{\partial}{\partial r}[r\psi_E(\mathbf{r})]\ |_{r\to 0} = -\frac{4\pi\hbar^2 a}{m}\frac{\partial}{\partial r}[rG_E(\mathbf{r},0)]|_{r\to 0}\frac{\partial}{\partial r'}[r'\psi_E(\mathbf{r}')]\ |_{r'\to 0}\ . \tag{5.15}$$

The factors $\frac{\partial}{\partial r}[r\psi_E(\mathbf{r})]$ are identical for r and r'. Thus, the bound state energies E satisfy

$$1 = -\frac{4\pi\hbar^2 a}{m}\frac{\partial}{\partial r}[rG_E(\mathbf{r},0)]|_{r\to 0}. \tag{5.16}$$

The operator $\frac{\partial}{\partial r}r$ removes the $1/r$ divergence in $G_E(\mathbf{r},0)$ so that the right hand side of eq. 5.16 does not diverge. To solve eq. 5.16, we remove the $\frac{1}{r}$ divergence in $G_E(\mathbf{r},0)$. Let $G_0(\mathbf{r})$ be the part of $G_E(\mathbf{r},0)$ that is $\propto\frac{1}{r}$, i.e. $\frac{\partial}{\partial r}\left[rG_0(r)\right]|_{r\to 0} = 0$. Subtracting $G_0(\mathbf{r})$ from $G_E(\mathbf{r},0)$

$$1 = -\frac{4\pi\hbar^2 a}{m}\frac{\partial}{\partial r}[r(G_E(\mathbf{r},0) - G_0(\mathbf{r})\,)]|_{r\to 0}, \tag{5.17}$$

is effectively adding a term that is zero. Now $G_E(\mathbf{r},0) - G_0(\mathbf{r})$ is regular at $r = 0$, i.e. $r\frac{\partial}{\partial r}\left[G_{E_b}(\mathbf{r},0) - G_0(\mathbf{r})\right]|_{r\to 0} = 0$. Then one obtains

$$1 = -\frac{4\pi\hbar^2 a}{m}[G_{E_b}(\mathbf{r},0) - G_0(\mathbf{r})]|_{r\to 0}. \tag{5.18}$$

Once $G_0(\mathbf{r})$ is found, eq. 5.18 can be used to self consistently solve for energy E.

From eq. 5.9 and eq. 5.14, by taking $\mathbf{r}' \to 0$ and letting $u = i\omega_z\tau$ yeilds

$$G_E(\mathbf{r},0) = \frac{m}{4\pi\hbar^2}\frac{1}{l_z}\int_0^\infty \frac{du e^{-\epsilon_b u}}{\sqrt{4\pi}}\prod_j\left(\frac{2\beta_j u}{1-e^{-2\beta_j u}}\right)^{1/2} e^{-coth(\beta_j u)(x_j/2l_j)^2}. \tag{5.19}$$

Here l_i is the harmonic oscillator length scale, $l_i^2 = \frac{\hbar}{m\omega_i}$, and the dimensionless ratio of trap frequencies is $\beta_i = \frac{\omega_i}{\omega_z}$, where $i = x, y, z$. Define binding energy $E_b = \epsilon\hbar\omega_z > 0$, assumed to be positive, relative to the ground state energy E_0. The ground state energy of a harmonic oscillator in three directions is $E_0 = \frac{\hbar\omega_x}{2} + \frac{\hbar\omega_y}{2} + \frac{\hbar\omega_z}{2}$. The eigenenergy E of a stable paired state below the ground state is $E = E_0 - E_b$.

In eq. 5.19, for large E_b where $\epsilon_b \gg 1$, only terms with small u can survive. So, we can approximately write $\coth(u) \to \frac{1}{u}$, $\frac{2\beta_i}{1-e^{-2u\beta_i}} \to \frac{1}{u}$,

$$\begin{aligned} G_E(\mathbf{r}) &= \frac{1}{4\pi\hbar\omega_z}\frac{1}{l_z^3}\int_0^\infty \frac{du}{\sqrt{4\pi u^3}} e^{-\epsilon_b u - \frac{r^2}{4ul_z^2}} \\ &= \frac{m}{4\pi\hbar^2 r} e^{-r\sqrt{\epsilon_b/l_z^2}}. \end{aligned} \tag{5.20}$$

In order to obtain the form of $G_0(\mathbf{r})$, we take the limit of $\epsilon_b \to 0$ and $r \to 0$ in eq. 5.20,

$$G_0(\mathbf{r}) = \frac{m}{4\pi\hbar^2 l_z}\int_0^\infty \frac{du}{\sqrt{4\pi u^3}} = \frac{m}{4\pi\hbar^2\mathbf{r}}. \tag{5.21}$$

We can then use in eq. 5.19 and eq. 5.21 in eq. 5.18 to get a self-consistent integral equation,

$$\frac{l_z}{a} = \int_0^\infty \frac{du}{\sqrt{4\pi u^3}}\left[1 - \prod_j\left(\frac{2\beta_j u}{1-e^{-2\beta_j u}}\right)^{1/2} e^{-\epsilon_b u}\right]. \tag{5.22}$$

This equation can be used to find the bound state pairing energy $E_b = \epsilon_b \hbar\omega_z$.

We can test the large E_b limit of eq. 5.18. Inserting eq. 5.20 for $G_E(\mathbf{r})$ and eq. 5.21 for $G_0(\mathbf{r})$ into eq. 5.18, one arrives at the following expression,

$$\begin{aligned} 1 &= -\frac{4\pi\hbar^2 a}{m}\left[\frac{m}{4\pi\hbar^2 r}e^{-r\sqrt{\epsilon_b/l_z^2}} - \frac{m}{4\pi\hbar^2 r}\right]|_{r\to 0} \\ &= a\sqrt{\frac{\epsilon_b}{l_z^2}}. \end{aligned} \tag{5.23}$$

For large binding energy, using $l_z^2 = \frac{\hbar}{m\omega_z}$ we have

$$E_b = \epsilon_b \hbar w_z = \frac{\hbar^2}{ma^2}. \tag{5.24}$$

The binding energy corresponds to that of a tight dimer $a \ll l_z$, independent of the trap parameters.

By letting $t = 2u$ in eq. 5.22 and for cylindrical symmetry $\omega_x = \omega_y = \omega_\perp$, $\beta_\perp \equiv \frac{\omega_\perp}{\omega_z} = \frac{1}{N}$, where $N \in$ *integers* and $N \geqslant 1$, one can make use of a trick [93] to integrate eq. 5.22 exactly.

$$\sum_{n=0}^{N-1}\left(e^{-\frac{1}{N}t}\right)^n = \frac{1-e^{-t}}{1-e^{-\frac{1}{N}t}}, \tag{5.25}$$

and there exists a closed form for the following integral when $x > 0$

$$\int_0^\infty dt\left\{\frac{e^{-xt}}{(1-e^{-t})^{3/2}} - \frac{1}{t^{3/2}}\right\} = \frac{-2\sqrt{\pi}\,\Gamma(x)}{\Gamma(x-\frac{1}{2})},\ x > 0. \tag{5.26}$$

Thus the integral on the right hand side of eq. 5.22 becomes

$$\int_0^\infty \frac{du}{\sqrt{4\pi u^3}} \left\{ 1 - \left(\frac{2u}{1-e^{-2u}} \right)^{\frac{1}{2}} \frac{2\beta_\perp u}{1-e^{-2\beta_\perp u}} e^{-\epsilon_b u} \right\}$$

$$= -\frac{1}{\sqrt{2\pi}} \frac{1}{N} \sum_{n=0}^{N-1} \int_0^\infty dt \left\{ \frac{e^{-\left(\frac{\epsilon_b}{2}+\frac{n}{N}\right)t}}{(1-e^{-t})^{3/2}} - \frac{1}{t^{3/2}} \right\}$$

$$= \frac{\sqrt{2}}{N} \sum_0^{N-1} \frac{\Gamma(\frac{\epsilon_b}{2}+\frac{n}{N})}{\Gamma(\frac{\epsilon_b}{2}-\frac{1}{2}+\frac{n}{N})} \tag{5.27}$$

The analytical expression for determining the pairing energy is then

$$\frac{l_z}{a} = \frac{\sqrt{2}}{N} \sum_0^{N-1} \frac{\Gamma(\frac{\epsilon_b}{2}+\frac{n}{N})}{\Gamma(\frac{\epsilon_b}{2}-\frac{1}{2}+\frac{n}{N})}. \tag{5.28}$$

Recall the definition of binding energy $E_b \equiv \epsilon_b \hbar\omega_z$, assuming $E_b > 0$. We have $E = E_0 - E_b$, where $E_0 = \frac{\hbar\omega_x}{2} + \frac{\hbar\omega_y}{2} + \frac{\hbar\omega_z}{2}$ is the ground state energy of harmonic oscillators in three directions. We plot E_b in units of $\hbar\omega_z$ for various trap geometries using the above equation. Plotted in Fig 5.1 are results for a spherically symmetric trap($w_\perp/w_z = 1$), cylindrically symmetric trap($w_\perp/w_z = 1/5$), and the 2D gas limit ($w_\perp/w_z = 1/1000$) where the radial confinement almost does not exist. For repulsive interaction $a > 0$, the energy levels are shifted upward while for attractive interaction $a < 0$, the energy levels are shifted downwards. Apart from the usual bound state which has $E < E_0$ corresponding to states that has energy lower than the ground harmonic oscillator state, there are also many other bound states at $E > E_0$ coming from the radial confinement. The red dashed lines correspond to radial harmonic oscillator states of equally spaced $2\hbar\omega_\perp$ in Fig 5.1(a) and (b). In Fig 5.1(c) the red dashed lines correspond to axial harmonic oscillator states that are equally spaced by $2\hbar\omega_z$. For the noninteracting limit where $a \to 0$, one retrieves the harmonic oscillator solutions. It is interesting to examine the 2D limiting case, in which the solutions show spikes around every $2\hbar w_z$ suggesting some kind of resonance. The unexpected

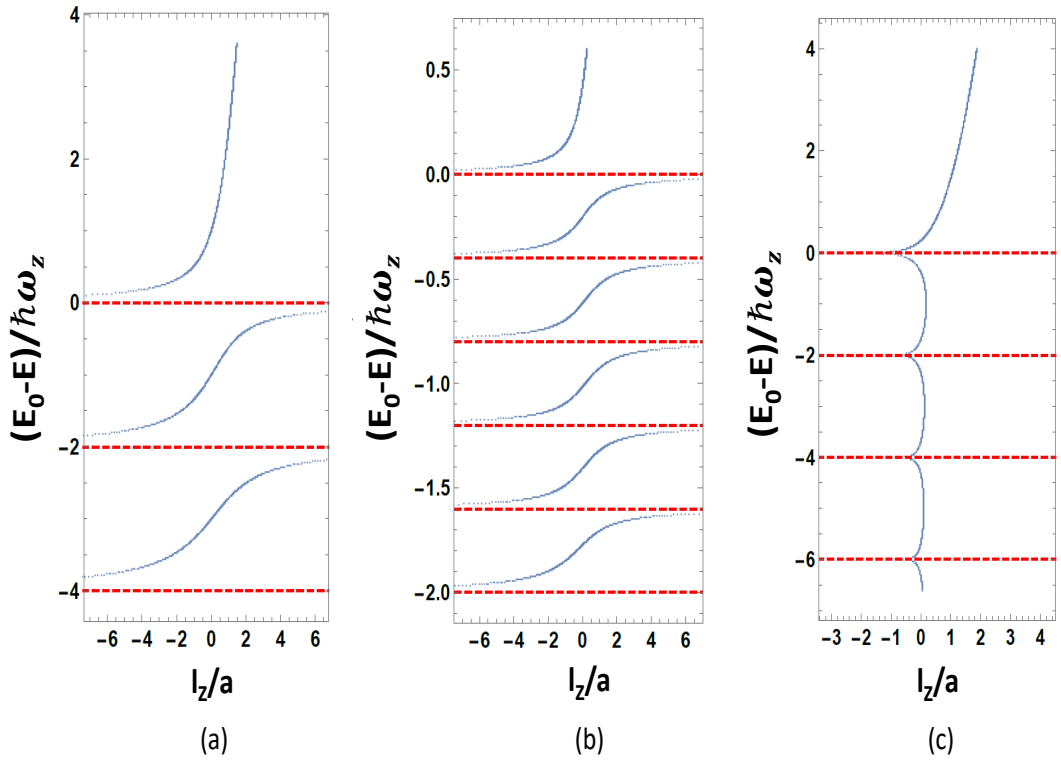

FIGURE 5.1: Plot pairing energies $E_b = E_0 - E$ referenced to two particle ground harmonic oscillator states E_0 in 3D. The relative motion for two atoms interacting via s-wave pseudopotential and confined in a cylindrically symmetric harmonic trap with (a)$w_\perp/w_z = 1$, (b) $w_\perp/w_z = 1/5$ and (c) $w_\perp/w_z = 1/1000$ respectively. The energies in units of $\hbar\omega_z$ are plotted as a function of the harmonic oscillator length scale $l_z = \sqrt{\frac{\hbar}{mw_z}}$ over the s-wave scattering length a. The red dashed lines correspond to radial states of equally spaced $2\hbar\omega_\perp$ in (a) and (b). In (c) the red dashed lines correspond to every $2\hbar\omega_z$.

quasibound states, which appear at positive energies, are extremely broad in energy and therefore have never been observed experimentally [94, 95].

5.2 Theory of Pairing in a Double Well Potential

As described in the last section, for a simple harmonic oscillator external potential, the CM part and the relative motion part are separable. Since rf-excitation does not change the CM motion, when considering the pair binding problem, one can ignore the CM motion and only deal with the relative part of the Hamiltonian. However

for the case of atoms are in an optical lattice, the CM and relative motion are not decoupled.

Consider first a one dimensional lattice $V(z) = V\cos^2(kz)$, for two atoms at positions z_1 and z_2. With $Z = \left(\frac{z_1+z_2}{2}\right)$ for the CM and $z = z_1 - z_2$ for the relative position,

$$V(z_1, z_2) = V\cos^2\left(Z + \frac{z}{2}\right) + V\cos^2\left(Z - \frac{z}{2}\right) = V(z, Z). \tag{5.29}$$

The form of the potential implies that the CM and relative motion are in general coupled. The Hamiltonian, with the interaction term is

$$H = \frac{\mathbf{p}^2}{2\mu} + \frac{\mathbf{P}_x^2}{2M} + \frac{\mathbf{P}_y^2}{2M} + \frac{\mathbf{P}_z^2}{2M} + V(z, Z) + g\delta(\mathbf{r})\frac{\partial}{\partial r}[r...] \tag{5.30}$$

One can see that only the x and y CM momenta are separable and can therefore be factored out. Rewriting the Hamiltonian into perturbed and unperturbed parts yields

$$\begin{aligned} H &= H_0(\mathbf{r}, Z) + g\delta(\mathbf{r})\frac{\partial}{\partial r}[r...] \\ H_0(\mathbf{r}, Z) &= \frac{\mathbf{p}^2}{2\mu} + \frac{\mathbf{P}_z^2}{2M} + V(z, Z) \\ &= \frac{\mathbf{p}_\perp^2}{2\mu} + \frac{\mathbf{p}_{1,z}}{2m} + V(z_1) + \frac{\mathbf{p}_{2,z}}{2m} + V(z_2), \end{aligned} \tag{5.31}$$

where $\mathbf{p}_\perp$ is the relative momentum in the transverse x, y direction. $\mathbf{p}_{1,z}$ and $\mathbf{p}_{2,z}$ are single particle momenta.

$$(H_0(\mathbf{r}, Z) - E)\,\Psi_E^{(0)}(\mathbf{r}, Z) = 0 \tag{5.32}$$

$$(H_0(\mathbf{r}, Z) - E)\,\Psi_E(\mathbf{r}, Z) = -g\delta(\mathbf{r})\frac{\partial}{\partial r}[r\Psi_E(\mathbf{r}, Z)] \tag{5.33}$$

By definition, the solution of the following equation is the Green's function,

$$(H_0(\mathbf{r}, Z) - E)\,G_E(\mathbf{r}, Z, \mathbf{r}', Z') = -\delta(\mathbf{r} - \mathbf{r}')\delta(Z - Z'). \tag{5.34}$$

Then,

$$\Psi_E(\mathbf{r}, Z) = \Psi_E^{(0)}(\mathbf{r}, Z) + g \int dZ' \int d^3\mathbf{r}' G_E(\mathbf{r}, Z, \mathbf{r}', Z')\delta(\mathbf{r}')\frac{\partial}{\partial r'}\left[r'\Psi_E(\mathbf{r}', Z')\right]_{r'\to 0} \tag{5.35}$$

For a bound state $\Psi_E^{(0)}$ has to vanish. Applying $\frac{1}{g}\frac{\partial}{\partial r}\left[r...\right]|_{\mathbf{r}\to 0}$ on both sides and defining $\mathcal{U}_E(\mathbf{r}, Z) \equiv r\Psi_E(\mathbf{r}, Z)$, then

$$\frac{1}{g}\,\mathcal{U}'_E(0, Z) = \int dZ' \frac{\partial}{\partial r}\left[rG_E((\mathbf{r}, Z, 0, Z')\right]|_{\mathbf{r}\to 0}\,\mathcal{U}'_E(0, Z'). \tag{5.36}$$

Unlike eq. 5.15, the $\mathcal{U}'_E(0, Z')$ on the right hand side is inside the integral of Z', and does not simply cancel out as in the harmonic trap case. After integrating over Z', the above equation now only depends on Z, which is center of mass position along the z-axis. We define $\mathcal{U}'_E(0, Z) \equiv f_E(Z)$, then

$$\frac{1}{g} f_E(Z) = \int_{-\infty}^{\infty} dZ' \mathcal{K}_E(Z, Z') f_E(Z'), \tag{5.37}$$

where the kernel is defined as

$$\mathcal{K}_E(Z, Z') \equiv \frac{\partial}{\partial r}\left[rG_E((\mathbf{r}, Z, 0, Z')\right]|_{\mathbf{r}\to 0}\ . \tag{5.38}$$

Since $V(z, Z)$ is periodic in Z, the CM quasi-momentum $Q = q_1 + q_2$ is conserved, and $f_E(Z)$ has the form of a Bloch function similar to eq. 2.19, which is

$$f_E(Z) = \sum_G B_G(Q)\frac{e^{i(G+Q)Z}}{\sqrt{Nd}}, \tag{5.39}$$

where d is the lattice spacing and N is the number of sites. We use eq. 5.39 in eq. 5.37 and apply $\int dZ e^{-i(G+Q)Z}$ on both sides. Since the basis is orthomornal and

complete, one obtains

$$\frac{d}{a}B_G(Q) = \frac{4\pi\hbar^2 d}{m}\sum_{G'}\int dZ e^{-i(G+Q)Z}\int dZ' \mathcal{K}_E(Z,Z')B_{G'}(Q')e^{i(G'+Q')Z'}$$

$$= \sum_{G'}\frac{4\pi\hbar^2 d}{m}\langle G+Q|\mathcal{K}_E|G'+Q'\rangle B_{G'}(Q'). \tag{5.40}$$

Solving the above matrix equation, one can obtain d/a, the lattice spacing over the s-wave scattering length, as a function of the energy E.

The trick we use regularize the kernel is to subtract two Green's functions to remove the singularity at $r \to 0$, similar to the harmonic oscillator case. We subtract the Green's function for zero lattice depth $s_1 \to 0$ in eq. 5.38,

$$\mathcal{K}^{s2}_{E2}(Z,Z') = \left(G^{s2}_{E2}(Z,Z') - G^{s1\to 0}_{E1}(Z,Z')\right) + \mathcal{K}^{s1\to 0}_{E1}(Z,Z'), \tag{5.41}$$

where $(G^{s2}_{E2}(Z,Z') - G^{s1\to 0}_{E1}(Z,Z'))$ is now regular at $r \to 0$. $s1$ and $s2$ denotes the lattice depth in units of E_R, and in general can be any value. For our convenience, we will take $s1 \to 0$, which recovers the free particle case.

Let's first try to compute the second part, the free particle kernel $\mathcal{K}^{s1\to 0}_{E1}(Z,Z')$ as defined in eq. 5.38, by computing first the free particle's Green's function.

$$\left(-\frac{\hbar^2}{2\mu}\frac{\partial^2}{\partial^2\mathbf{r}^2} - \frac{\hbar^2}{2M}\frac{\partial^2}{\partial Z^2} - E_1\right) G^0_{E1}(\mathbf{r}-\mathbf{r}', Z-Z') =$$

$$-\delta(\mathbf{r}-\mathbf{r}')\delta(Z-Z'). \tag{5.42}$$

The superscript zero in G^0_{E1} denotes a lattice depth of zero. The Fourier transform of the delta function is

$$\delta(\mathbf{r}-\mathbf{r}')\delta(Z-Z') = \int\frac{d^3\mathbf{k}}{(2\pi)^3}\int\frac{dq}{2\pi}e^{i\mathbf{k}(\mathbf{r}-\mathbf{r}')+iq(Z-Z')}. \tag{5.43}$$

The free particle's Green's function G^0_{E1} is thus

$$G^0_{E1}(\mathbf{r}-\mathbf{r}', Z-Z') = \int\frac{d^3\mathbf{k}}{(2\pi)^3}\int\frac{dq}{2\pi}\,\frac{e^{i\mathbf{k}(\mathbf{r}-\mathbf{r}')+iq(Z-Z')}}{(E_1+i\epsilon) - \frac{\hbar^2\mathbf{k}^2}{2\mu} - \frac{\hbar^2 q^2}{2M}}, \tag{5.44}$$

where $\epsilon \to 0^+$. Requiring the binding energy $E_b > 0$ for a bound state such that $E_1 = \frac{\hbar^2 q^2}{2M} - E_b$, yields

$$G^0_{E1}(\mathbf{r}-\mathbf{r}', Z-Z') = \\ -\frac{m}{4\pi\hbar^2}\frac{1}{\mathbf{r}}\int_{-\infty}^{\infty}\frac{dq}{2\pi}e^{iq(Z-Z')}\,\Theta\left[\frac{q^2}{4}-\frac{mE_1}{\hbar^2}\right]e^{-\sqrt{\frac{q^2}{4}-\frac{mE_1}{\hbar^2}}\,(\mathbf{r}-\mathbf{r}')} \tag{5.45}$$

The free particle kernel $\mathcal{K}^0_{E1}$, using definition in eq. 5.38 is then

$$\mathcal{K}^0_{E1}(Z,Z') = \frac{m}{4\pi\hbar^2}\int_{-\infty}^{\infty}\frac{dq}{2\pi}e^{iq(Z-Z')}\,\Theta\left[\frac{q^2}{4}-\frac{mE_1}{\hbar^2}\right]\sqrt{\frac{q^2}{4}-\frac{mE_1}{\hbar^2}}\,. \tag{5.46}$$

Using eq. 5.46 in eq. 5.37, we find the binding energies for a zero lattice depth. The eigenfunction of a free particle having center of mass momentum P is just a plane wave $f^0_E(Z) = \frac{e^{iPZ}}{\sqrt{2\pi}}$. Using this in eq. 5.37, with eq. 5.46, then we find

$$E(P) \;=\; \frac{\hbar^2 P^2}{4m} - \frac{\hbar^2}{ma^2}\,. \tag{5.47}$$

From above expression, we see that the total energy of the dimer is the kinetic energy of the center of mass minus the dimer binding energy in free space, as it should be. The binding energy $E_b = \frac{\hbar^2}{ma^2} > 0$ is independent of P.

In order to numerically calculate the binding inside the lattice, we need to rewrite the integral in eq. 5.46 as a discrete sum, $\int \frac{Nd}{2\pi}dq = \sum_{G_1,q_1}$ with $q \to G_1 + q_1$,

$$\mathcal{K}^0_{E1}(Z,Z') = \\ \frac{m}{4\pi\hbar^2}\sum_{G_1,q_1}\frac{e^{i(G_1+q_1)(Z-Z')}}{Nd}\sqrt{\frac{\hbar^2}{4m}\frac{(G_1+q_1)^2}{E_R}-\frac{E_1}{E_R}}\,\sqrt{\frac{mE_R}{\hbar^2}}, \tag{5.48}$$

where the lattice recoil energy $E_R = \frac{\hbar^2}{2m}\left(\frac{\pi}{d}\right)^2$ and $d = \frac{\lambda}{2\sin\left(\frac{\theta}{2}\right)}$ is the lattice spacing. Rewriting eq. 5.48 in normalized units, one obtains

$$\mathcal{K}^0_{\widetilde{E1}}(Z,Z') = \frac{m}{4\pi\hbar^2}\frac{1}{d}\frac{\pi}{\sqrt{2}}\sum_{\widetilde{G_1},\widetilde{q_1}}\frac{e^{i(G_1+q_1)(Z-Z')}}{Nd}\sqrt{\frac{\left(\widetilde{G_1}+\widetilde{q_1}\right)^2}{2}-\widetilde{E_1}}\,, \tag{5.49}$$

where $\widetilde{E_1} = \frac{E_1}{E_R}$, $\widetilde{G_1} \equiv \frac{G_1}{k}$ and $\widetilde{q_1} = \frac{q_1}{k}$. With eq. 5.49, the matrix element of the free particle kernel $\langle G+Q|\mathcal{K}^{S1\to 0}_{E1}(Z,Z')|G'+Q'\rangle$ in eq. 5.40 is,

$$\begin{aligned}
&\langle G+Q|\mathcal{K}^{0}_{\widetilde{E1}}(Z,Z')|G'+Q'\rangle \\
&= \int_0^{Nd} \frac{dZ}{\sqrt{Nd}} e^{-i(G+Q)Z} \int_0^{Nd} \frac{dZ'}{\sqrt{Nd}} e^{i(G'+Q')Z'} \mathcal{K}^{0}_{\widetilde{E1}}(Z,Z') \\
&= \frac{m}{4\pi\hbar^2}\frac{1}{d}\frac{\pi}{\sqrt{2}}\delta_{Q,q_1}\delta_{Q',q_1}\delta_{G,G_1}\delta_{G',G_1}\sqrt{\frac{\left(\widetilde{G_1}+\widetilde{q_1}\right)^2}{2}-\widetilde{E_1}} \\
&= \frac{m}{4\pi\hbar^2}\frac{1}{d}\frac{\pi}{\sqrt{2}}\delta_{G,G'}\delta_{Q,Q'}\sqrt{\frac{\left(\widetilde{G}+\widetilde{Q}\right)^2}{2}-\widetilde{E_1}}
\end{aligned} \tag{5.50}$$

The delta functions are obtained using the same trick as in eq. 2.23.

For the discrete sum form of Green's function inside a lattice, we make use of the completeness relation of the single atom Bloch functions,

$$\sum_{\alpha,q} \Psi^{\alpha}_{q}(z)\Psi^{*\alpha}_{q}(z') = \delta(z-z'). \tag{5.51}$$

Starting from the definition of the Green's function in eq. 5.34,

$$\begin{aligned}
&\left(H_0(\mathbf{r}_\perp,z_1,z_2)-E\right)G_E(\mathbf{r}_\perp,\mathbf{r}'_\perp;z_1,z'_1;z_2,z'_2) = \\
&\qquad -\delta(\mathbf{r}_\perp-\mathbf{r}'_\perp)\delta(z_1-z'_1)\delta(z_2-z'_2),
\end{aligned} \tag{5.52}$$

where $\mathbf{r}_\perp$ is the relative x and y coordinate, and z_1, z_2 specifies the z coordinate of each particle. Thus

$$\begin{aligned}
&G_E(\mathbf{r}_\perp,\mathbf{r}'_\perp;z_1,z'_1;z_2,z'_2) = \\
&\sum_{\alpha_1,q_1,\alpha_2,q_2}\int_0^\infty \frac{d^2\mathbf{k}_\perp}{(2\pi)^2} e^{i\mathbf{k}_\perp(\mathbf{r}_\perp-\mathbf{r}'_\perp)} \frac{\Psi^{\alpha_1}_{q_1}(z_1)\Psi^{*\alpha_1}_{q_1}(z'_1)\Psi^{\alpha_2}_{q_2}(z_2)\Psi^{*\alpha_2}_{q_2}(z'_2)}{(E+i\epsilon)-\frac{\hbar^2{\mathbf{k}_\perp}^2}{m}-\epsilon_{\alpha_1}(q_1)-\epsilon_{\alpha_2}(q_2)}.
\end{aligned} \tag{5.53}$$

The definition of the z direction center of mass is $Z = \frac{z_1+z_2}{2}$ and relative coordinate is $z = \frac{z_1-z_2}{2}$, so that $z_1 = Z+\frac{z}{2}$, $z_2 = Z-\frac{z}{2}$. By taking $\mathbf{r}$, $\mathbf{r}' \to 0$, $z_1 = z_2 = Z$

and $z_1' = z_2' = Z'$. The discrete form of $G_E(\mathbf{r} \to 0, Z, \mathbf{r}' \to 0, Z') \equiv G_E(Z, Z')$ in the Bloch state basis is then

$$G_E(Z,Z') = \sum_{\alpha_1,q_1,\alpha_2,q_2} \int_0^\infty \frac{d^2\mathbf{k}_\perp}{(2\pi)^2} \frac{\Psi_{q_1}^{\alpha_1}(Z)\Psi^{*\alpha_1}_{q_1}(Z')\Psi_{q_2}^{\alpha_2}(Z)\Psi^{*\alpha_2}_{q_2}(Z')}{(E+i\epsilon) - \frac{\hbar^2 {\mathbf{k}_\perp}^2}{m} - \epsilon_{\alpha_1}(q_1) - \epsilon_{\alpha_2}(q_2)}. \tag{5.54}$$

In eq. 5.54, the integral over $\mathbf{k}_\perp$ yields a logarithm. In eq. 5.41 the upper limit $\mathbf{k}_\perp \to \infty$ in $(G_{E2}^{s2}(Z,Z') - G_{E1}^{s1\to 0}(Z,Z'))$ vanishes, and the lower limit yields a principal part for $\epsilon \to 0^+$. After normalizing all energies to E_R, i.e. $\widetilde{E} = E/E_R$, the first terms in eq. 5.41 can be written as,

$$G_{\widetilde{E}}(Z,Z') - G^0_{\widetilde{E1}}(Z,Z') = \frac{m}{4\pi\hbar^2} \sum_{\alpha_1,q_1,\alpha_2,q_2}$$

$$\Big\{ Re\left(\ln\left[\widetilde{\epsilon}_{\alpha_1}(q_1) + \widetilde{\epsilon}_{\alpha_2}(q_2) - \widetilde{E}\right]\right) \Psi_{q_1}^{\alpha_1}(Z)\Psi^{*\alpha_1}_{q_1}(Z')\Psi_{q_2}^{\alpha_2}(Z)\Psi^{*\alpha_2}_{q_2}(Z')$$

$$- Re\left(\ln\left[\widetilde{\epsilon^0}_{\alpha_1}(q_1) + \widetilde{\epsilon^0}_{\alpha_2}(q_2) - \widetilde{E_1}\right]\right) \Psi_{0\,q_1}^{\alpha_1}(Z)\Psi^{*\alpha_1}_{0\,q_1}(Z')\Psi_{0\,q_2}^{\alpha_2}(Z)\Psi^{*\alpha_2}_{0\,q_2}(Z')\Big\}, \tag{5.55}$$

where the zeros denote the zero lattice depth solutions.

Substituting $\Psi_q^\alpha(Z) = \sum_G C_G^\alpha \frac{e^{i(G+q)Z}}{\sqrt{Nd}}$, the matrix element in eq. 5.40 is

$$\langle G+Q|G_{\widetilde{E}}(Z,Z') - G^0_{\widetilde{E1}}(Z,Z')|G'+Q'\rangle =$$

$$\frac{m}{4\pi\hbar^2}\frac{1}{Nd} \sum_{\alpha_1,q_1,\alpha_2,q_2} \Big\{ Re\left(\ln\left[\widetilde{\epsilon}_{\alpha_1}(q_1) + \widetilde{\epsilon}_{\alpha_2}(q_2) - \widetilde{E}\right]\right)$$

$$\sum_{G_1,G_1',G_2,G_2'} C_{G_1}^{\alpha_1}(q_1) C_{G_1'}^{\alpha_1 *}(q_1) C_{G_2}^{\alpha_2}(q_2) C_{G_2'}^{\alpha_2 *}(q_2)$$

$$\int_0^{Nd} dZ \frac{1}{Nd} e^{i[G_1+q_1+G_2+q_2-G-Q]Z}$$

$$\int_0^{Nd} dZ' \frac{1}{Nd} e^{i[-G_1'-q_1-G_2'-q_2+G'+Q']Z'}$$

$$- Re\left(\ln\left[\widetilde{\epsilon^0}_{\alpha_1}(q_1) + \widetilde{\epsilon^0}_{\alpha_2}(q_2) - \widetilde{E_1}\right]\right) .....\Big\}, \tag{5.56}$$

with the zero lattice depth part having the exact same form as the first part with zero lattice solutions $C^{0\alpha}_G$ and $\widetilde{\epsilon^0}_\alpha$. Using the same trick as in eq. 2.23, the integrals over

Z and Z' in eq. 5.56 give δ_{Q,q_1+q_2}, δ_{Q',q_1+q_2}, δ_{G,G_1+G_2}, and $\delta_{G',G'_1+G'_2}$. Then eq. 5.56 becomes

$$\begin{aligned}
&\langle G+Q|G_{\widetilde{E}}(Z,Z') - G^0_{\widetilde{E1}}(Z,Z')|G'+Q'\rangle = \\
&\frac{m}{4\pi\hbar^2 Nd}\sum_{q_1}\sum_{\alpha_1,\alpha_2}\Big\{Re\left(\ln\left[\widetilde{\epsilon}_{\alpha_1}(q_1)+\widetilde{\epsilon}_{\alpha_2}(Q-q_1)-\widetilde{E}\right]\right) \\
&\sum_{G_1,G'_1} C^{\alpha_1}_{G_1}(q_1)C^{\alpha_1 *}_{G'_1}(q_1)C^{\alpha_2}_{G-G_1}(Q-q_1)C^{\alpha_2 *}_{G'-G'_1}(Q-q_1) \\
&- Re\left(\ln\left[\widetilde{\epsilon^0}_{\alpha_1}(q_1)+\widetilde{\epsilon^0}_{\alpha_2}(Q-q_1)-\widetilde{E_1}\right]\right) \\
&\sum_{G_1,G'_1} C^{0\alpha_1}_{\ G_1}(q_1)C^{0\alpha_1 *}_{\ G'_1}(q_1)C^{0\alpha_2}_{\ G-G_1}(Q-q_1)C^{0\alpha_2 *}_{\ G'-G'_1}(Q-q_1)\Big\}. \qquad (5.57)
\end{aligned}$$

For higher excited bands, $\widetilde{\epsilon}_{\alpha_1}(q_1) \simeq \widetilde{\epsilon^0}_{\alpha_1}(q_1)$, and the log terms becomes identical. Then, the sums reduce to Kronecher deltas,

$$\begin{aligned}
\sum_{\alpha_1} C^{\alpha_1}_{G_1}(q_1)C^{\alpha_1 *}_{G'_1}(q_1) &= \delta_{G_1,G'_1}, \\
\sum_{\alpha_2} C^{\alpha_2}_{G-G_1}(q_1)C^{\alpha_2 *}_{G'-G'_1}(q_1) &= \delta_{G-G_1,G'-G'_1}, \qquad (5.58)
\end{aligned}$$

and the quantity in curly brackets in eq. 5.57 goes to zero. Hence, the sum is convergent.

The zero lattice depth term can be simplified. Since the zero lattice depth solution is just parabolically dispersive like a free particle, we know all the $C^{0\alpha}_{\ G}$ and $\epsilon^0_\alpha(q)$,

i.e.,

$$\alpha = 1,\ {C^0}_{G_1}^{\alpha=1} = \delta_{G_1,0}\ ;$$

$${\epsilon^0}_{\alpha=1}(q_1) = \frac{\hbar^2}{2m} q_1^2$$

$$\alpha = 2,\ {C^0}_{G_1}^{\alpha=2}(q_1) = \delta_{G_1,-G_0}\Theta[q_1] + \delta_{G_1,G_0}\Theta[-q_1]\ ;$$

$${\epsilon^0}_{\alpha=2}(q_1) = \frac{\hbar^2}{2m}(G_0 - q_1)^2\Theta[q_1] + \frac{\hbar^2}{2m}(G_0 + q_1)^2\Theta[-q_1]$$

$$\alpha = 3,\ {C^0}_{G_1}^{\alpha=3}(q_1) = \delta_{G_1,G_0}\Theta[q_1] + \delta_{G_1,-G_0}\Theta[-q_1]\ ;$$

$${\epsilon^0}_{\alpha=3}(q_1) = \frac{\hbar^2}{2m}(G_0 + q_1)^2\Theta[q_1] + \frac{\hbar^2}{2m}(G_0 - q_1)^2\Theta[-q_1], \tag{5.59}$$

similarly for all the higher bands $\alpha = 4, 5.....$ These relations require $G' = G$ and $G'_1 = G_1$ for each α. Therefore, we can write

$${\widetilde{\epsilon^0}}_{\alpha_1}(q_1) = (\widetilde{G_1} + \widetilde{q_1})^2$$

$${\widetilde{\epsilon^0}}_{\alpha_2}(Q - q_1) = (\widetilde{G_2} + \widetilde{Q} - \widetilde{q_1})^2 = (\widetilde{G} - \widetilde{G_1} + \widetilde{Q} - \widetilde{q_1})^2, \tag{5.60}$$

where in eq. 5.56 we have $G_2 = G - G_1 = G'_2$. The analytic expression of the zero lattice Green's function sum in the second half of eq. 5.56 then can be written as

$$\langle G + Q|G^0_{\widetilde{E1}}(Z, Z')|G' + Q'\rangle =$$

$$\frac{m}{4\pi\hbar^2}\frac{1}{Nd}\sum_{q_1,G_1}\ln\left[\left(\widetilde{G_1} + \widetilde{q_1}\right)^2 + \left(\widetilde{G} + \widetilde{Q} - \widetilde{G_1} - \widetilde{q_1}\right)^2 - \widetilde{E_1}\right], \tag{5.61}$$

where $\widetilde{q_1} = \frac{q_1}{k} = \frac{2m_1}{N}$; $\frac{-N}{2} \leqslant m_1 \leqslant \frac{N}{2} - 1$ with $N \in even$, and $\widetilde{G_1} = \frac{G_1}{k} = \frac{nG_0}{k} = 0, \pm 2, \pm 4...$ since $G_0 = \frac{2\pi}{d}$ and $k = \frac{\pi}{d}$.

Note that for a $4M + 1$ band model where $1 \leqslant G_1, G_2 \leqslant 4M + 1$, due to the symmetry of the Bloch bands, we can shift $G \to G - (2M + 1)$, $G_1 \to G_1 - (2M + 1)$ and $G_2 \to G_2 - (2M + 1)$ to symmetrize the matrix in G, G'. Since $G = G_1 + G_2$, the range of G_1 in the sum has to be refined in order not to exceed the matrix dimension.

Therefore $G_1 \leqslant \min[G+2M, 4M+1]$ sets the upper limit, while $G_1 \geqslant \max[1, G-2M]$ sets the lower limit of G_1. Rewriting eq. 5.57 after shifting the indices as described above, one obtains

$$\langle G+Q|G^0_{\widetilde{E1}}(Z,Z')|G'+Q'\rangle = \frac{m}{4\pi\hbar^2}\frac{1}{Nd}\sum_{m_1=-\frac{N}{2}}^{\frac{N}{2}-1}\sum_{G_1=max[1,G-2M]}^{min[G+2M,4M+1]}$$

$$\ln\left[\left[2\left(G_1-(2M+1)+\frac{2m_1}{N}\right)\right]^2+\left[2(G-G_1)+\widetilde{Q}-\frac{2m_1}{N}\right]^2-\widetilde{E_1}\right]. \quad (5.62)$$

We shift $q_1 \to q_1 + \frac{Q}{2}$, such that the terms are identical for $q_1 \to -q_1$, in order to enhance the computational speed by a factor of two when summing over q_1. With eq. 5.50, eq. 5.57, eq. 5.62, the matrix equation eq. 5.40 now becomes

$$\frac{d}{a}B_G(Q) = \sum_{G'} M_{GG'}B_{G'}(Q) \quad (5.63)$$

$$M_{GG'} = \sum_{G'}\Bigg\{\frac{1}{N}\sum_{q_1}\sum_{\alpha_1,\alpha_2} Re\left(\ln\left[\widetilde{\epsilon}_{\alpha_1}\left(q_1+\frac{Q}{2}\right)+\widetilde{\epsilon}_{\alpha_2}\left(\frac{Q}{2}-q_1\right)-\widetilde{E}\right]\right)$$

$$\sum_{G_1}\sum_{G'_1} C^{\alpha_1}_{G_1}\left(q_1+\frac{Q}{2}\right)\ C^{\alpha_1 *}_{G'_1}\left(q_1+\frac{Q}{2}\right) C^{\alpha_2}_{G-G_1}\left(\frac{Q}{2}-q_1\right)\ C^{\alpha_2 *}_{G'-G'_1}\left(\frac{Q}{2}-q_1\right)$$

$$-\frac{1}{N}\sum_{m_1=-\frac{N}{2}}^{\frac{N}{2}-1}\sum_{G_1}\ln\Bigg(\left[2(G_1-(2M+1))+\frac{2m_1}{N}\right]^2+$$

$$\left[2(G-G_1)+\widetilde{Q}-\frac{2m_1}{N}\right]^2-\widetilde{E_1}\Bigg)+\frac{\pi}{\sqrt{2}}\sqrt{\frac{\left(\widetilde{G}+\widetilde{Q}\right)^2}{2}-\widetilde{E_1}}\ \Bigg\}. \quad (5.64)$$

Notice the range in the summation $\sum_{G_1}$, $\sum_{G'_1}$ are defined so that $\max[1, G_1-2M] \leqslant G_1 \leqslant \min[G_1+2M, 4M+1]$ and $\max[1, G'_1-2M] \leqslant G'_1 \leqslant \min[G'_1+2M, 4M+1]$.

It is convenient to choose $\widetilde{E_1} = \frac{\left(\tilde{G}+\tilde{Q}\right)^2}{2}$ so that the free particle kernel part disappears. Diagonalizing the above matrix equation gives d/a as a function of $\widetilde{E}$.

With above formalism, eq. 5.64, we are able to reproduce the prior result for two atom pairing in a one dimensional periodic potential by G. Orso et al [84].

We show in Fig 5.2 the pair energies calculated for a $N = 40$ site lattice using a 9-band model. The pair energies are calculated for CM quasi-momentum $Q = 0$ using eq. 5.64. In general, for a 9-band model, there are 9 solutions for $\frac{d}{a}$ at every $\widetilde{E}$, where a is the s-wave scattering length, which is tunable using a magnetic field.

As of today, we do not fully understand the physical meaning of all of these solutions. However, I'll try to describe some qualitative or quantitative finding. Inspired by the solution inside a one dimensional harmonic well with no radial confinement, which was shown in Fig 5.1(c), we label the smallest d/a solution for a given energy as red, second to smallest solution as blue, etc. The pair energies are referenced to $E_0 = 2\widetilde{\epsilon}_1(\widetilde{Q}/2)$, corresponding to two atoms of $q_1 = -q_2 = Q/2$ both in the lowest band. States corresponding to $E_0 - E > 0$ are bound states that lie below the two particle ground state. States with $E_0 - E < 0$ correspond energies higher than two particle ground state, but lower than some excited state that is still trapped well below the lattice depth.

For $\frac{d}{a} \to -\infty$, the pair binding is weak. Thus, the solution asymptotes to two non-interacting particles inside the lattice. The dashed horizontal lines in Fig 5.2 at $(E_0 - E)/E_R = 0$ corresponds to the reference point for two atom in the ground band. The dashed horizontal line around $(E_0 - E)/E_R = -6.2$ roughly corresponds to the energy of one atom in the ground band while the other is in the first excited band.

For large $\frac{d}{a} > 0$ all solutions asymptote to tightly bound dimers, where $E_b = \frac{\hbar^2}{ma^2}$, i.e. $\frac{E_0 - E}{E_R} = \frac{E_b}{E_R} = \frac{2}{\pi^2}\left(\frac{d}{a}\right)^2$. In this case the red, blue, and yellow curves in Fig 5.2 corresponds to different CM states of a tightly bound dimer in the effective potential of the lattice, with the red be the lowest CM state, and green the largest. For

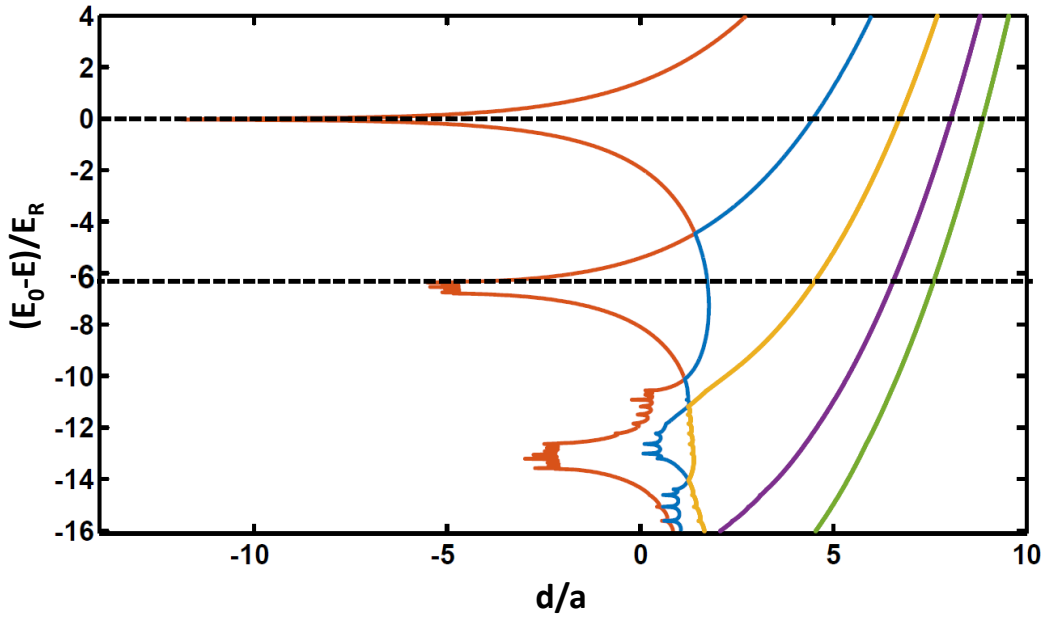

FIGURE 5.2: Dimer energy E versus scattering length a obtained by solving the 9-band model matrix equation. For a two particle of CM quasi-momentum $\widetilde{Q} = 0$ in a single color lattice of $s_1 = 20$, the dimer energies are plotted with respect to the two particle ground state E_0 and normalized to E_R.

practical purposes, usually the lowest two bands are occupied. Thus, we will only include the red and blue curves for the following discussions.

In order to compare the results of pairing energy with harmonic confinement in eq. 5.28 to the pairing energy inside a single color lattice of arbitrary depth s in eq. 5.64, we relate l_z/a in eq. 5.28 to d/a and ϵ_b to E_b/E_R. For a lattice of depth sE_R, i.e.

$$V(z) = sE_R \sin^2(\frac{\pi}{d}z) \approx sE_R \frac{\pi^2}{d^2} z^2$$

$$= \frac{1}{2} m\omega_z^2 z^2, \tag{5.65}$$

$\hbar\omega_z/E_R = \sqrt{4s} - 2$, where the 2 is an approximation for the anharmonic correction. Recall $l_z = \sqrt{\frac{\hbar}{m\omega_z}}$, therefore $\frac{d}{l_z} = \pi\sqrt{\frac{\sqrt{4s}-2}{2}}$. With $\frac{l_z}{a} \equiv I(\epsilon_b)$, for the harmonic

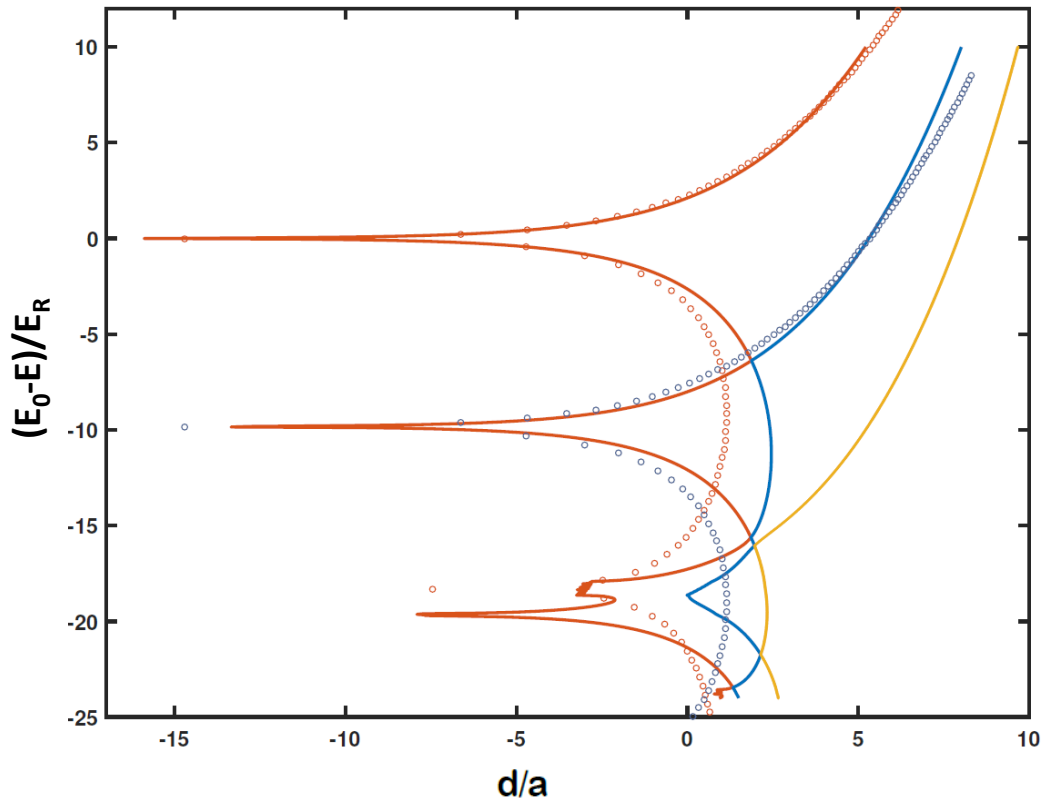

FIGURE 5.3: Comparing the 9-band model matrix equation solution for a single color lattice of $s_1 = 20$ (solid), to the one dimensional harmonic trap solution (open circle). The red, blue and yellow solid lines are the smallest three $\frac{d}{a}$ correspond to every E. The red open circles denote the harmonic confinement solution. The blue open circles denote the harmonic confinement solution shifted down by the energy difference between ground and first excited band.

oscillator solution,

$$\begin{aligned} \frac{d}{a} &= \frac{d}{l_z} I(\epsilon_b) = \pi \sqrt{\frac{\sqrt{4s}-2}{2}}\, I(\epsilon_b) \\ \frac{E_b}{E_R} &= \epsilon_b(\sqrt{4s}-2), \end{aligned} \tag{5.66}$$

We plot in Fig 5.3 the pair energies inside a single color lattice of $s_1 = 20$ obtained using eq. 5.64, where the lowest three $\frac{d}{a}$ solutions for every E are labeled by solid

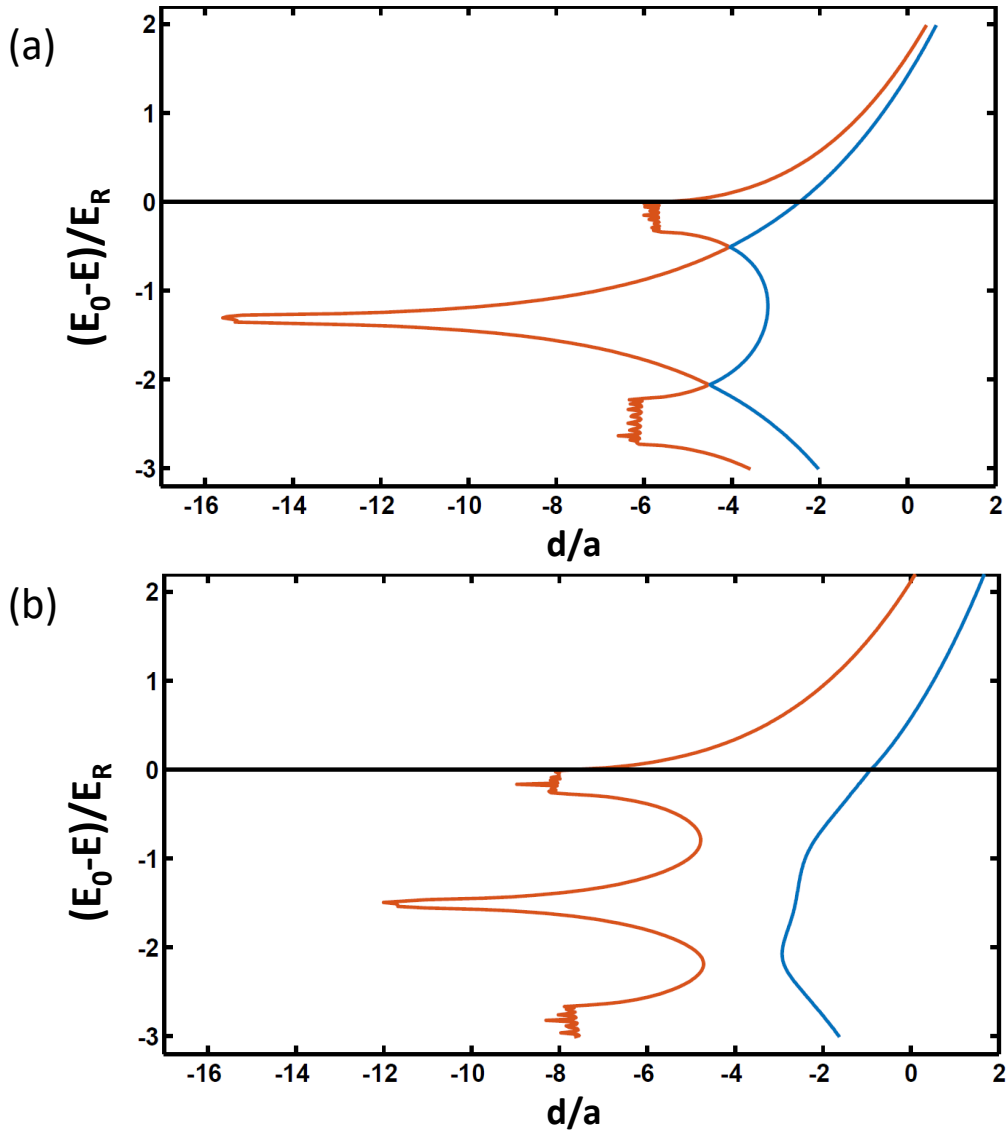

FIGURE 5.4: Pair energies in a bichromatic lattice of depth $s_1 = 10$, $s_2 = 20$, and relative phase (a) $\phi = 0$ and (b) $\phi = \frac{2\pi}{35}$. The blue solution in (b) is shifted to the right from the red solution, similar to an avoided crossing in $\frac{d}{a}$.

lines. The red open circles denote the pair energies inside a harmonic trap obtained from eq. 5.28 and eq. 5.66. The blue open circles are obtained by shifting the red open circles down by the energy difference between the ground and first excited bands. Notice that unlike the harmonic solutions, which have spikes at large negative $\frac{d}{a}$, the lattice solution has cutoff at sufficiently negative $\frac{d}{a}$, likely due to the non-zero

tunneling rate that breaks the pairs, while the pairs inside harmonic traps are always bound.

We plot in Fig 5.4 the pair energies computed using eq. 5.36 for a bichromatic lattice of depth $s_1 = 15$, $s_2 = 20$, and relative phase $\phi = 0$ or $\phi = \frac{2\pi}{35}$. Recall from Fig 2.4 and Fig 2.5 that shifting the phase by $\phi = \frac{2\pi}{35}$ causes little change in the lattice geometry and the band structure, as shown in Fig 2.4(c). It does significantly modify the ground state wavefunction, shown in Fig 2.5(c). To our surprise, it significantly alters the pair energies, as shown in Fig 5.5. For $\phi = \frac{2\pi}{35}$ the blue solution is shifted to the right from the red solution, which resembles an avoided crossing, however not in energy, but in $\frac{d}{a}$.

5.3 Preliminary RF Spectroscopy Results for Pairing in a Bichromatic Lattice

We probe the pairing energy in a bichromatic lattice using rf spectroscopy, as described in Sec 4.2. We start with the lowest two hyperfine states $|1\rangle$ and $|2\rangle$, then apply an rf pulse. We assume that we start with a paired $|1\rangle$-$|2\rangle$ state, and end up with a paired $|1\rangle$-$|3\rangle$ state. As discussed in Sec 2.2, a periodic symmetric double well potential is created when choosing lattice depths $s_1 = 10$, $s_2 = 20$ (in units of E_R), and relative phase of $\phi = 0$ in a bichromatic lattice. Here the lowest two bands are close to degenerate. Shifting the phase ϕ by $\frac{2\pi}{35}$ does not change either the lattice potential geometry or the band structure, but modifies the ground state wavefunction noticeably. The computed pair energies for a bichromatic lattice of depth $s_1 = 10$, $s_2 = 20$, and relative phase of $\phi = 0$ and $\phi = \frac{2\pi}{35}$ are shown in Fig 5.4.

We start near the magnetic Feshbach resonance, with $B = 834.6$ G. For this field, $d/a_{12} = -0.015$ is shown as the purple vertical line and $d/a_{13} = -4.285$ is shown as the green vertical line. There are at least two possible final $|1\rangle$-$|3\rangle$ states for relative phase $\phi = 0$ in Fig 5.5(a). The two lowest transition frequencies required for the rf

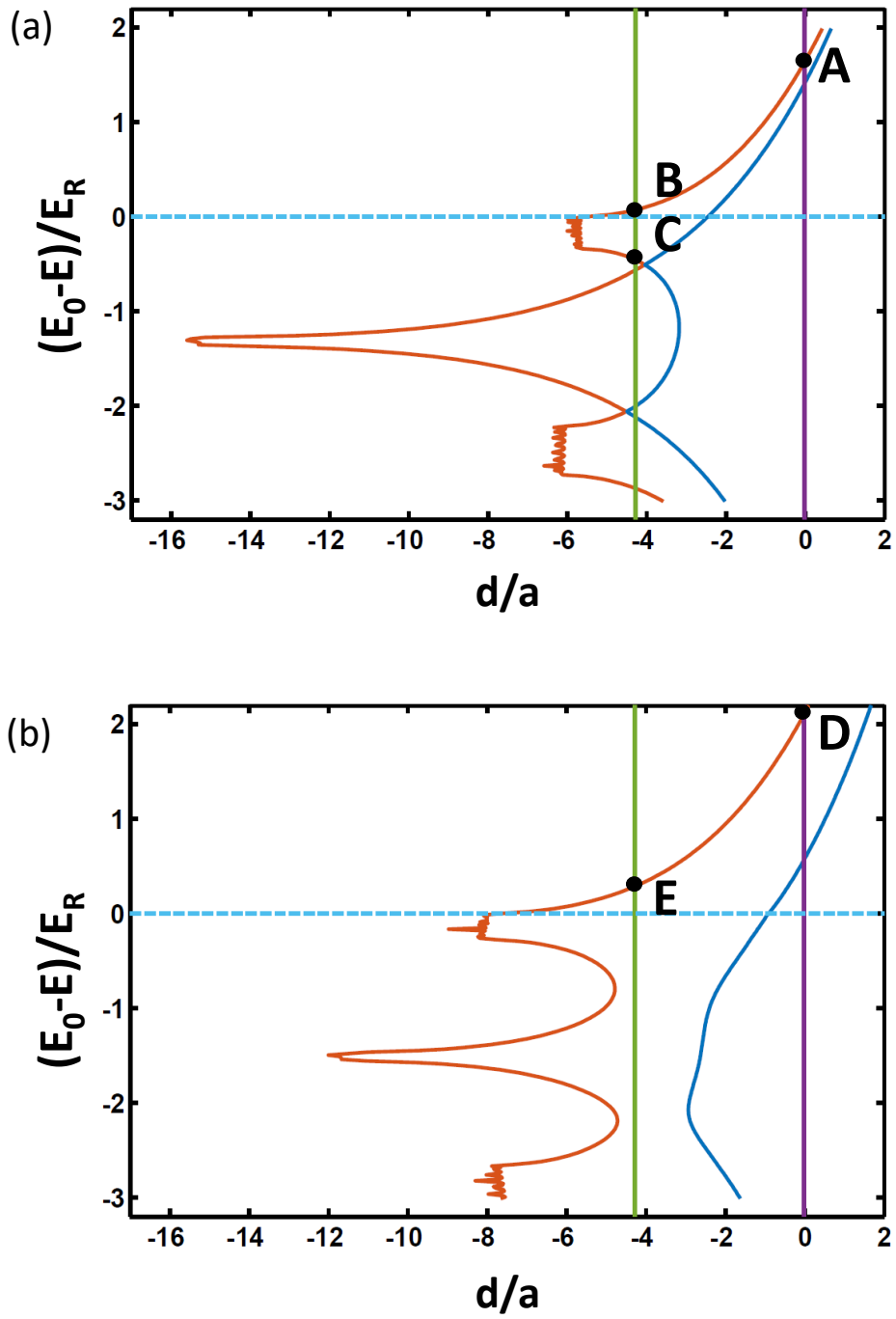

FIGURE 5.5: Pair energies in a bichromatic lattice of depth $s_1 = 10$, $s_2 = 20$, and relative phase (a) $\phi = 0$ and (b) $\phi = \frac{2\pi}{35}$. The blue solution is shifted to the right from the red solution, similar to an avoided crossing in $\frac{d}{a}$. Positions of crossing points are: A(-0.015, 1.638), B(-4.285, 0.078), C(-4.285, -0.448), D(-0.015, 2.088), E(-4.285, 0.288)

transition, as labeled on the graph in units of $E_R = 14.9$ kHz, are for $A \rightarrow B$ 23.3 kHz and $A \rightarrow C$ 31.0 kHz. After shifting the phase to $\phi = \frac{2\pi}{35}$, there is only one final $|1\rangle$-$|3\rangle$ state E that is accessible, which corresponding to a transition frequency of 26.9 kHz.

The measured spectrum for the same lattice configuration is presented in Fig 5.6 for relative phase $\phi = 0$. We find two resonances near 22 kHz and 28 kHz, close to the predicted values. For $\phi = \pm\frac{2\pi}{35}$, Fig 5.7 and Fig 5.8, we measure only one peak at 25 kHz, the same for both positive and negative phase shifts. The measured rf resonance positions agree reasonably well with the computed pair energies.

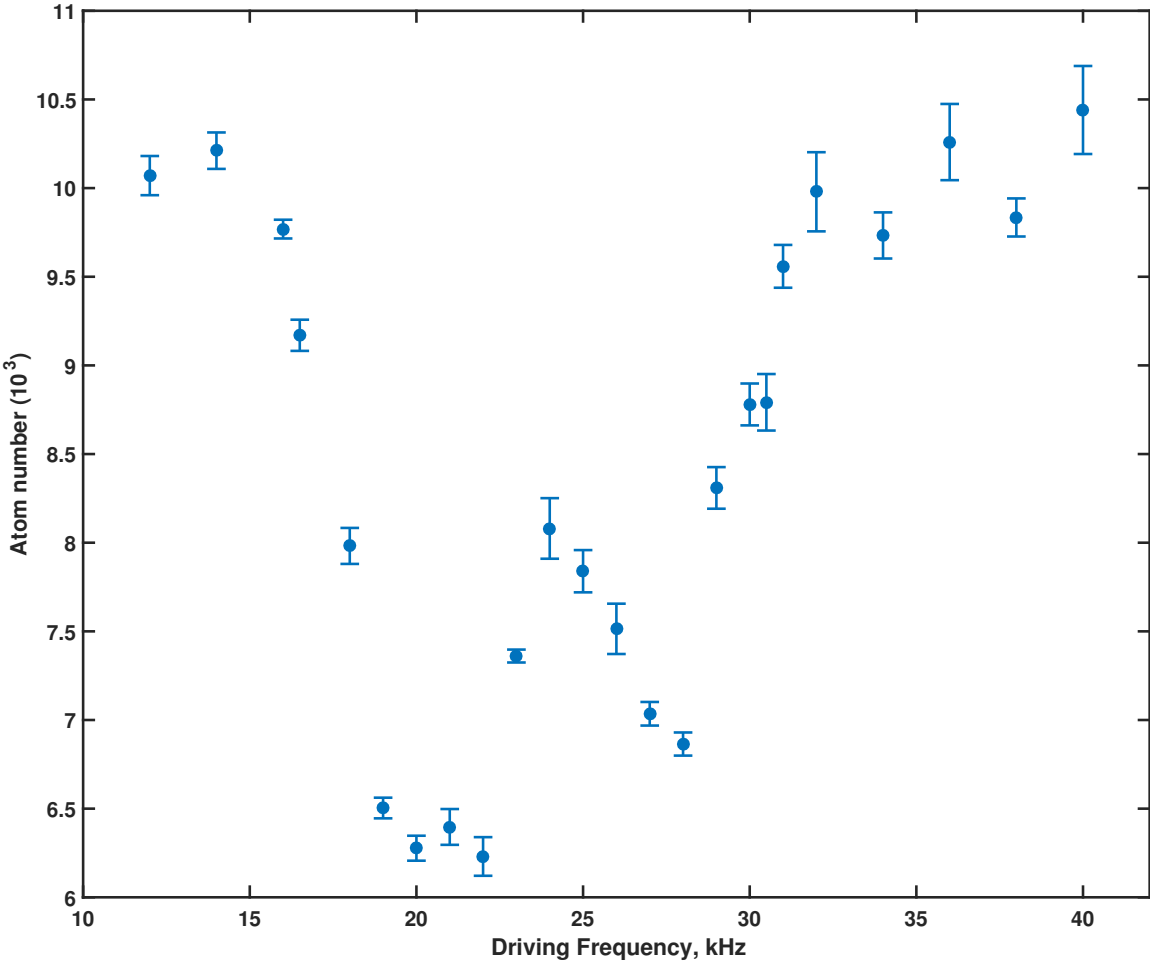

FIGURE 5.6: RF spectrum at 834 G for a bichromatic lattice of depth $s_1 = 10$, $s_2 = 20$, and relative phase $\phi = 0$.

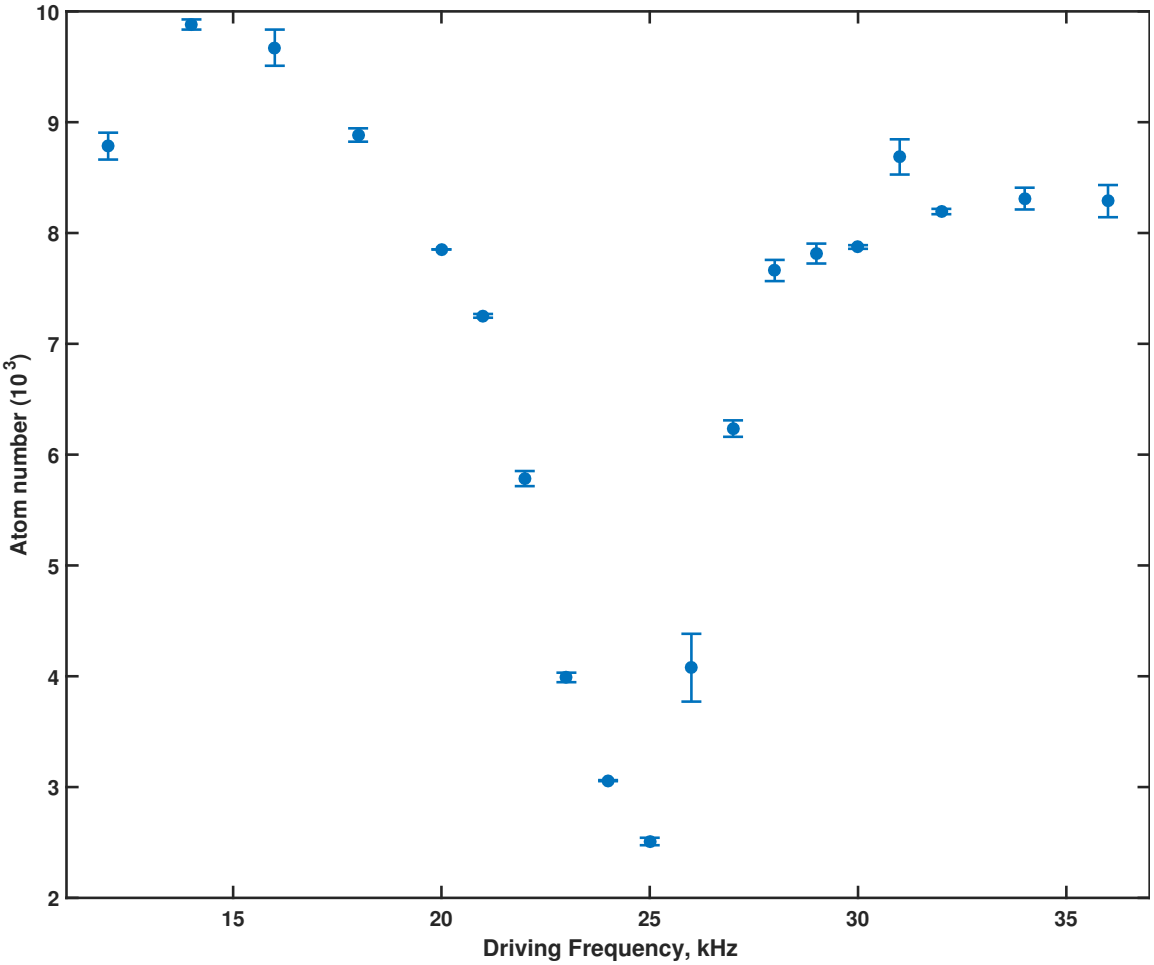

FIGURE 5.7: RF spectrum at 834 G for a bichromatic lattice of depth $s_1 = 10$, $s_2 = 20$, and relative phase $\phi = \frac{2\pi}{35}$.

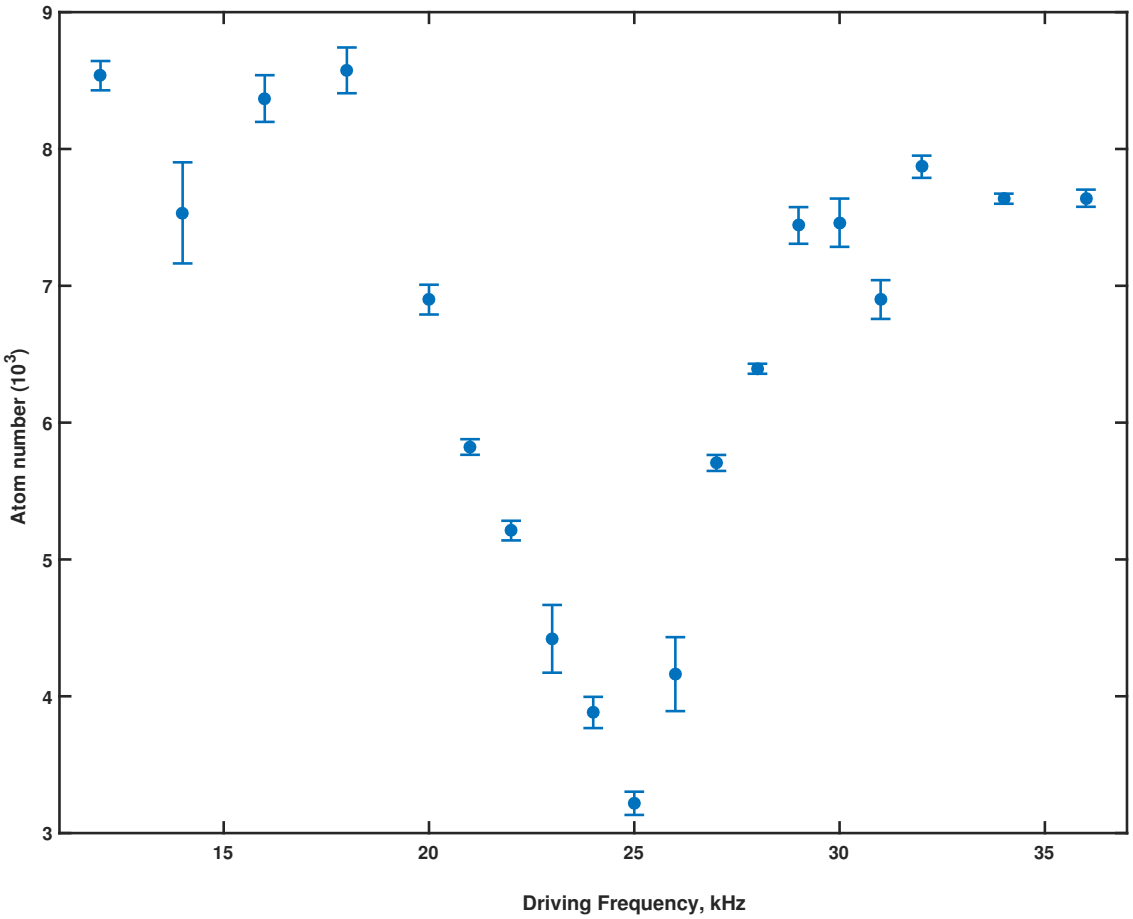

FIGURE 5.8: RF spectrum at 834 G for a bichromatic lattice of depth $s_1 = 10$, $s_2 = 20$, and relative phase $\phi = -\frac{2\pi}{35}$.

6

Conclusion

6.1 Summary of the Dissertation

This dissertation contains mainly of two pieces of work. I describe the first systematic study of pairing and thermodynamics for a Fermi gas that is continuously tuned from 2D to quasi-2D in a new trap geometry. I was able to measure both the radio frequency spectra and radial cloud profiles under identical conditions for each regime. For the quasi-2D gas, I found that the spectra were inconsistent with 2D-BCS theory. For the 2D gas, I found that the spectra can be fit by 2D-BCS mean field theory, consistent with previous work[3, 13]. In contrast to the spectra, the radii for 2D clouds were measured to be much smaller than those predicted by 2D-BCS mean field theory, which yields ideal gas density profiles[14]. These results show that there is no transition between 2D and quasi-2D systems and that beyond mean field descriptions are required in both regimes.

In the second part of the dissertation, I studied how a double well superlattice modifies the pairing of two particles interacting via s-wave collisions. I presented a Green's function scheme for computing the two particle binding energy in a one

dimensional optical lattice. The computed results for binding in a bichromatic lattice are in reasonable agreement with our preliminary rf spectroscopy measurements. However, more work is needed to fully understand the rich structure of the predicted pairing energies as a function of the s-wave scattering length.

6.2 Outlook

In the future, we plan to study fermionic atom pairing in lattices with control of dispersion. Relativistic dispersion of weakly interacting Fermi gases has been studied using a honeycomb lattice by Esslinger's group [96], which produces a cold-atom analog of graphene. In this experiment, the quasi-momentum distribution was measured to probe the Dirac point. A 1.064 μm laser was used to produce two co-propagating standing waves and one orthogonally propagating standing wave, yielding a honeycomb lattice with controllable dispersion, dependent on the relative frequencies and intensities of the superposed waves. Here, the Dirac points are topologically protected, and determined by the tunable lattice geometry. However, pairing interactions have not been studied.

Weitz's group demonstrated a cold-gas analog of relativistic Klein tunneling using a Bose-Eistein condensate of ^{87}Rb in a Fourier-synthesized optical lattice, measuring nearly 100% barrier penetration in a regime where a non-relativistic gas would have negligible penetration probability [15]. When the condensate is transferred to an energy near the Dirac point, the lattice creates a quasi-relativistic dispersion relation for the gas. In this experiment, the lattice is created by using a four-photon Raman process, which is specific to the level structure of the trapped species. While this method is elegant, it is difficult to apply to mixtures of cold atoms or atoms in more than one hyperfine state, as the detunings are state-dependent.

Our current one-dimensional bichromatic superlattice system greatly extends these experiments by enabling control of the dispersion relation in multi-component

superfluid mixtures with tunable interactions. We plan to employ radio-frequency spectroscopy to measure the evolution of the gap and spatial profile measurements to probe the thermodynamics in the transition from a quasi-2D to a 3D quasi-relativistic gas, in the strongly interacting superfluid regime. Here, our bichromatic superlattice will be used to tune the dispersion relation along the z-axis continuously from quadratic to linear by changing the stable relative phase and amplitude of the superposed optical standing wave potentials. The mechanism for controlling the dispersion is briefly described in the following section.

6.2.1 Linear Dispersion in a Bichromatic Lattice

We show in this section a derivation of how a gas with a linear dispersion relation near the zone center $q = 0$ can be generated in a bichromatic optical lattice. Recall the one dimensional bichromatic optical lattice potential, composed of an infrared lattice and a green lattice along the z direction,

$$V(z) = V_1 \cos^2(kz) + V_2 \cos^2\left(2kz + \frac{\phi}{2}\right), \tag{6.1}$$

with a depth of $V_1 \equiv -s_1 E_R < 0$ for the red-detuned 1064 nm lattice and $V_2 \equiv s_2 E_R > 0$ for blue-detuned 532 nm lattice. (We define s_1 and s_2, the lattice depth in units of $E_R = \frac{\hbar^2 k^2}{2m}$, to be positive.) For the simplest 3-band model, the Hamiltonian reduces to the following matrix equation

$$\begin{bmatrix} (\tilde{q} - \widetilde{G_0})^2 & \frac{-s_1}{4} & \frac{s_2}{4} e^{-i\phi} \\ \frac{-s_1}{4} & \tilde{q}^2 & \frac{-s_1}{4} \\ \frac{s_2}{4} e^{i\phi} & \frac{-s_1}{4} & (\tilde{q} + \widetilde{G_0})^2 \end{bmatrix} \begin{bmatrix} C^{\alpha}_{\tilde{q}-\widetilde{G_0}} \\ C^{\alpha}_{\tilde{q}} \\ C^{\alpha}_{\tilde{q}+\widetilde{G_0}} \end{bmatrix} = \widetilde{E^{\alpha}} \begin{bmatrix} C^{\alpha}_{\tilde{q}-\widetilde{G_0}} \\ C^{\alpha}_{\tilde{q}} \\ C^{\alpha}_{\tilde{q}+\widetilde{G_0}} \end{bmatrix}, \tag{6.2}$$

where $\widetilde{E} = \frac{E}{E_R}$, $G_0 = 2k$ being the reciprocal lattice vector, and $\widetilde{G_0} = 2$.

When diagonalizing the matrix, we first take the limit $s_2 \to 0$, and expand around the Brillouin zone center where $|\widetilde{q}| \ll 1$, throwing away higher order terms in $\tilde{q}^2$. The solutions $|\alpha, \widetilde{q}\rangle$ of the 3-band model for $\left(\frac{s_1}{4}\right)^2 \ll 1$ are,

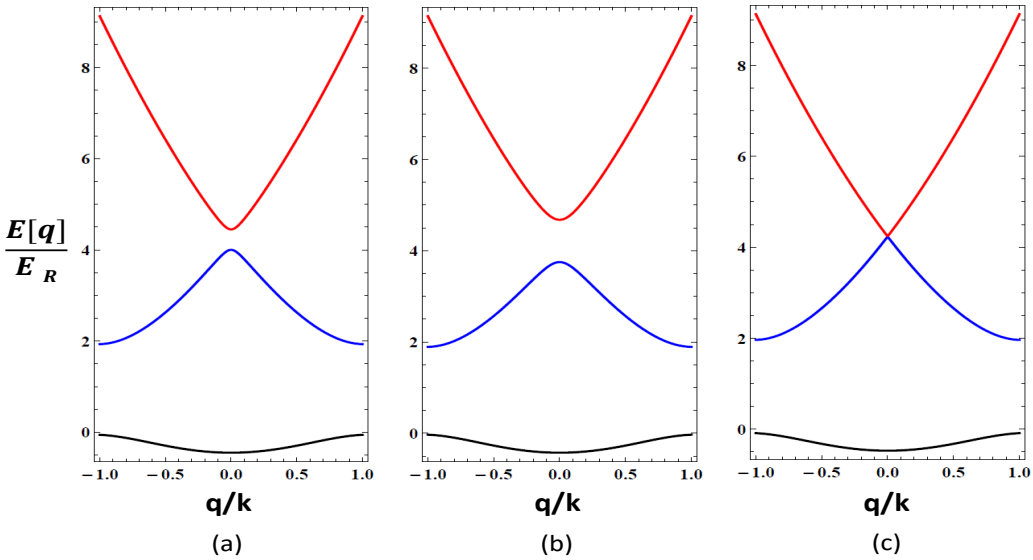

(a) (b) (c)

FIGURE 6.1: The band structure for (a) $s_1 = 4$, $s_2 = 0$, (b) $s_1 = 4$, $s_2 = 1$, $\phi = 0$, and (c) $s_1 = 4$, $s_2 = 1$, $\phi = \pi$ respectively, calculated using a 3-band model. A Dirac point is created by choosing parameters as in (b).

$$\begin{array}{ll} |3,\widetilde{q}\rangle \approx \frac{1}{\sqrt{2}}\left[\begin{array}{l} |\widetilde{q}+\widetilde{G_0}\rangle + |\widetilde{q}-\widetilde{G_0}\rangle \\ |\widetilde{q}+\widetilde{G_0}\rangle - |\widetilde{q}-\widetilde{G_0}\rangle \end{array}\right. & \tilde{E} = 4+\epsilon \\ |2,\widetilde{q}\rangle \approx \frac{1}{\sqrt{2}} \quad \left. \right] & \tilde{E} = 4 \\ |1,\widetilde{q}\rangle \approx |\widetilde{q}\rangle & \tilde{E} = -\epsilon\ , \end{array}$$

where $\epsilon = \frac{1}{2}\left(\frac{s_1}{4}\right)^2 > 0$ is always greater than zero.

As shown in Fig 6.1, the second and third excited bands are close to each other at the Brillouin zone center. So it makes sense to consider including only $|2,\widetilde{q}\rangle$ and $|3,\widetilde{q}\rangle$ if we want to study how the two bands cross. Notice also that the ground band only involves $|\widetilde{q}\rangle$, which is not coupled to $|2,\widetilde{q}\rangle$ or $|3,\widetilde{q}\rangle$ by $V_2\cos^2\left(2kz+\frac{\phi}{2}\right)$. Whereas $|2,\widetilde{q}\rangle$ and $|3,\widetilde{q}\rangle$ can couple to each other by $V_2\cos^2\left(2kz+\frac{\phi}{2}\right)$. To study the Dirac point, we need only states $|2,\widetilde{q}\rangle$ and $|3,\widetilde{q}\rangle$. We use these solutions as an approximate orthonormal basis to diagonalize the matrix in the presence of non-zero V_2.

To find the analytical expression of the energy-momentum relation at the zone center, we rewrite the matrix form of the Hamiltonian in eq 6.2 using the new basis,

where only $|2,\widetilde{q}\rangle$ and $|3,\widetilde{q}\rangle$ are coupled by the V_2 lattice. Then,

$$\begin{bmatrix} 4-\frac{s_2}{4}\cos(\phi) & 2\tilde{G}_0\tilde{q}+i\frac{s_2}{4}\sin(\phi) \\ 2\tilde{G}_0\tilde{q}-i\frac{s_2}{4}\sin(\phi) & 4+\epsilon+\frac{s_2}{4}\cos(\phi) \end{bmatrix} \begin{bmatrix} C_2 \\ C_3 \end{bmatrix} = \widetilde{E} \begin{bmatrix} C_2 \\ C_3 \end{bmatrix} \ . \tag{6.3}$$

Using this approximation, the eigenenergies in units of $E_R = \frac{\hbar^2 k^2}{2m}$, where $k = \frac{2\pi}{\lambda \sin\frac{\theta}{2}}$ are

$$\widetilde{E} = 4 + \frac{\epsilon}{2} \pm \frac{1}{2}\sqrt{\tilde{\Delta}^2 + (4\tilde{G}_0\tilde{q})^2}, \tag{6.4}$$

where $\epsilon = \frac{s_1^2}{32}$. The energy gap in between the two bands at $\widetilde{q} = 0$ is

$$\widetilde{\Delta} = |\epsilon + \frac{s_2}{2}e^{i\phi}|. \tag{6.5}$$

Ignoring the constant offset in eq. 6.4, one obtains

$$\widetilde{E} = \pm\frac{1}{2}\sqrt{\tilde{\Delta}^2 + (4\tilde{G}_0\tilde{q})^2}, \tag{6.6}$$

which can be compared with the relativistic energy-momentum relation

$$E = \pm\sqrt{(m^*c^2)^2 + (pc)^2} \ . \tag{6.7}$$

Using $pc = \hbar qc = 2\widetilde{G_0}\widetilde{q}\,E_R$, one obtains the effective speed of light

$$c_{eff} = 2\frac{\hbar k}{m} \approx 8.7\, cm/s \ . \tag{6.8}$$

The effective mass, since $m^*c^2 = E_R\frac{\tilde{\Delta}}{2}$, leads to

$$m^* = m\tilde{\Delta}/16 \tag{6.9}$$

The gap in eq. 6.5 can be closed ($\widetilde{\Delta} = 0$) by letting $\phi = \pi$ and $s_2 = 2\epsilon = \frac{s_1^2}{16}$, i.e. $V_2 = \frac{V_1^2}{16E_R}$.

The results of direct numerical diagonalization of the 3-by-3 matrix are plotted in figure 6.1. The energies of each band are represented in units of E_R and are plotted

as a function of the quasi-momentum in the first Brillouin zone for lattice depths V_1, V_2 and ϕ. By choosing proper phase $\phi = \pi$ and amplitude $s_2 = \frac{s_1^2}{16} = 1$ for $s_1 = 4$, one can tune the energy-momentum relation from quadratic to linear around the Brillouin zone center.

We plan to study pairing interactions by using the CO_2 laser confinement to increase the chemical potential, and to populate the second band. Then tuning the lattice will be used to obtain the Dirac point.

Appendix A

Polaron Model for 2D Fermi Gas Density Profile

Starting from the free energy of a spin-balanced two-dimensional Fermi gas, we can derive the zero temperature density profile inside a harmonic trap using a polaron model. The free energy consists of first two terms representing the Fermi energies of the individual species and the two terms denoting the polaron energy arising from an intermixing of both spins,

$$f = \frac{1}{2}n_1\epsilon_{F1} + \frac{1}{2}n_2\epsilon_{F2} + \frac{1}{2}n_1E_p(1) + \frac{1}{2}n_2E_p(2). \tag{A.1}$$

It is worth pointing out that the factor of $\frac{1}{2}$ arises from the energy of the ideal two-dimensional Fermi gas. We assume these Fermi polarons to be weakly interacting, so that the polaron impurity model can be extended to a 50-50 mixture.

The ideal 2D local Fermi energy of each species, ϵ_{Fi} is given by

$$\epsilon_{Fi} = \frac{2\pi\hbar^2}{m}n_i \equiv \alpha n_i. \tag{A.2}$$

Here n_i is the density of the atomic species, with $i = 1, 2$ for $|1\rangle$ and $|2\rangle$. The two-dimensional polaron energy which arises from scattering of $|2\rangle$ off the Fermi sea

of $|1\rangle$, is denoted by

$$E_p(2) = y(q_1)\epsilon_{F1}, \tag{A.3}$$

The dimensionless function $y(q_1)$ can be approximated by a simple form [86]

$$y(q_1) = \frac{-2}{\ln(1+2\,q_1)}, \tag{A.4}$$

where $q_1 \equiv \epsilon_{F1}/E_b$ denotes the ratio of the local Fermi energy, ϵ_{F1} of $|1\rangle$ to the binding energy, E_b of $|1\rangle$-$|2\rangle$ dimer in a 2D trap.

For a spin-balanced mixture $N_1 = N_2$, one has $\epsilon_{F1} = \epsilon_{F2}$ and $n_1 = n_2 = n/2$. The chemical potentials are obtained by differentiating eq. A.1 with respect to densities, $\mu_i = \partial f/\partial n_i$, resulting in

$$\mu_1 = \mu_2 = \epsilon_{F1}\left\{1 + y(q_1) + \frac{1}{2}y^{'}(q_1)\right\}. \tag{A.5}$$

where the last term $y^{'}(q_1)$ is defined to be

$$y^{'}(q_1) \equiv dy(q_1)/d\log q_1 = \frac{q_1\left[y(q_1)\right]^2}{1+2q_1}. \tag{A.6}$$

The corresponding form for the local central pressure,

$$p = n_1\mu_1 + n_2\mu_2 - f, \tag{A.7}$$

can be expressed as

$$p = \frac{n}{2}\epsilon_{F1}\left\{1 + y(q_1) + y^{'}(q_1)\right\}. \tag{A.8}$$

The Gibbs-Duhem relation determines the pressure at the trap center. For fixed temperature, $dp = nd\mu$. Since $d\mu = -dU_{trap}$, and the pressure vanishes for $U_{trap} \to \infty$, we have

$$p(0) = -\int_{\infty}^{0} n(\rho)\, dU_{trap}. \tag{A.9}$$

In a harmonic trap, $dU_{trap} = m\omega_\perp^2 \rho d\rho$ and $U_{trap} \to \infty$ as $\rho \to \infty$, we immediately obtain for $N_1 = N_2$

$$p(0) = \frac{m\omega_\perp^2}{2\pi} \int_0^\infty 2\pi\rho d\rho n(\rho) = \frac{m\omega_\perp^2 N_1}{\pi}. \tag{A.10}$$

We define $q_1 \equiv q_0 \tilde{n}_1$, where the interaction strength $q_0 \equiv \frac{E_F}{E_b}$ with $E_F \equiv \hbar\omega_\perp \sqrt{N_1}$ being the Fermi energy of an ideal gas at the harmonic trap center, and $\tilde{n}_1 \equiv n_1/n_0$, where n_0 is the ideal gas unit of density $n_0 \equiv \frac{E_F}{\alpha}$. With eq. A.8 and eq. A.10 the central density is immediately determined by numerically solving

$$\tilde{n}_1(0) = \frac{1}{\sqrt{1 + y\left[q_0 \tilde{n}_1(0)\right] + y'\left[q_0 \tilde{n}_1(0)\right]}}. \tag{A.11}$$

After finding $\tilde{n}_1(0)$ by numerically solving eq. A.11, one can determine $\tilde{\mu}_1(0)$ by rewriting the chemical potential in eq. A.5 in units of E_F, with $\tilde{\mu}_1 = \tilde{\mu}_1(0) - \tilde{\rho}^2$. The density profile is then determined for the given q_0 using

$$\tilde{\mu}_1(0) - \tilde{\rho}^2 = \tilde{n}_1(\tilde{\rho}) \left[1 + y(q_0 \tilde{n}_1) + \frac{1}{2} y'(q_0 \tilde{n}_1)\right]. \tag{A.12}$$

The density vanishes for $\rho > R$. To find R, we consider the limiting case of $\tilde{n}_1 \to 0$, Taylor expansion of the right hand side of eq. A.12 approaches $-1/(2q_0)$. The cloud radius in units of R_{TF} is then given by

$$\frac{R}{R_{TF}} = \sqrt{\tilde{\mu}(0) + \frac{1}{2q_0}}, \tag{A.13}$$

where $q_0 \equiv \frac{E_F}{E_b}$ defines the interaction strength in 2D.

The column density for the spin balanced mixture is calculated by integrating the 2D spatial profiles obtained from eq. A.12. In a harmonic trap, the predicted column density $n_{1D}(x)$ is very well fit by

$$n_{1D}(x) = n_{1D}(0)\left(1 - \frac{x^2}{R^2}\right)^{\gamma} \Theta\left[R - |x|\right], \tag{A.14}$$

where Θ is a Heaviside function, n_{1D0} is the peak column density, and n is an exponent, determined from the fit. Normalizing the x-integral of eq. A.14 to the number of atoms in one spin state yields

$$R = \frac{N_1}{n_{1D}(0)\sqrt{\pi}} \frac{\Gamma(\gamma + 3/2)}{\Gamma(\gamma + 1)}, \tag{A.15}$$

which determines R from the measured atom number and peak column density.

To find the peak column density we use eq. A.14 to fit the data within 70 percent of the apparent Thomas-Fermi radius. Thus, we avoid fitting the wings of the column density, which suffers from relatively high noise.

Bibliography

[1] Enrico Vogt, Michael Feld, Bernd Fröhlich, Daniel Pertot, Marco Koschorreck, and Michael Köhl. Scale invariance and viscosity of a two-dimensional Fermi gas. *Phys. Rev. Lett.*, 108:070404, Feb 2012.

[2] Edward Taylor and Mohit Randeria. Apparent low-energy scale invariance in two-dimensional Fermi gases. *Phys. Rev. Lett.*, 109:135301, Sep 2012.

[3] B. Fröhlich, M. Feld, E. Vogt, M. Koschorreck, W. Zwerger, and M. Köhl. Radio-frequency spectroscopy of a strongly interacting two-dimensional fermi gas. *Phys. Rev. Lett.*, 106:105301, 2011.

[4] Ariel T. Sommer, Lawrence W. Cheuk, Mark J. H. Ku, Waseem S. Bakr, and Martin W. Zwierlein. Evolution of fermion pairing from three to two dimensions. *Phys. Rev. Lett.*, 108:045302, Jan 2012.

[5] Mohit Randeria, Ji-Min Duan, and Lih-Yir Shieh. Bound states, Cooper pairing, and Bose condensation in two dimensions. *Phys. Rev. Lett.*, 62:981–984, Feb 1989.

[6] Y. Zhang, W. Ong, I. Arakelyan, and J. E. Thomas. Polaron-to-polaron transitions in the radio-frequency spectrum of a quasi-two-dimensional Fermi gas. *Phys. Rev. Lett.*, 108:235302, Jun 2012.

[7] M. G. Ries, A. N. Wenz, G. Zürn, L. Bayha, I. Boettcher, D. Kedar, P. A. Murthy, M. Neidig, T. Lompe, and S. Jochim. Observation of pair condensation in the quasi-2D BEC-BCS crossover. *Phys. Rev. Lett.*, 114:230401, Jun 2015.

[8] W. Ong, Chingyun Cheng, I. Arakelyan, and J. E. Thomas. Spin-imbalanced quasi-two-dimensional Fermi gases. *Phys. Rev. Lett.*, 114:110403, 2015.

[9] I. Boettcher, L. Bayha, D. Kedar, P. A. Murthy, M. Neidig, M. G. Ries, A. N. Wenz, G. Zürn, S. Jochim, and T. Enss. Equation of state of ultracold fermions in the 2D BEC-BCS crossover region. *Phys. Rev. Lett.*, 116:045303, Jan 2016.

[10] K. Fenech, P. Dyke, T. Peppler, M. G. Lingham, S. Hoinka, H. Hu, and C. J. Vale. Thermodynamics of an attractive 2D Fermi gas. *Phys. Rev. Lett.*, 116:045302, Jan 2016.

[11] P. A. Murthy, I. Boettcher, L. Bayha, M. Holzmann, D. Kedar, M. Neidig, M. G. Ries, A. N. Wenz, G. Zürn, and S. Jochim. Observation of the Berezinskii-Kosterlitz-Thouless phase transition in an ultracold Fermi gas. *Phys. Rev. Lett.*, 115:010401, Jun 2015.

[12] Vasiliy Makhalov, Kirill Martiyanov, and Andrey Turlapov. Ground-state pressure of quasi-2D Fermi and Bose gases. *Phys. Rev. Lett.*, 112:045301, Jan 2014.

[13] A. T. Sommer, L. W. Cheuk, M. J.-H. Ku, W. S. Bakr, and M. W. Zwierlein. Evolution of fermion pairing from three to two dimensions. *Phys. Rev. Lett.*, 108:045302, 2012.

[14] Lianyi He and Pengfei Zhuang. Phase diagram of a cold polarized fermi gas in two dimensions. *Phys. Rev. A*, 78:033613, 2008.

[15] Tobias Salger, Christopher Grossert, Sebastian Kling, and Martin Weitz. Klein tunneling of a quasirelativistic bose-einstein condensate in an optical lattice. *Phys. Rev. Lett.*, 107:240401, Dec 2011.

[16] KersonHuang. *Statistical Mechanics*. John Wiley, New York,, 2th edition, 1987.

[17] A. J. Moerdijk, B. J. Verhaar, and A. Axelsson. Resonances in ultracold collisions of ^{6}Li, ^{7}Li, and ^{23}Na. *Phys. Rev. A*, 51:4852–4861, Jun 1995.

[18] M. Bartenstein, A. Altmeyer, S. Riedl, R. Geursen, S. Jochim, C. Chin, J. Hecker Denschlag, R. Grimm, A. Simoni, E. Tiesinga, C. J. Williams, and P. S. Julienne. Precise determination of ^{6}Li cold collision parameters by radio-frequency spectroscopy on weakly bound molecules. *Phys. Rev. Lett.*, 94:103201, Mar 2005.

[19] G. Zürn, T. Lompe, A. N. Wenz, S. Jochim, P. S. Julienne, and J. M. Hutson. Precise characterization of ^{6}Li feshbach resonances using trap-sideband-resolved rf spectroscopy of weakly bound molecules. *Phys. Rev. Lett.*, 110:135301, Mar 2013.

[20] D. S. Petrov and G. V. Shlyapnikov. Interatomic collisions in a tightly confined Bose gas. *Phys. Rev. A*, 64:012706, 2001.

[21] Mohit Randeria and Edward Taylor. Crossover from Bardeen-Cooper-Schrieffer to Bose-Einstein condensation and the unitary Fermi gas. *Annu. Rev. Condens. Matt. Phys.*, 5(1):209–232, 2014.

[22] G. Bertaina and S. Giorgini. BCS-BEC crossover in a two-dimensional Fermi gas. *Phys. Rev. Lett.*, 106:110403, Mar 2011.

[23] Marianne Bauer, Meera M. Parish, and Tilman Enss. Universal equation of state and pseudogap in the two-dimensional Fermi gas. *Phys. Rev. Lett.*, 112:135302, Apr 2014.

[24] Lianyi He, Haifeng Lü, Gaoqing Cao, Hui Hu, and Xia-Ji Liu. Quantum fluctuations in the BCS-BEC crossover of two-dimensional Fermi gases. *Phys. Rev. A*, 92:023620, Aug 2015.

[25] E. R. Anderson and J. E. Drut. Pressure, compressibility, and contact of the two-dimensional attractive fermi gas. *Phys. Rev. Lett.*, 115:115301, Sep 2015.

[26] Hao Shi, Simone Chiesa, and Shiwei Zhang. Ground-state properties of strongly interacting fermi gases in two dimensions. *Phys. Rev. A*, 92:033603, Sep 2015.

[27] Alexander Galea, Hillary Dawkins, Stefano Gandolfi, and Alexandros Gezerlis. Diffusion monte carlo study of strongly interacting two-dimensional fermi gases. *Phys. Rev. A*, 93:023602, Feb 2016.

[28] Brendan C. Mulkerin, Kristian Fenech, Paul Dyke, Chris J. Vale, Xia-Ji Liu, and Hui Hu. Comparison of strong-coupling theories for a two-dimensional fermi gas. *Phys. Rev. A*, 92:063636, Dec 2015.

[29] Andrea M. Fischer and Meera M. Parish. Quasi-two-dimensional Fermi gases at finite temperatures. *Phys. Rev. B*, 90:214503, Dec 2014.

[30] Andrea M. Fischer and Meera M. Parish. BCS-BEC crossover in a quasi-two-dimensional Fermi gas. *Phys. Rev. A*, 88:023612, Aug 2013.

[31] Yu.E. Lozovik and V.I. Yudson. Superconductivity at dielectric pairing of spatially separated quasiparticles. *Solid State Communications*, 19(4):391 – 393, 1976.

[32] J. Kasprzak, M. Richard, S. Kundermann, A. Baas, P. Jeambrun, J. M. J. Keeling, F. M. Marchetti, M. H. Szyman, acuteska, R. Andr, J. L. Staehli, V. Savona, P. B. Littlewood, B. Deveaud, and Le Si Dang. Boseeinstein condensation of exciton polaritons. *Nature*, 443(7110):409–414, 2006.

[33] A. A. High, J. R. Leonard, A. T. Hammack, M. M. Fogler, L. V. Butov, A. V. Kavokin, K. L. Campman, and A. C. Gossard. Spontaneous coherence in a cold exciton gas. *Nature*, 483(7391):584–588, 2012.

[34] A. C. Gossard L. V. Butov and 4 D. S. Chemla1. Macroscopically ordered state in an exciton system. *Nature*, 418(6899):751–754, 2012.

[35] J. A. Seamons, C. P. Morath, J. L. Reno, and M. P. Lilly. Coulomb drag in the exciton regime in electron-hole bilayers. *Phys. Rev. Lett.*, 102:026804, Jan 2009.

[36] J. P. Eisenstein and A. H. MacDonald. Boseeinstein condensation of excitons in bilayer electron systems. *Nature*, 432:691–694, 2004.

[37] E. Tutuc, M. Shayegan, and D. A. Huse. Counterflow measurements in strongly correlated gaas hole bilayers: Evidence for electron-hole pairing. *Phys. Rev. Lett.*, 93:036802, Jul 2004.

[38] M. Kellogg, J. P. Eisenstein, L. N. Pfeiffer, and K. W. West. Vanishing hall resistance at high magnetic field in a double-layer two-dimensional electron system. *Phys. Rev. Lett.*, 93:036801, Jul 2004.

[39] Y. W. Suen, L. W. Engel, M. B. Santos, M. Shayegan, and D. C. Tsui. Observation of a ν=1/2 fractional quantum hall state in a double-layer electron system. *Phys. Rev. Lett.*, 68:1379–1382, Mar 1992.

[40] J. P. Eisenstein, G. S. Boebinger, L. N. Pfeiffer, K. W. West, and Song He. New fractional quantum hall state in double-layer two-dimensional electron systems. *Phys. Rev. Lett.*, 68:1383–1386, Mar 1992.

[41] D. R. Luhman, W. Pan, D. C. Tsui, L. N. Pfeiffer, K. W. Baldwin, and K. W. West. Observation of a fractional quantum hall state at $\nu = 1/4$ in a wide gaas quantum well. *Phys. Rev. Lett.*, 101:266804, Dec 2008.

[42] Maxim Yu Kharitonov and Konstantin B Efetov. Excitonic condensation in a double-layer graphene system. *Semiconductor Science and Technology*, 25(3):034004, 2010.

[43] A. S. Mayorov, D. C. Elias, M. Mucha-Kruczynski, R. V. Gorbachev, T. Tudorovskiy, A. Zhukov, S. V. Morozov, M. I. Katsnelson, A. K. Geim, and K. S. Novoselov. Interaction-driven spectrum reconstruction in bilayer graphene. *Science*, 333(6044):860–863, 2011.

[44] R. T. Weitz, M. T. Allen, B. E. Feldman, J. Martin, and A. Yacoby. Broken-symmetry states in doubly gated suspended bilayer graphene. *Science*, 330(6005):812–816, 2010.

[45] Markus Greiner, Olaf Mandel, Tilman Esslinger, Theodor W. Hansch, and Immanuel Bloch. Quantum phase transition from a superfluid to a mott insulator in a gas of ultracold atoms. *Nature*, 415(6867):39–44, Jan 2002.

[46] Belen Paredes, Artur Widera, Valentin Murg, Olaf Mandel, Simon Folling, Ignacio Cirac, Gora V. Shlyapnikov, Theodor W. Hansch, and Immanuel Bloch. Tonks-girardeau gas of ultracold atoms in an optical lattice. *Nature*, 429(6989):277–281, May 2004.

[47] Toshiya Kinoshita, Trevor Wenger, and David S. Weiss. Observation of a one-dimensional tonks-girardeau gas. *Science*, 305(5687):1125–1128, 2004.

[48] Andrew G. Truscott, Kevin E. Strecker, William I. McAlexander, Guthrie B. Partridge, and Randall G. Hulet. Observation of fermi pressure in a gas of trapped atoms. *Science*, 291(5513):2570–2572, 2001.

[49] C. Chin, M. Bartenstein, A. Altmeyer, S. Riedl, S. Jochim, J. Hecker Denschlag, and R. Grimm. Observation of the pairing gap in a strongly interacting fermi gas. *Science*, 305(5687):1128–1130, 2004.

[50] M. W. Zwierlein, J. R. Abo-Shaeer, A. Schirotzek, C. H. Schunck, and W. Ketterle. Vortices and superfluidity in a strongly interacting fermi gas. *Nature*, 435(7045):1047–1051, Jun 2005.

[51] Robert Jordens, Niels Strohmaier, Kenneth Gunter, Henning Moritz, and Tilman Esslinger. A mott insulator of fermionic atoms in an optical lattice. *Nature*, 455(7210):204–207, Sep 2008.

[52] Jae-yoon Choi, Sebastian Hild, Johannes Zeiher, Peter Schauß, Antonio Rubio-Abadal, Tarik Yefsah, Vedika Khemani, David A. Huse, Immanuel Bloch, and Christian Gross. Exploring the many-body localization transition in two dimensions. *Science*, 352(6293):1547–1552, 2016.

[53] Richard P. Feynman. Quantum mechanical computers. *Optics News*, 11(2):11–20, Feb 1985.

[54] Tim Rom, Thorsten Best, Olaf Mandel, Artur Widera, Markus Greiner, Theodor W. Hänsch, and Immanuel Bloch. State selective production of molecules in optical lattices. *Phys. Rev. Lett.*, 93:073002, Aug 2004.

[55] Immanuel Bloch. Ultracold quantum gases in optical lattices. *Nat Phys*, 1(1):23–30, Oct 2005.

[56] Immanuel Bloch, Jean Dalibard, and Sylvain Nascimbene. Quantum simulations with ultracold quantum gases. *Nat Phys*, 8(4):267–276, Apr 2012.

[57] N. W. Ashcroft and N. D. Mermin. *Solid State Physics*. W. B. Saunders, Philadelphia, 1976.

[58] Charles Kittel. *Introduction to Solid State Physics*. Wiley.

[59] Markus Greiner, Immanuel Bloch, Olaf Mandel, Theodor W. Hänsch, and Tilman Esslinger. Exploring phase coherence in a 2d lattice of bose-einstein condensates. *Phys. Rev. Lett.*, 87:160405, Oct 2001.

[60] D. McKay, M. White, and B. DeMarco. Lattice thermodynamics for ultracold atoms. *Phys. Rev. A*, 79:063605, Jun 2009.

[61] P. A. Murthy, D. Kedar, T. Lompe, M. Neidig, M. G. Ries, A. N. Wenz, G. Zürn, and S. Jochim. Matter-wave fourier optics with a strongly interacting two-dimensional fermi gas. *Phys. Rev. A*, 90:043611, Oct 2014.

[62] Kenneth Martin O'Hara. *Optical Trapping end Evaporatice COoling of Fermionic Atoms*. PhD thesis, Duke University, 2000.

[63] Daniel L. Freimund, Kayvan Aflatooni, and Herman Batelaan. Observation of the kapitza-dirac effect. *Nature*, 413(6852):142–143, Sep 2001.

[64] Subhadeep Gupta, Aaron E. Leanhardt, Alexander D. Cronin, and David E. Pritchard. Coherent manipulation of atoms with standing light waves. *Comptes Rendus de l'Acadmie des Sciences - Series IV - Physics*, 2(3):479 – 495, 2001.

[65] C. C. Tsuei and J. R. Kirtley. Pairing symmetry in cuprate superconductors. *Rev. Mod. Phys.*, 72:969–1016, Oct 2000.

[66] John Singleton and Charles Mielke. Quasi-two-dimensional organic superconductors: A review. *Contemporary Physics*, 43(2):63–96, 2002.

[67] D. L. Smith and C. Mailhiot. Theory of semiconductor superlattice electronic structure. *Rev. Mod. Phys.*, 62:173–234, Jan 1990.

[68] Michael R. Norman. The challenge of unconventional superconductivity. *Science*, 332(6026):196–200, 2011.

[69] M. Baranov, D. Efremov, and M. Kagan. The enhancement of the superconductive transition temperature in quasi-2D materials in a parallel magnetic field. *Physica (Amsterdam)*, 218C:75, 1993.

[70] J.-P. Martikainen and P. Törmä. Quasi-two-dimensional superfluid fermionic gases. *Phys. Rev. Lett.*, 95:170407, Oct 2005.

[71] S. S. Botelho and C. A. R. Sá de Melo. Vortex-antivortex lattice in ultracold fermionic gases. *Phys. Rev. Lett.*, 96:040404, Feb 2006.

[72] Lianyi He and Pengfei Zhuang. Phase diagram of a cold polarized Fermi gas in two dimensions. *Phys. Rev. A*, 78:033613, Sep 2008.

[73] Wei Zhang, G.-D. Lin, and L.-M. Duan. Berezinskii-Kosterlitz-Thouless transition in a trapped quasi-two-dimensional Fermi gas near a Feshbach resonance. *Phys. Rev. A*, 78:043617, Oct 2008.

[74] J. Tempere, S. N. Klimin, and J. T. Devreese. Effect of population imbalance on the Berezinskii-Kosterlitz-Thouless phase transition in a superfluid Fermi gas. *Phys. Rev. A*, 79:053637, May 2009.

[75] H. Caldas, A. L. Mota, R. L. S. Farias, and L. A. Souza. Superfluidity in two-dimensional imbalanced Fermi gases. *J. Stat. Mech.*, 2012(10):P10019, 2012.

[76] Shaoyu Yin, J.-P. Martikainen, and P. Törmä. Fulde-Ferrell states and Berezinskii-Kosterlitz-Thouless phase transition in two-dimensional imbalanced Fermi gases. *Phys. Rev. B*, 89:014507, Jan 2014.

[77] Daniel E. Sheehy. Fulde-Ferrell-Larkin-Ovchinnikov state of two-dimensional imbalanced Fermi gases. *Phys. Rev. A*, 92:053631, Nov 2015.

[78] Kirill Martiyanov, Vasiliy Makhalov, and Andrey Turlapov. Observation of a two-dimensional Fermi gas of atoms. *Phys. Rev. Lett.*, 105:030404, Jul 2010.

[79] Michael Feld, Bernd Frohlich, Enrico Vogt, Marco Koschorreck, and Michael Kohl. Observation of a pairing pseudogap in a two-dimensional Fermi gas. *Nature*, 480(7375):75–78, December 2011.

[80] Marco Koschorreck, Daniel Pertot, Enrico Vogt, Bernd Frohlich, Michael Feld, and Michael Kohl. Attractive and repulsive Fermi polarons in two dimensions. *Nature*, 485(7400):619–622, May 2012.

[81] Alexey A Orel, Paul Dyke, Marion Delehaye, Chris J Vale, and Hui Hu. Density distribution of a trapped two-dimensional strongly interacting Fermi gas. *New J. Phys.*, 13(11):113032, 2011.

[82] Yingyi Zhang. *Radio Frequency Spectroscopy Of a Quasi-Two-Dimensional Fermi Gas*. PhD thesis, Duke University, 2013.

[83] Christian Langmack, Marcus Barth, Wilhelm Zwerger, and Eric Braaten. Clock shift in a strongly interacting two-dimensional fermi gas. *Phys. Rev. Lett.*, 108:060402, 2012.

[84] G. Orso, L. P. Pitaevskii, S. Stringari, and M. Wouters. Formation of molecules near a Feshbach resonance in a 1d optical lattice. *Phys. Rev. Lett.*, 95:060402, 2005.

[85] Meera Parish, private communication.

[86] Michael Klawunn and Alessio Recati. Fermi polaron in two dimensions: Importance of the two-body bound state. *Phys. Rev. A*, 84:033607, Sep 2011.

[87] M. Klawunn. Equation of state and Kosterlitz-Thouless transition temperature in two-dimensional Fermi gases: An analytical approach. arXiv:1510.02081v2 [cond-mat.quant-gas], 2016.

[88] Shahin Bour, Dean Lee, H.-W. Hammer, and Ulf-G. Meißner. *Ab initio* lattice results for Fermi polarons in two dimensions. *Phys. Rev. Lett.*, 115:185301, Oct 2015.

[89] W. Ketterle, D.S. Durfee, and D.M. Stamper-Kurn. Making, probing and understanding bose-einstein condensates. in bose-einstein condensation in atomic gases, proceedings of the international school of physics "enrico fermi". pages 67–176, 1999.

[90] Michael Eric Gehm. *PREPARATION OF AN OPTICALLY-TRAPPED DEGENERATE FERMI GAS OF ^{6}LI: FINDING THE ROUTE TO DEGENERACY*. PhD thesis, Duke University, 2003.

[91] Here, $\tilde{\mu}(0) = \tilde{n}(0)\{1+y_m[q_0\tilde{n}(0)]+y'_m[q_0\tilde{n}(0)]/2\}$, where $y'_m(q) \equiv q\,y_m^2(q)/(1+2q)$ and $q_0 = E_F/E_b$. We determine the scaled total density $\tilde{n}(0)$ self-consistently from $\tilde{n}(0) = 1/\sqrt{1 + y_m[q_0\tilde{n}(0)] + y'_m[q_0\tilde{n}(0)]}$. For a detailed explanation, see the supplementary material of Ref. [8].

[92] Paul Bloom. Two-dimensional fermi gas. *Phys. Rev. B*, 12:125–129, Jul 1975.

[93] Zbigniew Idziaszek and Tommaso Calarco. Analytical solutions for the dynamics of two trapped interacting ultracold atoms. *Phys. Rev. A*, 74:022712, Aug 2006.

[94] D. S. Petrov and G. V. Shlyapnikov. Interatomic collisions in a tightly confined bose gas. *Phys. Rev. A*, 64:012706, Jun 2001.

[95] M. Kanász-Nagy, E. A. Demler, and G. Zaránd. Confinement-induced interlayer molecules: A route to strong interatomic interactions. *Phys. Rev. A*, 91:032704, Mar 2015.

[96] Leticia Tarruell, Daniel Greif, Thomas Uehlinger, Gregor Jotzu, and Tilman Esslinger. Creating, moving and merging dirac points with a fermi gas in a tunable honeycomb lattice. *Nature*, 483(7389):302–305, Mar 2012.

Biography

Chingyun Cheng was born April 1, 1983 in Taiwan. She received her B.S. and M.S. degrees in Physics department from National Tsing-Hua University in Hsin-chu, Taiwan. Her master's research in the field of theoretical condensed matter physics was on Dilute Magnetic Semiconductors. She joined Dr. John Thomas's group at Duke University in 2009 and conducted experiments on pairing of ultracold quantum gases in optical bichromatic lattices.